UKAEA-CCFE-PR(22)40

S.M. Kaye, J.W. Connor, C.M. Roach

# Confinement and Transport in Spherical Tokamaks: A Review

# Confinement and Transport in Spherical Tokamaks: A Review

S.M. Kaye, J.W. Connor, C.M. Roach

# Confinement and Transport in Spherical Tokamaks: A Review

S.M. Kaye[1], J.W. Connor[2], C.M. Roach[2]

e-mail contact: kaye@pppl.gov

## Abstract

In this paper, we review the confinement and transport properties observed and predicted in low aspect ratio tokamaks, or spherical tokamaks (STs), which can depart significantly from those observed at higher aspect ratio. In particular, thermal energy confinement scalings show a strong, near linear dependence of energy confinement time on toroidal magnetic field, while the dependence on plasma current is more modest, the opposite of what is seen at higher aspect ratio. Furthermore, STs show a strong increase of normalized confienemnt with decreasing collisionality, a dependence that is much stronger than that at higher aspect ratio. These differences reflect the fundamental differences in transport in STs due to the more extreme toroidicity than plasmas at higher aspect ratio, and to the relatively larger $E \times B$ shearing rates, both of which can suppress electrostatic drift wave instabilities at both ion and electron gyroradius scales. In addition, the importance of much stronger electromagnetic effects due to the ST operating at high $\beta_T$ are clearly observed and inferred. These latter effects bring into light importance both Microtearing modes and Kinetic Ballooning modes have a much stronger impact in the core of STs plasmas than at higher aspect ratio. These differences have led to inferring a very strong improvement in normalized confinement with decreasing collisionality, $\Omega\tau_E \propto \nu_{e,*}{}^{-1}$, much stronger than at higher aspect ratio, which bodes well for an ST-based fusion pilot plant should this trend continue. Gyrokinetic studies, coupled with low- and high-$k$ turbulence measuements, have shed light on the underlying physics controlling transport. At lower $\beta$, both ion- and electron-scale electrostatic drift turbulence may be responsible for transport, while at higher $\beta$, MTMs, KBMs, and hybrid TEM-KBMs play a role. Flow shear will, of course affect the balance between ion- and electron-scale modes. Non-linear gyrokinetic simulations find regimes where the electron heat flux decreases with decreasing collisionality, consistent with the experimental global normalized confinement scaling. The ST is unique in that the relatively low toroidal

---

[1] Princeton Plasma Physics Laboratory, Princeton University, Princeton, NJ 08543, USA

[2] CCFE, Abingdon, Oxfordshire OX 14 3DB UK

magnetic field allows for localized measurements of electon-scale turbulence, and this coupled with turbulence measurements at ion-scales has facilitated detailed comparisons with gyrokinetic simulations. These data have provided compelling evidence for the presence of ITG and ETG turbulence in some plasmas, and direct experimental support for the impact of experimental actuators like $\gamma_E$, $R/L_n$ and magnetic shear on turbulence and transport.

---

# I. Introduction

A spherical torus or tokamak (ST) is a tokamak with an aspect ratio ($A = R/a$) less than approximately two.[1,2] The ST provides a potential transformative route to a more compact and possibly lower cost Component Test Facility[3]/Fusion Nuclear Science Facility[4–6] (CTF/FPP) or Fusion Pilot Plant[7–11] (FPP) because of its compactness and because of its fundamental properties of enhanced confinement and stability at low aspect ratio, which have been established quantitatively in the first generation of high-powered STs: NSTX[12,13] and MAST.[14] The ST configuration also has physics advantages, as can be seen from results of early studies as well as from 0D considerations. For instance, work has predicted that STs can operate in regimes of high $\beta_T$, as was demonstrated in START[15] and NSTX,[16] an economic metric that maximizes the plasma energy with respect to the energy in the toroidal field that has to be provided by external power. The ST is an inherently high plasma current machine due to its low aspect geometry and strong natural shaping (e.g., elongation) $\kappa$,[17] with

$$I_p \sim \frac{(1+\kappa^2)}{2}\frac{R_0 B_0}{q_a}\frac{Af(A)}{A^2-1},\ where f(A) = 1.22A - 0.68 \tag{1}$$

The high current leads to a higher MHD stability limit, given crudely by $\beta_T = \beta_N I_p/(aB_0)$, as well as to a higher self-driven bootstrap current[18,19] deemed necessary for advanced tokamak Pilot Plants. The bootstrap fraction is given by $f_{bs} \sim (1+\kappa^2)\frac{\beta_N}{/} l_i$ for fixed aspect ratio and $I/aB$. Thus, the ability to optimize $\beta_N$ and $\kappa$ is critical. The ST configuration affords a large accessible range in these parameters and thus flexibility in this optimization, as well as the ability to achieve stable operation at high $\kappa$ (up to 2.9) and high-$\beta_N/l_i$ (in excess of 14) was shown in NSTX.[20,21]

These characteristics help maximize the $nT\tau_E$ metric, given by

$$nT\tau_E \sim \frac{H^2}{q^3} R_0^2 B_T^3 (\frac{\kappa}{A^3})^3 \tag{2}$$

where, $H$ is confinement enhancement factor defined as $\tau_e/\tau_{E,98y,2}$, where $\tau_{E,98y,2}$ is the parametric scaling of energy confinement time based on a multi-machine database,[22] $\kappa$ is plasma elongation, and $A$ is aspect ratio $R_0/a$. In addition, operation at low aspect ratio and high elongation can help maximize the ratio of fusion power to the resistive dissipation in the TF center leg, which can be expressed as

$$\frac{P_{fusion}}{P_{TF}} \sim \beta_N^2 (1+\kappa^2)^2 \left(\frac{R_o B_o}{q_a}\right)^2 \frac{f(A)^2}{(A-1)^4 A^2} \tag{3}$$

Recent studies[10,11] have, in fact, demonstrated the possibility of designing small, compact steady-state ST fusion pilot plants. These studies use system codes that recognize standard operating limits (e.g., the Greenwald density limit, the Sykes-Troyon $\beta$ limit[23,24] with and without additional wall stabilization), current drive efficiencies and basic engineering constraints, and the utilization of high temperature superconducting magnets. They calculate the fusion power output, or the fusion gain factor, $Q$ (ratio of fusion power to input power) as a function of size, TF winding pack density, and other variables. Critical to all these pilot plant studies, as can be seen by the above relations, at both small and higher aspect ratio, is the scaling of energy confinement time, $\tau_E$, particularly with respect to dimensionless parameters such as collisionality $\nu_*$ and $\beta$. The conventional scaling, $\tau_{E,98y,2}$ effectively scales almost inversely with $\beta$, and it has no dependence on $\nu_*$. STs are at the extreme limits of the multi-machine database as regards aspect ratio, and beyond the limits as regards $\beta$. There is evidence, which will be discussed in this paper, that ST energy confinement has a weak dependence on $\beta$ but a strong inverse dependence on $\nu_*$, both of which would be favorable for a small, compact spherical tokamak power plant. It would strengthen the case for this path to fusion power if the empirical scalings could be augmented by first principles calculations of turbulent transport, as has been initiated in early studies[25,26] particularly as this would allow confident extrapolation to parameter values typical of an ST power plant.

The ST configuration also presents physics challenges in several areas. STs with neutral beam auxiliary heating can operate in a regime where the ratio of fast particle velocity to Alfvén velocity exceeds one, and this could lead to destabilization of multiple Alfvén Eigenmodes (AEs), which can couple to one another and impact severely the heating and current drive efficiency of the fast ions.[27] Furthermore, the compact nature of the ST can lead to high divertor and wall power and particle fluxes, and the enhanced flux expansion properties of divertor configurations such as the X and Super-X,[28,29] and snowflake[30] have been tested as a means to ameliorate divertor heat loads.

It is important to note that additional (i.e., non-confinement and transport related) ST-relevant physics has been carried out in other spherical tokamaks around the world. The Helicity Injection Tokamak[31] (HIT) in the U.S. employed co-axial helicity injection (CHI) to initiate the plasma non-inductively. HIT-II[32] has also studied non-inductive startup along with Pegasus, as well as QUEST,[33] TS3/4,[34] UTST[35] and HIST[36] (the latter four in Japan), VEST[37] (Korea) and SUNIST[38] (China). TST-2[39] and LATE[40] (both in Japan) will investigate high harmonic fast wave (HHFW) and ECH heating respectively. CDX-U/LTX[41,42] (U.S.), is investigating liquid lithium as a plasma facing component. An excellent review of the international ST program progress and ST research results can be found in the review article by Ono and Kaita[43] .

The purpose of this paper is to review the confinement and transport physics, crucial to the development of an ST pilot plant, that has been studied in STs over the past three decades or more. While there are a multitude of STs internationally, the review will focus on results from START[44] (UK), NSTX[12,13] (US), MAST[14] (UK), Pegasus[45] (US) and Globus-M[46] and M2[47] (Russia). A comparison of the basic operating parameters of these STs is given in Table 1. Also included in this table are the operating parameters of ST experiments that follow on to those whose results are discussed: ST40 (Tokamak Energy Ltd, UK), MAST-Upgrade (CCFE, UK) and NSTX-Upgrade (PPPL, US). These will be discussed more in the concluding section of this review.

In Section II, we will review L-H threshold experiments, in Section III, we will review dimensional and dimensionless global scaling studies, in Sections IV, V and VI we will review momentum confinement, particle confinement and Internal Transport Barrier results respectively, and in Section VII, we will summarize what gyrokinetic analysis of experiments has revealed about the plasma turbulence underlying anomalous transport in STs. We will then Conclude in Section VIII.

## II. L-H Threshold Studies

H-mode operation in STs was found to be similar to that at conventional aspect ratio, often leading to improved confinement, and with the main L- to H-mode transition signatures of a sudden drop in the $D_\alpha$ signal, an accelerated rise in plasma density, development of edge pedestals in the temperature and/or density profiles, and often decreases of edge turbulence and increase in edge rotation after the transition. H-mode operation in STs was initially identified in START, specifically in Double Null Divertor discharges.[48] Improvements in particle confinement were inferred from the rise of plasma density and the development of density pedestals,[49] and L-H transitions were often observed in Ohmic discharges. L-H threshold powers exceeded published scaling-derived values[50] by up to a factor of 30. It was suggested that the high edge neutral density in START, and the associated high convective heat loss, could impede the L-H transition.

H-modes were obtained successfully during the first years of operation on NSTX[51–53] and MAST[54–56] (Figure 1, taken from Field et al.[56]). More recently, H-modes were also obtained on Pegasus,[57,58] and during the first operational period of NSTX-U.[59] In both MAST and NSTX, transitions into ELMy H-modes were clear and reproducible, even in Ohmic plasmas, and the transitions were facilitated and were most reproducible using center stack gas fueling.[60,61] Inboard fueling led to increased toroidal flow velocities in the outboard midplane in MAST and in the core in Pegasus, possibly leading to a suppression effect on turbulence. Inferred from this increased toroidal flow velocity was a reduction in radial electric field.[62] In NSTX, the measured edge carbon rotation was largest just prior to the transition, and then reversed direction after.[60]

The threshold power was further found to be minimized through careful configuration control; well-balanced double null plasmas led to the lower threshold powers than for unbalanced or single-null configurations.[63,64] Since there were no significant changes in recycling or core impurity levels with these configuration changes, it was posited that the threshold power was influenced strongly by the parallel connection length, which also changed strongly with configuration.[63] On Pegasus, H-modes were obtained either in a limiter or a single null divertor plasma.[58] The threshold power in limiter configurations on Pegasus was up to three times greater than that in divertor plasmas, consistent with the $q$-dependence as predicted by the FM$^3$ model.[65] The NSTX plasmas, however, did not show agreement with the FM$^3$ model.

Later work on MAST and NSTX tested the impact of other operational aspects to see their effect on the L-H threshold power. On MAST, a shorter outer divertor leg led to lower threshold powers,[62] and while application of $n$=4, 6 edge magnetic fields had little effect on the threshold power, they were effective in mitigating the first ELM in the H-mode phase[66] . In NSTX, applied $n$=3 magnetic perturbations, used for dynamic error field correction, led to almost a doubling of the normalized L-H power threshold ($P_{LH}/n_e$)[64,67] (note that either $P_{thr}$ or $P_{LH}$ will be used to denote the L-H threshold power). This threshold power was determined by adjusting the neutral beam voltage in small increments to find the minimum power for transition into the H-mode. In the study, the discharges that transitioned into the H-mode at the lower applied magnetic fields also exhibited higher toroidal velocity shear towards the edge of the plasma.

The same NSTX L-H study presented in the above reference[67] also assessed several other factors that could influence the L-H transition. The particle fueling-less High Harmonic Fast Wave heating capability on NSTX allowed for studies of the dependence of $P_{thr}$ on plasma species, an important concern for ITER, and it showed that the threshold power normalized to plasma density was 20 to 40% greater in helium than in deuterium. Furthermore, there was evidence of a strong hysteresis, with the H-L threshold approximately 30 to 40% lower than the L-H threshold, indicating that once in the H-mode, the NSTX discharges could remain in this state with $P_{heat} < P_{thr}$.

A unique observation on NSTX was the dependence of the threshold power on plasma current,[68,67] which has not been seen at higher aspect ratio. On NSTX, the dependence was strong (see Figure 2, taken from Kaye et al.[67]), with threshold powers nearly doubling going from 0.7 to 1.0 $MA$. As will be shown below, this result is qualitatively consistent with the result that the $P_{thr}$ at low aspect ratio depends on the total magnetic field at the edge,[69] not just the toroidal field; at low aspect ratio, $B_T \sim B_p$, while at higher aspect ratio, $B_T \gg B_p$ at the edge. XGC0[70] calculations showed that the neoclassical radial electric field well, caused by the thermal ion loss cone near the plasma edge, was distinctly deeper and exhibited stronger $E_r$ shear at low than high current, consistent with the lower threshold. The deeper well reflected the loss of lower energy particles, and those with higher $v_\parallel/v$ than for the higher current.

The NSTX results also showed lower thresholds for higher lithium evaporation rates used for wall conditioning, as well as for lower triangularity plasmas where the X-point was at larger major radius (see Figure 10 in Kaye et al.[67]). XGC0 was used again here, to explore possible neoclassical effects that could lead to lower thresholds at both larger X-point radius and with more lithium conditioning. It was found that maintaining the $E_r \times B$ shear rate resulting from the thermal ion loss cone near the edge requires less heat flux, and thus leads to lower thresholds, as X-point radius increases with a lower divertor recycling to fueling ratio (low recycling with lithium conditioning).[71] The easier access to H-mode in a low-recycling condition was reported also on Pegasus, which made use of titanium gettering.[58]

Early statistical studies in both NSTX[53] and MAST[72] attempted to relate the transition characteristics to leading theories of the L-H transitions of the time. The theories were based on the drift-resistive ballooning mode,[73,74] peeling modes,[75] the drift-Alfvén instability[76] and finite-$\beta$ drift waves.[77] In the studies for both devices, the data were categorized by whether they were in the L-mode, H-mode or either dithering or in an L-phase just prior to an L-H transition ("L-H"). In NSTX, the results indicated a clear separation of the L- and H-mode data with respect to the critical parameters of the first three theories (Figure 3, taken from Kaye et al.[53]) However, there was essentially no difference observed in the cluster of discharges that remained in the L-mode versus the L-mode points that transitioned into the H-mode. This result was found also in MAST.[72] This indicates that while these theories reflected differences between L- and H-mode plasmas, they could not predict and L-H transition.

The finite-$\beta$ drift wave theory predicts a critical pedestal electron temperature for transition into the H-mode, where the critical temperature is related to the point where sheared flows can suppress the turbulence. This theory showed some success in modeling C-Mod and DIII-D,[77] but was not successful in modeling the NSTX data; for NSTX, the $T_e/T_{e,crit}$ ranges were the same for the L-mode and the "L-H" points. On the other hand, this theory showed some success in modeling MAST. Figure 4, taken from Counsell et al.,[72] shows the cluster of L-H points having slightly higher pedestal $T_e$ values relative to the critical value, $T_{e,crit} = T_{EC}$ than do the L-mode points.

Not taken into account in any of these theories is the electric field caused by nonambipolar loss of fast, neutral beam ions. In NSTX, it was found that bounce precession fishbones, which cause large loss or redistribution of the fast ions reflected by large drops in the neutron rate, led directly to an L-H transition.[53] An incremental 3 $kV/m$ radial electric field could result from the estimated loss of fast ions, and because of the factor of five to ten lower operating $B_T$ at low relative to high aspect ratio, could lead to high rotational shear values.

Edge turbulence suppression was observed on MAST,[63] NSTX[78] and Pegasus[58] once the plasma transitioned into the H-mode. In NSTX, no change in turbulence characteristics or shear flow was observed during the period immediately preceding the transition,[79,78] however.

L-H threshold powers in STs typically exceed those predicted by various scalings developed from conventional aspect ratio ($R/a \sim 2.5$ *to* 4) tokamaks by factors of several up to greater than an order of magnitude. In fact, the ranges of threshold powers for the three STs discussed, normalized to the conventional aspect ratio threshold power scaling predicted by Martin et al.,[80] exhibited a strong dependence on aspect ratio. As the aspect ratio decreases towards one (MAST to NSTX to Pegasus), this ratio increases significantly, as shown in Figure 5, taken from Thome et al.[57]

This trend had been recognized implicitly in the re-analysis of the ITPA threshold database, augmented by NSTX and MAST threshold data.[69] It was found in this analysis that an aspect ratio dependence given by

$$F(A)^\gamma = \left[\frac{A}{1-\left[\frac{2}{1+A}\right]^{1/2}}\right]^\gamma \tag{4}$$

where, $A = R/a$ and $\gamma = 0.5 \pm 0.5$, helped to order the data with the low $A$ data included better than did the conventional aspect ratio scalings. The aspect ratio correction factor is related to the trapped particle fraction, the magnitude of which is itself related to parallel flow or current, which was hypothesized to impact the transition mechanism. With a higher trapped particle fraction (lower $A$), the parallel flow/current would be reduced. The work also considered two additional factors: total, instead of just toroidal magnetic field and $Z_{\text{eff}}$ ($\propto Z_{\text{eff}}^{0.7}$). The use of the total magnetic field attempted to address the current dependence found in the NSTX threshold data, although its parameterization in the scaling, $|B_{TOT}|^{0.7}$, led to a weaker dependence than that observed on NSTX. The full fromula is

$$P_{thr} = 0.072 B_{tot}^{0.7} n_{20}^{0.7} S^{0.9} (Z_{\text{eff}}/2)^{0.7} F(A)^\gamma \tag{5}$$

where $S$ is plasma surface area. The fits of $P_{thr}/P_{scal}$ using a conventional $A$ scaling and the modified scaling is shown in Figure 6, taken from Takizuka et al..[69]

## III. Global Confinement Scalings

Systematic and statistical studies have been conducted in STs, as they have in conventional aspect ratio tokamaks, to develop an understanding of the parametric dependences of both thermal and global energy confinement times on both engineering and physics parameters. Engineering parameters are those that can be controlled externally, e.g., $I_p$, $B_T$, $R$, $a$, $P_{heat}$, $n$, $\kappa$, $\delta$, while dimensionless physics variables such as $\rho_*$, $\beta$, $\nu_*$, are intrinsic to the plasma. The physics parameters, and other dimensionless variables such as $R/a$, $q$, $\kappa$, $\delta$, are intercorrelated, and thus present challenges to determining the parametric variations directly, using them as regression variables, or by transformation from engineering variable scalings. For the latter, due to the intercorrelation of the dimensionless variables, small changes in engineering variable dependences can lead to large changes in the various physics parameter dependences. The best path forward to determine dependencies on physics parameters is through dedicated and controlled experiments, although these have not yet been performed in STs to the extent that they have at conventional aspect ratio.

Confinement studies have been performed primarily in MAST (CCFE, UK), NSTX (PPPL, U.S.), Globus-M (Ioffe Inst., Russia) and most recently Globus-M2, which is an upgrade of Globus-M. The comparison in operating parameters among these STs is given in Table 1 (Section I). NSTX and MAST are similar in size and operating parameters, while Globus-M, M2 are smaller. Confinement studies, most notable at higher $B_T$, $I_p$ and heating power will be conducted over the next several years in MAST-Upgrade, NSTX-Upgrade and ST40, the latter being a high-field ST built and operated by the private company Tokamak Energy Ltd (UK). Operating parameters for these STs are included in Table 1 as well.

### A. Dimensional Variable Scalings

For simplicity, the scalings are assumed to have the form:

$$\tau_E \propto B_T^{\alpha B} I_p^{\alpha I} R^{\alpha R} n_e^{\alpha n} P_{heat}^{\alpha P} \kappa^{\alpha\kappa} ..... \qquad (6)$$

where the coefficients have been determined historically through Multiple Linear Regression[82] (MLR) or closely related approaches that take into account variable uncertainties.[83,84] Recently, more advanced machine learning methods have been adopted.[85–87] In this section, we will first discuss results of the parametric trends of confinement time based on engineering variables, followed by a similar discussion revolving around the physics variables. As will be seen, some differences that emerge from engineering scalings even within one device can be reconciled when viewed from the perspective of physics variables.

H-mode operation comprised the majority of confinement-related experiments in STs such as START, MAST, NSTX, Globus-M and Pegasus,and only limited work has been done on assessing OH or L-mode confinement. First physics operation of NSTX found that ohmic confinement followed the neoAlcator trend, with a nearly linear increase of confinement with line-averaged density, and a saturation of the confinement for Greenwald fractions ($\frac{n_e}{n_G}$ where $n_G = \frac{I_p}{\pi a^2}$ and $a$ is the plasma minor radius) $> 0.8$.[88] Additional ohmic scaling results were reported by the Globus-M ST group at the Ioffe Institute in St. Petersburg, Russia, where the energy confinement time $\tau_E$ was found to scale as $\tau_e \propto n_e$ for $n_e < 2.5 \times 10^{19}\ m^{-3}$, but it was found to be weaker than linear at higher $n_e$, saturating at Greenwald fractions also of $\frac{n_e}{n_G} \sim 0.8$.[89] In addition, a linear dependence on $I_p$ but a weak dependence on $P_{heat}$ and $H \sim 0.5$ to 0.7 was found in ohmic H-modes. Confinement times in START ohmic plasmas appeared to be bounded by the neoAlcator scaling predictions.[90]

An L-mode study, performed during early neutral beam heating operation in NSTX,[91] assessed the parametric dependence of global energy confinement time, which included the fast ion component, as determined from magnetic equilibrium reconstructions, and found that

$$\tau_E \ = 4.74 \times 10^{-4} B_T^{0.7} I_p^{1.01} n_e^{0.07} P_{loss}^{-0.37} \tag{7}$$

in $sec$, $T$, $MA$, $10^{19}\ m^{-3}$ (line-averaged density), $MW$ (total power lost across the separatrix). While the strong scaling in current is consistent with that seen at conventional aspect ratio, note that there is also a strong dependence on toroidal field, and a weaker degradation with loss power.

Early H-mode experiments on high-heating power STs indicated higher than L-mode energy confinement times. While not explicitly identified as H-modes, discharges on the high-$\beta$ START ST produced discharges with flat density profiles and large edge density gradients representative of H-modes, and deduced confinement times that were close to H-mode scaling predictions.[92] In a more dedicated study in START, ELMy discharges were found to exhibit similar trends to, and exceed the 97ELMy scaling.[49,50]

High neutral beam power operation in both MAST and NSTX resulted in routine access to the H-mode regime, and studies on both devices showed the H-mode confinement scaling to be quite different than that at conventional aspect ratio in terms of the dependence on $I_p$ and $B_T$. Early studies with boronized wall conditioned discharges in NSTX[93] involved both dedicated single variable scans as well as statistical studies. In these studies, an almost linear dependence of thermal confinement time on plasma current $I_p^{0.98}$ was observed at fixed $B_T$ (0.45 $T$) and heating power (4.4 $MW$), although the plasma current increase from 0.65 $MA$ to 1.2 $MA$ was correlated with a 30% increase in density. In addition to this trend with plasma current, a significant $B_T$ dependence from 0.25 to 0.45 $T$ was also observed. Statistical analyses of the data using various methods confirmed a strong, nearly linear scaling with $B_T$. The correlation between the density and current was accounted for in in the statistical analysis, where the $I_p$ dependence was found to be clearly less than linear, with a strong, accompanying density dependence. Using ordinary MLR, the scaling was found to be

$$\tau_E \ = 4.69 \times 10^{-9} B_T^{1.08} I_p^{0.57} n_e^{0.44} P_{loss}^{-0.73} \tag{8}$$

Accounting for the errors-in-variables, the PCEIV method modified the coefficients somewhat, most notably in a weaker power degradation ($P_{loss}^{-0.50}$), but the other dependences remained similar.

Early experiments on MAST found H-enhancement factors strongly dependent on ELM frequency, with $H$ decreasing from 1.5 to 0.5 as the ELM frequency increased.[63] MAST data also provided the means to determine an aspect ratio dependence relative to the IPB98y,2 scaling, with $\tau_E \propto (R/a)^{-0.81}$ with bean-shaped (PBX, PBX-M) and circular cross-section data were omitted.[94] Dedicated, single parameter scans were performed on MAST to determine the $I_p$ and $B_T$ dependence of thermal confinement, and dependences similar to those on NSTX (Eq. 8) were found. Figure 7, taken from Valovic et al.,[95] shows the total and electron stored energies as a function of $I_p$ and $B_T$ for MAST H-mode plasmas. The solid and dashed lines in the plots show the fit and the maximum and minimum slopes consent with uncertainties in the data. The data, which consist of both ELM-free and ELMing discharges, clearly follow the NSTX trend, with a weaker than linear scaling with plasma current and a strong (even stronger than NSTX) dependence on toroidal magnetic field. Given an estimate for fast ion content, the thermal energy confinement time at fixed density ($1.1 \times 10^{20}$ $m^{-3}$) in MAST was found to scale as

$$\tau_E \ = 0.186 B_T^{1.4} I_p^{0.59} P_{loss}^{-0.73} \tag{9}$$

remarkably similar to that in NSTX.

Later experiments in NSTX with boronized walls, but this time with only a small variation in density over the course of the scan, confirmed the weak $I_p$ and strong $B_T$ dependence. Figure 8, taken from Kaye et al.,[93] shows these trends.

The first neutral beam heating experiments in Globus-M showed a strong $\tau_E$ dependence on both $I_p$ and $B_T$ with $\tau_E \propto I_p^{0.8\pm0.1}B_T^{0.8\pm0.1}$.[96] A subsequent study[97] refined the Globus-M scaling, and found that:

$$\tau_E \ = 6.08^{-3} B_T^{1.28\pm0.12} I_p^{0.48\pm0.21} n_e^{0.77\pm0.04} P_{loss}^{-0.54\pm0.26} \tag{10}$$

consistent with scalings determined from MAST and NSTX data. It was found,[98] however, that while $\tau_E \propto n_e B_T$, there was some sign of possible saturation of confinement above some, possibly $B_T$-dependent critical density (Figure 9, taken from Bakharev et al.[98]). Recent experiments on Globus-M2 with toroidal fields up to 0.8 $T$ also show a $B_T$-dependent density saturation up to 0.7 $T$ as well as indicating that the strong $B_T$ scaling holds at these higher fields.[99] Figure 10, taken from Kurskiev et al,[99] shows that the thermal confinement time from the combined Globus-M and Globus-M2 dataset, spanning the ranges of 0.25 $T < B_T \ < 0.8\ T$ and 0.11 $MA < I_p \ < 0.4\ MA$ is well represented by the scaling

$$\tau_{GBLB20} \propto B_T^{1.19} I_p^{0.43} n_e^{0.58} P_{loss}^{-0.59} \tag{11}$$

A study in NSTX that seemed to contradict the strong $B_T$ scaling and weaker $I_p$ scaling was one that was conducted with lithium conditioning of the plasma walls. To do this, a downward facing lithium evaporator was utilized, with pre-shot lithium evaporation in the ranges of a few to up to 1000 $mg$. The global and thermal electron energy confinement times were found to increase linearly with amount of lithium deposition[100] For modest amounts of lithium evaporation ($\sim$ 100 to 200 $mg$), dedicated, single parameter scans actually showed confinement scalings more similar to the ITER98y,2 scaling, with a nearly linear dependence on plasma current and a weak dependence on toroidal magnetic field (Figure 11), taken from Kaye et al.[101] These seemingly contradictory results were reconciled by considering the variation of normalized confinement with collisionality, as will be discussed in the next section on Dimensionless Variable Scalings.

Because NSTX and MAST operated at similar aspect ratio and plasma size, no size dependence in the ST confinement scalings could be deduced from these early studies. Furthermore, the Globus-M thermal confinement results in neutral beam heated plasmas were reported only recently. The approach to determining the size dependence in the ST scalings was performed by Buxton et al.[102] under the assumption that the transport was controlled by plasma physics in a quasi-neutral plasma with no Debye length dependence. This assumption constrains fit coefficients for engineering parameters, including major radius, to guarantee that the fit to be dimensionally correct (i.e., $\tau_E$ in $sec.$). In this work, the fit, including the size scaling, was based on the dataset used in Kaye et al.[91] It was recognized, however, that another assumption was required to mitigate the effect of correlations among the engineering variables in this dataset, and it was assumed that the transport was gyroBohm, consistent with NSTX.[93] With this assumption, the following scaling was determined:

$$\tau_E \ = 0.21 B_T^{0.91} I_p^{0.54} n_e^{-0.05} P_{loss}^{-0.38} R^{2.14} \tag{12}$$

Figure 12a, taken from Buxton et al.[102] shows a collection of START, MAST and NSTX data as a function of the IPB98y,2 scaling, while Figure 12b shows the same dataset as a function of the scaling relation given above. The dataset is better described by Equation 12 than by the IPB98y,2 scaling, with this scaling relation giving higher precision and accuracy.

Kurskiev et al.[103] combined data from START, MAST, NSTX, Globus-M and Globus-M2 (up to 0.8 T) to derive the following size-dependent ST scaling, which is shown in Figure 13.

$$\tau_{E,scal} = 0.066 I_p^{0.53} B_T^{1.05} P_{abs}^{-0.58} n_e^{0.65} R^{2.66} \kappa^{0.78} \tag{13}$$

The standard IPB98y,2 scaling, derived from devices with aspect ratio $R/a > 2.5$, has an aspect ratio dependence of $(R/a)^{-0.58}$, and it overpredicts the confinement time on STs, as can be seen in Fig. 2, from Kaye et al[104] in the work analyzing the international multi-machine global confinement database. The ST data used for this comparison were taken from MAST and boronized-wall NSTX H-mode plasmas from the respective early experimental campaigns. The ST data was incorporated into the database not only for comparison, but also for assessing their effect on this aspect ratio scaling. A series of statistical studies were performed in Kaye et al,[104] finding that, with some minor modifications to the exponents of the other engineering variables, a stronger aspect ratio dependence was found, with confinement scaling as $(R/a)^{-0.73}$ (see Eq. 3 of Kaye et al[104]), indicating an improvement in confinement time as aspect ratio decreases, holding all other engineering variables fixed.

Local transport analyses were carried out in NSTX, MAST and Globus-M to understand the underpinning of the strong increase of confinement with toroidal field. In NSTX,[93] it was found that the electron temperature profile broadened at fixed $q$, plasma current, heating power and density with increasing $B_T$ (Figure 14a), and this was accompanied by a reduction in the anomalous electron diffusivity for $r/a > 0.4$ (Figure 14b). The ion temperature also increased with increasing $B_T$ (Figure 15a), but the ions remained in the neoclassical range in the outer half of the discharge (Figure 15b). Both figures are taken from Kaye et al.[93] The electron transport was also seen to decrease in the outer half of the discharge with increasing current, but not as strongly as with increasing toroidal field, reflecting the weaker dependence of confinement on $I_p$. The electron thermal diffusivity exhibited a strong decrease with increasing amounts of lithium deposition.[100] The variation of thermal diffusivities in the inner core of the plasma in NSTX may be controlled by energetic particle-driven modes,[105] but no reduced model to characterize this has yet been developed.

Local transport studies in Globus-M were performed using the ASTRA code.[96] Because only a limited number of measured radial ion temperature points were available, the simulations assumed a neoclassical ion thermal diffusivity. It was found for the range of $B_T$ and $I_p$ studied (0.4 to 0.5 $T$ and 0.2 to 0.25 $MA$ respectively), the measured points fit well to profiles predicted in this fashion. Both $T_i$ and $T_e$ were found to increase with toroidal field at fixed $I_p$ . and with increasing current at fixed $B_T$. The thermal diffusivities deduced from these analyses are shown in Figure 16, taken from Telnova et al..[96] The $\chi_e$ in the inner half radius decreases with increasing $B_T$ (unlike NSTX, where the decrease was in the outer half radius), while it decreases in the outer half radius with increasing $I_p$.

## B. Dimensionless Variable Scalings

A more physics-based method of parametrerizing energy confinement, one that connects more directly to neoclassical and turbulence theories of transport, is to cast the scaling in terms of dimensionless parameters. These include the normalized gyroradius $\rho_*$, beta $\beta$, normalized collisionality $\nu_*$, and safety factor $q$, in addition to geometric parameters such as $\kappa$, $\delta$, $R/a$, etc. The dimensionless variables relate to the engineering and plasma parameters in the following fashion: $\rho_* = \frac{\rho}{a} \propto \frac{T^{1/2}}{aB}$, $\beta \propto \frac{nT}{B^2}$, $\nu_* \propto \frac{anq}{\epsilon^{5/2}T^2}$. $q \propto \frac{B\epsilon a}{I}$, where $\epsilon = \frac{a}{R}$. $T$ is plasma temperature, and $n$ is plasma density. In addition, parameters describing the plasma, such as ionic atomic mass $M$, the electron-ion temperature ratio $T_e/T_i$, and impurity content $Z_{\text{eff}}$, may be included.

In dimensionless form, the energy confinement can be written as

$$\Omega_c \tau_E \ \propto \rho_*^{\alpha\rho} \beta^{\alpha\beta} \nu_*^{\alpha\nu} q^{\alpha q} ....... \tag{14}$$

where $\Omega_c \propto B$, is the ion cyclotron frequency, which is introduced to make the left-hand side of the equation dimensionless. The form above is expected to provide the physics of confinement that does not involve phenomena that breaks the quasi-neutrality condition. Correspondingly, the four powers of $B$, $R$, $P$ and $n$ in the form given in Section 2.1 can be cast in terms of just three independent combinations, known as the "Kadomtsev constraint".[106–108]

There are three primary approaches to determining the dimensionless scalings, each having pros and cons. The first is to use techniques such as MLR or PCEIV directly, as was done for the engineering variables. As can be seen from the definitions of the dimensionless variables, there are common engineering and plasma variables among them, potentially causing strong intercorrelations. Care must be taken, then, to identify and handle these correlations to avoid misleading results. The second approach is to use simple linear transformations from the engineering coefficients to the dimensionless variable coefficients based on definitions of the latter. This has been used previously for IPB98y,2, and for the ST scalings contained in Kaye et al.,[91] and is described nicely in Buxton et al.[102] Again, however, the correlations among the variables lead to extreme sensitivity in the transformed exponents; small changes in the engineering variable exponents can lead to large changes in the exponents of the dimensionless variable expressions. The third approach is experimentally based, single parameter scans, for which careful discharge tailoring is necessary to hold certain profiles fixed in order to fix the non-scanned dimensionless variables locally. Such experiments have been performed on conventional aspect ratio tokamaks[109,110 *and references therein*], and an attempt at this was made on MAST.[111] Other studies on STs focused on attempting to fix several dimensionless variables globally, while scanning another. This approach led to inevitable variations in the "fixed" parameters, as will be seen later in this section.

As was seen in the previous section, there were stark differences between STs and conventional aspect ratio tokamaks in their parametric dependences of $\tau_E$ on $I_p$ and $B_T$. These differences are reflected in the dimensionless variable scalings as well, most notably on the dependence of normalized confinement on collisionality. It was recognized early on in MAST that plasmas at lower collisionality had higher confinement enhancements ($\tau_E/\tau_{E,98y2}$) than those at higher collisionality.[101] These results indicated a favorable collisionality dependence, with $H_{98y,2} \propto \nu_*^{-0.23}$ (as compared to $B\tau_{E,98y,2} \propto \nu_*^0$ at the higher aspect ratio), and, although a correlation between $\rho_*$ and $\nu_*$ existed, the effect on the collisionality exponent was deemed to be small.

Dimensionless parameter scans were performed in NSTX to investigate the dependence of confinement on $\nu_{e,*}$ (normalized electron collisionality) and $\beta_T$ (toroidal $\beta$) at constant $q$.[112] A factor of three variation in collisionality in the first scan was achieved in these boron-conditioned wall plasmas by varying the toroidal field and plasma current at constant $B_T/I_p$, while also varying plasma density at fixed heating power. These scans found a much stronger collisionality dependence than at higher aspect ratio, with $B\tau_E \propto \nu_{e,*}^{-0.97}$, although there was a ~20% variation in both $\rho_*$ and $\beta_T$ across this collisionality range. The $\beta_T$ scan was accomplished by varying density and input power at constant $B_T$ and $q$. The resulting near factor of three variation in $\beta_T$ was accompanied by a 20% variation in $\rho_*$ and $\nu_{e,*}$ across this range. The effect of these 20% variations in each of the scans was determined statistically to give a scaling range of $B\tau_E \propto \nu_{e,*}^{-0.7\pm0.2}\beta_T^{0.3\pm0.1}$, with an inverse relation between the $\nu_{e,*}$ and $\beta_T$ exponents. For this sensitivity analysis, the $\rho_*$ variation was assumed to be in the gyroBohm range, with $\rho_{e,*}^{(-2.5\ to\ -3.5)}$.

Using a transformation from engineering to dimensionless variables, the authors in Valovic et al.[95] found that for MAST H-mode plasmas,

$$B\tau_E \propto \rho_*^{-4.4}\beta^{1.0}\nu_*^{-0.74}q^{-2.1} \tag{15}$$

The strong dependence on $\rho_*$ and $\beta$ was due to these variables having a strong correlation. The collisionality scaling was found to be strong, and consistent with that found on NSTX. The authors noted that this strong collisionality scaling was a consequence of the fact that $\alpha_I + \alpha_B \sim 2$ is much greater than 1.08 from the IPB98y,2 scaling. Assuming gyroBohm transport, the relation between the $I_p$ and $B_T$ exponents and those of the dimensionless variables is given by

$$\alpha_I + \alpha_B = (2 - 2\alpha_{\beta)})/(5/2 - \alpha_\beta - 2\alpha_\nu) \tag{16}$$

with the $\alpha_\nu$ term being the dominant one that controls the $\alpha_I + \alpha_B$ sum. The authors found further that there was, additionally, a dependence on $q$. They noted these dependences by comparing the effective thermal diffusivity $\chi_{\text{eff}}$ at two different currents with the assumption that the transport was gyroBohm ($\propto \rho_*^3$). The effective diffusivity treats the ions and electrons as a single fluid, and it is defined as $\chi_{\text{eff}} \propto q_T/n\nabla T$, where it is assumed $T_e = T_i$, and $q_T$ is the total heat flux across a surface. The $\chi_{\text{eff}}$ ratios were found to be a factor of two lower than that expected if the transport was gyroBohm, but they could be reconciled if $\chi_{\text{eff}}$ also incuded dependences on $q$, $\beta$ and/or $\nu_*$ (see Figure 17, taken from Valovic et al.[95]).

More controlled scans of the dependence of normalized confinement on dimensionless parameters were performed in MAST by tuning neutral beam power, magnetic field and plasma current in order to keep the plasma temperature and density profiles, and thus non-scanned dimensionless parameter profiles, similar.[111] Scans were performed to determine the $\nu_*$ and $q$ dependences of $\tau_E$, with significant dependences found in both. The results, shown in Figure 18 a and b (taken from Valovic et al.[111]), are consistent with the scaling

$$B\tau_E \propto \nu_*^{-0.82\pm0.1}q_{eng}^{-0.85\pm0.2} \tag{17}$$

As can be seen in each scan, the other dimensionless variables were held fixed to within 10% in most cases.

The dimensionless variable scaling was extended further through studies on NSTX.[101] As discussed in the previous section on dimensional scalings, differences emerged in the $I_p$ and $B_T$ dependences on NSTX when comparing discharges with boronized walls versus those with lithium wall conditioning. By constraining to limited ranges on both $\beta$ and $q$ to define subsets of data from each condition, it was found that these differences could be reconciled by expressing the normalized confinement as a function of collisionality. Figure 19a-c, taken from Kaye et al.,[101] show the constrained data plotted as a function of collisionality. There was a variation of $\rho_*$ across this range of collisionality, and this effect was taken into account by assuming three different dependences of normalized confinement on $\rho_*$, with $B\tau_E \propto \rho_*^{0,-2,-3}$, reflecting a zero, Bohm and gyroBohm dependence. The fits $-0.79 < \alpha_\nu < -1.21$ for the assumptions on the $\rho_*$ dependence. Note that the boronized wall discharges do not achieve as low collisionality as the lithiated wall ones, although there is overlap between the two subsets in the $\nu_{e,*} \sim$ 0.1 range. In this range, the normalized confinements of the two subsets are the same.

Dimensionless variable scaling studies have also been conducted in Globus-M neutral beam heated discharges with $B_T$ up to 0.5 $T$.[97] Formal MLR of the Globus-M data found that

$$B\tau_E \propto \rho_*^{-2.7\pm0.12}\beta^{1.45\pm0.3}\nu_*^{-0.45\pm0.1}q^{0.85\pm0.05} \tag{18}$$

While this expression certainly indicates near gyroBohm scaling in terms of the $\rho_*$ dependence, and a favorable, but not as strong dependence on $\nu_*$ as in MAST and NSTX, the dependence on $q$ is actually inverted from that derived from MAST data (see Eqns. 15 and 17). It was pointed out by the authors of this work that the Pearson correlation coefficients indicated strong correlations among the variables, especially between $\beta$ and $q$, which could account for the very different dependence. The addition of Globus-M2 data at higher $B_T$ (up to 0.8 $T$) allowed for almost a factor of two lower collisionality than in the Globus-M dataset, and the resulting scaling with collisionality was found to be $B\tau_E \sim \nu_*^{-0.74}$ (see Figure 20, taken from Kurskiev et al[103]), correcting for the $\rho_*$ variation by assuming either a Bohm ($\rho_*^2$) or gyroBohm ($\rho_*^3$) dependence. The key finding here, is that, while the dependence on collisionality tends to become weaker at lower collisionality in higher aspect ratio devices,[109] the Globus-M and M2 ST dataset indicates that as collisionality decreases the dependence actually strengthens, as is inferred by the results in Equation 18 and 20.

As was done for the engineering variables, the ST data from NSTX and MAST were combined with the conventional aspect ratio data in the H-mode database to explore the scaling trends of normalized confinement with the dimensionless parameters.[104] The ST data had some, but not a major, effect on these combined scalings, which still showed a near gyroBohm dependence on $\rho_*$, a strong degradation with $\beta$, and a weak, but now slightly favorable scaling with $\nu_*$. Applying different techniques that take into account data uncertainties, device weightings and different approaches (transforming engineering variable exponents vs direct regression) led to some variation in the dimensionless variable exponents (see Table 2b in Kaye et al.[104]), but the general trends for $\rho_*$ and $\nu_*$ remained the same. There was a strong correlation between $\beta$ and inverse aspect ratio $\epsilon$ in the database, which led to larger variations and correlated changes in the exponents of these parameters.

The local transport results in NSTX and Globus-M2 reveal the source of the strong favorable $\nu_*$ scaling in those devices, and especially why the different engineering scalings in NSTX discharges with different wall conditioning techniques are reconciled by examining the collisionality dependence. As was shown in Figure 14, the electron temperature broadened for boronized wall conditioned NSTX discharges as $B_T$ increased, leading to reduced electron thermal collisionality. While $I_p$ was held fixed in Figure 14a, a similar result was found for increasing $B_T$ at constant $q$; as $B_T$ increased and collisionality decreased, the $T_e$ profile broadened in the mid-plasma region. This is also seen for lithium wall conditioned NSTX plasmas in Figure 21, taken from Kaye et al.,[101] where the lithium conditioning was able to produce plasmas at even lower collisionality. There was an associated decrease in electron thermal diffusivity in the mid plasma region for these plasmas as well. Figure 22a and b, also taken from Kaye et al.,[101] show the $\chi_e$ profiles themselves, and the profiles normalized to the gyroBohm $\rho_{e,*}$ parameterization ($\propto \rho_s^2 c_s/a$) respectively, color coded by collisionality, and the drop in $\chi_e$ is apparent. Interestingly enough, as the collisionality decreased, the ion thermal diffusivity, which was within a factor of two of neoclassical at the highest collisionalities, became more anomalous by a factor of four to five.

Globus-M shows an increase in $T_e$ across the entire profile, and possibly a more peaked $T_e$ profile, at lower collisionality (Figure 23a, taken from Kurskiev et al.[97]). Accompanying this is a reduction in $\chi_{\text{eff}}$ (one-fluid effective $\chi$) from the very core to $r/a \sim 0.6$ to 0.7 (Figure 23b). Beyond this radius, the uncertainties in $\chi_{\text{eff}}$ are too large to draw any conclusions. It is worthwhile noting that while the decrease in $\chi_e$ in NSTX occurs outside the very core of the plasma, the reduction of $\chi_{\text{eff}}$ in Globus-M2 in most noticeable in the very core. In NSTX, it is highly possible that the electron transport in the very core is driven by high frequency energetic particle-driven instabilities, and not the ambient plasma turbulence.[105]

## IV. Momentum Transport

The toroidal rotation in neutral beam heated ST plasmas was found to be high, with thermal Mach numbers, $M_{th} = v_\phi/v_{th}$ up to 0.7 on MAST,[111] and rotation velocities up to 1.6 times the carbon thermal velocity in NSTX.[113] Because of the relatively low toroidal fields in STs, these high rotation velocities are associated with large rotation shear ($\gamma_e \propto$

$E/B$). Although geometric effects play a dominant role in suppressing the low-$k$ electrostatic instabilities in STs, the stabilizing role of strong $E \times B$ shear can be additive.[1,25,114] An effect of $E \times B$ shear even on electron-scale turbulence was found on NSTX, where the $E \times B$ flow shear rate, $\omega_{E\times B}$, was comparable to the electron temperature gradient (ETG) mode linear growth rate, $\gamma_{ETG,lin}$. Enhanced high-$k$ turbulence was effectively suppressed when $\gamma_e > \gamma_{ETG,lin}$ even when the experimental electron temperature gradient exceeded the critical gradient for ETG.[115] Flow shear can also have a strong effect on MHD stability,[116] including its effect on sawteeth[117] and stabilization of the Resistive Wall Mode.[118]

Both steady-state and perturbative momentum transport studies were carried out in neutral beam heated H-mode discharges in NSTX.[119,120] An increase in rotation velocity by 50% was associated with an increase in toroidal field from 0.35 to 0.55 $T$ at fixed plasma current. The rotation profile remained fairly constant over this range of $B_T$, as did the applied torque profiles; therefore, the steady-state analysis indicated a reduction in the momentum diffusivity by up to a factor of four across the profile. On the other hand, at fixed toroidal field, while there was an increase in plasma rotation with increasing current, this was due more to a change in applied torque than in momentum transport; the momentum diffusivities showed little change over the variation in current. The momentum diffusivity was insensitive to the amount of lithium deposition except at the highest evaporation and lowest input torque levels, where the diffusivity values were decreased by slightly less than a factor of two in the outer region of the discharge.[100] No dependence was seen in the inner region of the plasma. The magnitude of the steady-state momentum diffusivities inferred from experiment in the outer portion of the plasma, $r/a$ ~0.65, generally yielded Prandtl numbers, $P_r = \chi_\phi/\chi_i$ in the range of 0.2 to 0.5.

Perturbation experiments performed using magnetic braking due to applied $n = 3$ non-resonant magnetic perturbations revealed inward momentum pinch velocities of 10 to 40 $m/s$. These significant inward pinches led to momentum diffusivities up to 7 $m^2/s$ (Figure 24, taken from Kaye et al.[120]), larger than those determined by steady-state analysis and with corresponding Prandtl numbers in the range from 0.5 to 0.8. The Prandtl numbers in the inner region of the NSTX plasmas were lower. Analysis of MAST L-modes using steady-state analysis[121] exhibited a similar range of Prandtl numbers, with $P = \chi_\phi/\chi_i \sim 1$ for $r/a$ ~0.1 to 0.7, but decreasing farther towards the edge (Figure 25, taken from Meyer et al.[121]).

The inferred pinch velocities in NSTX were compared to those predicted by the theories of Peeters[122] and Hahm,[123] which were based on momentum transport drive from low-$k$ turbulence. Both theories found $v_{pinch} \propto \chi_\phi/R$, although the Peeters theory included an additional dependence on density gradient scale length, $L_n$. A comparison of $v_{pinch}$ values in the outer region of the NSTX plasmas is shown in Figure 26, taken from Kaye et al.[120] While both theories give reasonable agreement with the valued inferred from experiment for low $v_{pinch}$, the Peeters theory appears to fit better for larger $v_{pinch}$, which is where $L_n$ tends to be smaller. Neither theory fits the data well in the inner region ($r/a \leq 0.35$), consistent with linear gyrokinetic simulations that indicate ITG/TEM modes are unstable in the outer region, where there is agreement, but stable in the core, where the agreement is poor.

The Peeters theory dependence on density gradient scale length also explains the apparent reduction in Prandtl number towards the edge in the MAST L-mode discharges (Figure 25, taken from Kaye et al.[120]). In this region, $L_n$ is small, and if considering an effect of an inward pinch, would lead to a $\chi_\phi$ two times greater than that inferred from the steady-state analysis shown in the figure. This would bring the Prandtl number closer to 1. Linear gyrokinetic calculations in the outer radii of these NSTX H-mode plasmas, which predict the dominance of microtearing modes, however, indicate a weak or outward convection of momentum, inconsistent with the experimental observations.[124]

It is worth noting here that $\chi_\phi/\chi_i \sim 0.5$ to 1, reflecting a low-$k$ turbulence drive, in both NSTX and MAST H-mode discharges despite the ion energy transport being close to neoclassical in both devices. While the neoclassical ion energy transport is large and dominates any residual ion energy transport due to low-$k$ turbulence, the neoclassical momentum transport is near zero and subdominant to that induced by whatever level of electrostatic low-$k$ turbulence exists in these plasmas. Thus, the momentum transport, and not the ion energy transport in ST H-modes can be used as a probe of the residual electrostatic low-$k$ turbulence.

Perturbation experiments using magnetic braking techniques similar to those used in NSTX were performed in MAST L-mode plasmas[125] . These low $\beta$ targets complement the studies in high $\beta$ NSTX H-mode discharges. Linear gyrokinetic calculations suggested that dominant low-$k$ electrostatic turbulence could lead to only a weak pinch, or even outward convection. While this was consistent with observations, the experimental uncertainties were too large to provide a true quantitative validation of the theory predictions.

Intrinsic rotation increasing in the co-$I_p$ direction with increasing density has been observed in both NSTX[126] and MAST[127] . In NSTX, the carbon intrinsic rotation was measured by passive charge-exchange in the outer part of the discharge following ohmic L to H transitions. The magnitude of the rotation was found to be correlated strongly with the carbon ion temperature gradient, and a simple theoretical treatment was employed to determine the intrinsic torque due to Ion Temperature Gradient Modes. The intrinsic torque was found to scale as $\hat{s}\chi_i/L_{Ti}$, where $\hat{s} = (r/q)dq/dr$, and general agreement was found between theory and experiment for $\chi_i$ in the range of 0.5 to 6 $m^2/s$, values consistent with those derived from NB-heated plasma transport studies in NSTX. Doppler Backscattering (DBS) measurements on MAST showed rotation reversals, from the counter-$I_p$ to the co-$I_p$ direction as density increased and normalized collisionality exceeded 1, which is the value at which that region of the discharge moved from the banana to the plateau region of neoclassical transport. This result was examined in the context of a 1-D model of the effect of neoclassical flows on turbulent fluctuations.[128,129] This balance of the intrinsic momentum flux and the turbulent diffusion was affected by the collisionality-dependent neoclassical corrections to the ion distribution function. The model, which assumed a Prandtl number of 0.7, successfully captures both the qualitative rotation reversal with collisionality as well as the trend of increasing reversal density with increasing plasma current.

## V. Particle Transport

Particle transport in STs has received less attention than heat transport, but there have been several published studies. In MAST H-modes[94] the core density profiles, fueled by core neutral beam injection and neutral penetration from the outer regions, have been observed to be rather flat. The build-up of core particle content has contributions from the neutral beam source, the neoclassical Ware pinch and the diffusive particle flux; however, in the core the first two almost fully account for the observed $dn_e/dt$, so the contribution from the particle flux is almost zero. Since the density profile is almost flat, the diffusion coefficient is indeterminate. In a NSTX H-mode plasma with a steep radially localized density gradient at $0.5 < r/a < 0.6$, the particle diffusivity in this region has been determined experimentally from particle balance (TRANSP) to lie in the range $0.2\ m^2/s < D < 1.0\ m^2/s$. A global nonlinear electrostatic gyrokinetic simulation with GTS finds a comparable particle diffusivity in this region of steep density gradient, where the particle flux is carried by low-n dissipative-trapped-electron turbulence that is relatively resistant to flow shear. Experiments with varying levels of Li wall conditioning have been carried out on NSTX. Interpretive edge transport modelling of these plasmas using SOLPS suggests that the impact of increasing Li is to reduce the effective particle diffusivity substantially in $0.8 < r/a < 0.94$ and increase it slightly in $0.94 < r/a < 1$.[100] Conceptual designs of high fusion performance steady state STs require peaked density profiles to achieve core high fusion power and efficient off-axis current drive, and clearly particle transport will be crucial.[94]

There is, however, more information regarding impurity transport. MAST experiments with a time dependent He gas-puff have revealed that in L-mode plasmas at $I_p$ =700 $kA$ and 900 $kA$, impurity transport was dominated by anomalous diffusion and an anomalous pinch, both of which decrease with increasing $I_p$ [130] . However, in an H-mode MAST experiment with comparable parameters at $I_p$ =900 $kA$ the $n_{He}$ profile peak did not penetrate inwards of mid-radius: impurity transport was close to neoclassical, with $D_{He} \sim \chi_i$, and an inward convection near the edge decreases and reverses to become outward at mid-radius.[130] Linear gyrokinetic analysis at $r/a$ ∼0.7 suggests trapped electron modes (TEM) are responsible for anomalous impurity transport in L-mode, and that TEM are stable in H-mode because $R/L_n$ is lower. Subsequently the L-mode discharge at $I_p$ =900 $kA$ was repeated using gas-puffing of C and N, to assess the Z dependence of light impurity transport spanning from He to N.[131] These experiments show a weak screening of C and N from the core, while the He profile was found to be peaked. Impurity transport coefficients in N and C were consistent with neoclassical theory for $r/a < 0.4$, but anomalous further out: $D_{N,C} \sim 1 - 10\ m^2s^{-1}$, with a strong inward convective pinch $V_{N,C} \sim -40\ m/s$ near the plasma edge that becomes outward at mid-radius (see Figure 27, taken from Henderson et al.[131]). These features are well described by the combination of neoclassical theory with a quasi-linear calculation of the anomalous impurity transport (which is attributed to the trapped electron mode for these plasmas).[131]

Perturbative experiments using Neon gas injection into L-mode NSTX discharges found that the Ne impurity did not penetrate inside $r/a \sim 0.5{-}0.6$ before the onset of MHD activity and the measured impurity diffusivities were both compatible with neoclassical predictions and consistent with the low observed level of ion heat transport.[132,133]

Sources and transport of lithium and carbon were studied in lithium wall conditioned ELM-free NSTX discharges.[134] It was found that while carbon accumulation was observed in the plasma core, lithium densities remained below 1% of the electron density.

Lithium erosion at the divertor plate was found to be consistent with physical and temperature-enhanced erosion[135] while the application of lithium on graphite plasma facing components led to a moderate reduction in carbon sputtering. Toroidal asymmetries in divertor impurity influxes were analyzed due to leading edges of divertor tiles (for carbon) and the toroidally asymmetric deposition from the lithium wall conditioning evaporators (for lithium).[136] The latter toroidal asymmetries, in particular, could lead to inaccuracies in determining the total source of lithium impurities. Parallel scrape-off layer transport studied with the fluid edge transport code UEDGE indicated stronger diverter retention for lithium impurities compared to carbon due to their shorter ionization mean free path and weaker classical parallel forces.[137]

The core transport codes NCLASS, NEO and MIST were used to study the impact of lithium conditioning on both the lithium and carbon core radial transport. It was found that changes in neoclassical transport due to changes in the deuterium temperature and density profiles together with the disappearance of ELMs could account for the increased carbon content in lithium wall conditioned discharges, although residual anomalous transport was needed to reproduce the evolution of the carbon profiles. Enhanced outward lithium transport due to the collisional coupling between that species and carbon could account for the lack of lithium accumulation, although the calculations also showed quantitatively that a reduced edge source of lithium was necessary to account for the low lithium density, consistently with the stronger divertor retention observed in the UEDGE simulations. The intrinsic impurities were found to behave neoclassically in H-mode discharges with boronized walls.

## VI. Internal Transport Barriers

A requirement for fusion power plants of any aspect ratio is to operate with low recirculating power by maximizing the plasma self-driven current, known as bootstrap current. This motivates the development of plasma scenarios with the large pressure gradients needed to drive bootstrap current. Of course, tailoring and controlling the pressure profiles is necessary to maintain plasma stability while simultaneously optimizing the self-driven current. Internal Transport Barriers (ITBs) have been explored as one route to this goal. Akin to the Edge Transport Barrier that is typical of H-mode plasmas, ITBs form farther towards the core, and they can manifest in all or some of plasma profiles of electron temperature, density, ion temperature and plasma rotation. These ITBs are tightly coupled to either or both the magnetic or rotational shear, depending on the channel.

The development of ITBs has been observed in both MAST and NSTX L-mode plasmas. Early reports of ITBs in MAST indicated their formation with early neutral beam injection into low density ($1.5 \times 10^{19}\ m^{-3}$) L-modes during the current ramp-up phase with either co- or counter-$I_p$ injection.[138,139] In these plasmas, the L-H transition was suppressed by using low field side fueling and operating in a disconnected (slightly lower) Double Null Divertor configuration; both serve to raise the L-H power threshold. In these early studies, it was noted the ITB region, taken to be the location of the strongest profile gradients, generally correlated with rotation or magnetic shear, $\hat{s}$, and especially where $\hat{s}$ was negative. In the studies on MAST, the $q$ and magnetic shear profiles were determined from magnetic diffusion calculations in TRANSP. With co-injection, ITBs were seen in the $T_i, T_e$ and $v_\phi$ profiles, with the $T_i$ ITB forming and developing out to $r/a$=0.4 to 0.6. In counter-injection discharges, the core rotation was found to be comparable to that with co-injection; the decrease in torque due to the enhanced lost energetic particles was compensated by the enhanced $j_r \times B$ due to the loss. In these counter-injection discharges, the ITBs were broad, with locations out to $r/a$=0.6 to 0.7, and were reported to be observed in $T_e$ and $n_e$.

Subsequent ITB studies were carried out in MAST, and these studies incorporated more detailed profile measurements, including that of the magnetic field pitch, a measurement on which the determination of the $q$ and $\hat{s}$ profiles could be made.[140,141] The more detailed comparison between co- and counter-injection ITBs indicated that the density in the counter-injection ITB tended to be higher than that with co-injection, due to a higher $Z_{\text{eff}}$, and while the total stored energy in the co-injection ITB was higher than that with counter-injection, most of that was due to the fast particle component, and the thermal stored energies in the two were comparable.

The profile and time evolutions of the magnetic shear, gradients in ion temperature and rotation profiles, along with the rate of change of plasma rotation and MHD activity is shown in Figure 28 (taken from Field et al.[140]) for the co-injection ITB. No electron temperature or density ITB is seen with co-injection. The ion temperature ITB forms near the location of $q_{min}$, while the rotation ITB is localized to a region of maximum negative $\hat{s}$, which is a few cm inside of $q_{min}$. In these plasmas, transport analysis indicates $\chi_i \sim \chi_\phi \sim \chi_{i,NC}$ inside the ITB; outside, $\chi_i/\chi_{i,NC} \sim 4$ to 10. With time, coupling of MHD modes, including energetic particle-driven modes, gives rise to enhanced neoclassical toroidal viscosity braking of the plasma rotation, reducing the rotation gradient and the strength of the $T_i$ ITB. The ITB is finally "destroyed" at the onset of an internal kink mode as $q_0 \sim 1$.

The counter-injection ITB is different from that with co-injection in several respects. The magnetic shear is only weakly negative in the core region ($r/a < 0.4$), but because of enhanced fast particle loss, the $E \times B$ shear gradient extends farther out in the plasma than for the co-injection case. The study reported in Field et al.,[140] and unlike the early studies, actually concluded that with counter-injection there were no clear indications of a maximum gradient in either $T_i$ or $T_e$, although some indication of an ITB in the density was observed. There were, however, localized maxima in $\rho_s/L_{Ti}$ related to $q_{min}$ passing through rational values. In these discharges, $\chi_e \geq \chi_{i,NC}$ and $\chi_\phi/\chi_i \sim 0.1$ to 0.3.

The statistical dependence of the $T_i$ and $v_\phi$ rotation gradients on magnetic shear is shown in Figure 29, taken from Field et al..[140] It is seen that for co-injection ITB discharges, the large $\rho_s/L_{Ti}$ and $\rho_s/L_{\omega,\phi}$ are more localized to the negative magnetic shear region. For counter-injection, $\rho_s/L_{\omega,\phi}$ evolves to higher values, and bifurcates, as $\hat{s}$ increases to more positive values. Microinstability analyses indicate that for co-injection, negative magnetic shear is sufficient to stabilize low-$k$ modes, thus supporting ITB formation; rotation shear is not necessary.

Observations of ITBs were made also on NSTX, and the analysis here focused on high-$k$, electron-scale turbulence effects.[142,143] It was found in this work that with sufficient negative magnetic shear, the electron temperature profiles were no longer stiff, and their gradients could exceed critical gradients for ETG modes by a large margin. The ITBs in the various channels formed early in L-mode discharges with either Neutral Beam or High Harmonic Fast Wave RF heating, with the formation reflected by a rapid rise in both $T_e(0)$ and $T_i(0)$.

The profile gradient scale lengths, along with $q$ and magnetic shear profiles for a developed ITB are shown in Figure 30, taken from Yuh et al.[142] It is seen that the $T_e$ ITB is slightly inside the $T_i$ ITB, and while the former is more aligned with maximum negative $\hat{s}$, a few cm inside the location of that maximum, the latter is a few cm inside the location of both $q_{min}$ and peak $E \times B$ shear. There is no $n_e$ ITB, and the rotation ITB location, as in MAST, is a few cm inside maximum negative $\hat{s}$. Consequently, while it appears that that $E \times B$ shear is important for suppressing modes that can lead to ion transport, negative $\hat{s}$ is more important for electron transport suppression.

Figure 31, also taken from Yuh et al.,[142] shows that the electron temperature profile stiffness at marginal conditions for ETG destabilization is no longer valid. For sufficiently high negative values of $\hat{s}$, $R/L_{Te}$ can be up to a factor of six greater than the critical values as determined by linear gyrokinetic calculations. This high values of $R/L_{Te}$ correspond to up to a factor of ten reduction in the measured high-$k$ turbulence amplitudes at those locations. $E \times B$ shear had little or no effect on the $T_e$ ITBs; high-$k$ turbulence was found to be suppressed using torque-free HHFW heating only, where the $E \times B$ shear was measured to be near zero. At the location of the ITBs, $\chi_i \sim \chi_{i,NC}$, and $\chi_e < \chi_{i,NC}$.

## VII. Gyrokinetic Analysis

The scaling laws described in Section II are a valuable guide to ST confinement, but understanding their ranges of validity and physical basis requires deeper knowledge of turbulent transport. Extensive investigations of microinstabilities in START, MAST, NSTX, Globus-M, and conceptual designs of burning STs[26,7] have used gyrokinetic (GK) calculations with local codes (GS2,[144] GYRO,[145] and GKW[146]), and global codes including finite $\rho_*$ effects (GTS[147] and ORB5[148,149]). This section reviews what GK calculations have revealed about core turbulence and anomalous transport in STs, focussing on heat transport; particle, impurity and momentum transport in STs are covered in Sections IV.

Beneficial impacts of equilibrium geometry on ST microstability, were uncovered in early studies motivated by START and NSTX[150,25,114]; favorable magnetic drifts allied with higher $dp/dr$ in STs, were found capable of suppressing drift-wave instabilities that drive anomalous transport.[26] Furthermore, in experiments with tangential NBI, the compact nature of the ST leads to high toroidal flows that can act to suppress the turbulence especially at ion-scales.[151] Nevertheless, trapped electron modes (TEM), driven at steep $dn/dr$, however, should be boosted in STs by the larger trapping fraction, and at the high $\beta$ accessible to STs[44,93] electromagnetic modes including kinetic ballooning modes (KBMs),[152,153] microtearing modes (MTMs),[154,155] and fast particle driven Global and Compressional Alfven Eigenmodes (GAEs, CAEs)[105,156] may become unstable and complement the usual electrostatic ion and electron temperature gradient, ITG and ETG, driven modes.

ST heat losses through the ion channel are often close to neoclassical in the plasmas and collisionalities accessed in ST H-mode plasmas so far,[157,158,93,159,160] but they become more anomalous at lower collisionality in NSTX.[101] The ion neoclassical transport in STs is higher than that at conventional aspect ratio; nevertheless, the ion thermal transport was inferred to still be less than that of the electrons. Therefore, electron heat transport, which usually dominates, has received more attention.[161,162] The following sections review GK studies, organized by mode type and binormal wavenumber $k_y\rho_{*,ii}$ of ST core plasmas, as well as more holistic microstability analyses for selected topics, including H-mode pedestal, lithium conditioning, pellet fuelling, high power, and long pulse plasmas.

## A. Ion scale modes at $k_y\rho_i \leq O(1)$: (excluding MTMs)

Local microstability studies have identified a range of unstable modes at $k_y\rho_i \leq O(1)$ in the core of STs. In MAST L- and H-modes these include: ITG and TEM driven at higher $R/L_n$,[155,152,163] the 'ubiquitous mode'[164,165]; electromagnetic modes destabilized by finite-$\beta$ including KBM and MTM (MTMs will be discussed in the next section).[152] Similar modes are also found in NSTX, where broader ranges in $\nu_*$ and $\beta$ are accessible. In low $\nu_*$ NSTX H-modes, hybrid TEM/KBM modes become unstable at the edge and may be linked with increasingly anomalous $Q_i$.[101] In a high $\beta$ NSTX plasma GYRO finds an electromagnetic hybrid ITG-KBM mode (destabilized by $\delta B_\parallel$) dominating ion-scales at $r/a$=0.7.[166] GLOBUS-M finds $R/L_{Te}$ is constant and clamped by TEMs at mid-radius at the lower $\nu_{e,*}$ end of an Ohmic density scan.[89] $R/L_{Te,crit,TEM}$[167] and $\tau_E$ increase while $R/L_{Te,crit,ETG}$[168] decreases with increasing $n_e$, until $\tau_E$ saturates at a transition from TEM to ETG turbulence above $n_e \sim 2.5 \times 10^{19}\ m{-}3$.[89]

Global nonlinear electrostatic simulations of ion-scale turbulence in various NBI-heated NSTX plasmas have been performed using the global GTS code, which excluding $\delta B$ and electron-scales, often underpredicts $Q_{e,exp}$. In a strongly rotating L-mode, GTS finds KH/ITG turbulence at $0.6 < r/a < 0.8$, with $Q_{i,GTS} \sim Q_{i,exp}$, but $Q_{e,exp}$ dominates and $Q_{e,GTS} \ll Q_{e,exp}$.[169] In an NBI heated H-mode, $Q_{i,exp} \sim Q_{i,GTS} + Q_{i,NC}$ before and after an $I_p$ rampdown, with negligible ion-scale turbulence in the latter state,[170] but the larger $Q_{e,exp}$ is still underpredicted. Interesting results for an H-mode with steep density, temperature and rotation gradients at mid-radius, find dissipative dominating over collisionless TEMs, as the longer wavelength DTEM is more robust to $\nu_{e,*}$ and $\gamma_E$.[169,171] The DTEM turbulence saturates as a large-scale quasi-coherent eddy with few toroidal modes. While $\Gamma_{GTS}$, $Q_{i,GTS}$ and $\chi_{\phi,GTS}$ all compare with experiment in $0.5 < r/a < 0.6$, $Q_{e,GTS} \sim Q_{e,exp}/4$. The fluxes have minima in $\nu_{e,*}$ at the CTEM-DTEM transition (see Figure 32, taken from Wang et al.,[169] suggested as a potential performance sweet spot for future STs.[172] Above the minimum $Q_{e,i,DTEM}$ increases with $\nu_{e,*}$ aligning qualitatively with the ST scaling $\tau_E \propto \nu_*{}^{(-1)}$.[93,111]

There is broad support from for flow shear suppression of turbulence in STs, where equilibrium flow shear, $\gamma_E$, often exceeds growth rates, particularly for ion-scale modes in plasmas with tangential NBI. Nonlinear GS2 simulations including $\gamma_E$ (but neglecting Coriolis and centrifugal effects[146]) at mid-radius in a MAST H-mode, find that toroidal flow shear can completely suppress ion-scale turbulence.[173] ST geometry facilitates this because the turbulence suppressing perpendicular component of flow shear, $\gamma_E = dv_\perp/dr$, is enhanced by the high value of $B_\theta/B_\phi \sim q/\epsilon$, while the parallel component, $\gamma_p = dv_\parallel/dr$, that drives KH and Parallel Velocity Gradient (PVG) turbulence[174] is reduced. Direct experimental evidence for flow shear suppression of ITG comes from NBI heated MAST L-modes, where local $R/L_{Ti}$ measurements increase with increasing $\gamma_E$ and decreasing $q/\epsilon$.[175] An inverse correlation is also observed between $R/L_{Ti}$ and the gyro-Bohm normalized ion heat flux (estimated using BES), $Q_{i,BES}/Q_{GB}$, indicating $R/L_{Ti}$ is close to a critical threshold where $Q_{i,ITG} \sim Q_{i,NC}$.[175] Theory calculations of sub-critical PVG-ITG turbulence at zero magnetic shear[176–178] find that the weaker transient mode amplification factor $\propto e^{q/\epsilon}$ in STs, should make them more resilient to such turbulence.

Ion-scale turbulence is observed outside internal transport barriers (ITBs) in co-NBI MAST L-modes. Steep $dT_i//dr$ and $d\Omega_\phi/dr$ form at the ITB just inside $q_{min}$, where $\hat{s} < 0$. Negative magnetic shear is found using GS2 to be sufficient to suppresses all modes in the ITB, even neglecting $\gamma_E$.[140] Similar findings were reported for low $\hat{s}$ in a high $\beta$ NSTX plasma.[166] Outside the ITB, where $\hat{s} > 0$ and $\gamma_E$ is weaker, GS2 finds ITG modes resilient to flow shear that have growth rates boosted by kinetic electrons.[140] Global ORB5 simulations, with kinetic electrons and flow shear, confirm this and predict significant ITG turbulence outside the ITB.[179] ORB5 simulations find that flow shear stabilization is asymmetric with respect to the sign of $\gamma_E$ owing to global effects, and that ITG turbulence spreads a short distance into the linearly stable region inside the barrier albeit impeded by stronger flow shear inside the ITB. BES measures ion-scale density fluctuations consistent with ITG turbulence at the edge of similar plasmas. BES turbulence correlation lengths, but not correlation times, are consistent with nonlinear ORB5 simulations.[180] Local GS2 simulations of the same plasma were post-processed using a synthetic diagnostic to reconstruct the BES data,[181] and reproduced $Q_{i,exp}$ but with significantly lower fluctuation amplitudes. These found reasonable agreement with all measured turbulence correlation properties apart from the radial correlation length.[182] GS2 reveals that this turbulence is sub-critical, with $R/L_{Ti}$ and $\gamma_e$ very close to threshold.[183]

Ion-scale turbulence simulations scanning in $R/L_T$ pass through the turbulence threshold and expose a transition between two distinct turbulent states.[183] Near threshold turbulence is dominated by sparse, long lived, spatially large, and intense structures generating low transport. As $R/L_T$ increases above threshold the density of large-scale fluctuations rises, until they interact to break up into the more familiar sea of small, weak, volume-filling fluctuations causing higher transport (see Fig. 33, taken from van Wyk et al.[183]). Close to threshold up-down symmetry is broken by flow shear induced tilting of the spatial correlation function, but symmetry is restored at high $R/L_T$[183]). This symmetry breaking tilt is observed experimentally in MAST BES measurements, suggesting ion scale turbulence is close to threshold.[184] The BES estimated normalized ion heat flux in MAST depends strongly on radial correlation length and tilt but is insensitive to flow shear.[185] Significant poloidal velocity fluctuations, consistent with ion-scale zonal flows, are observed in velocimetry analysis of low-frequency filtered BES data (and in DBS), and may supplement equilibrium flow shear in generating the tilt.[185]

Extensive analysis of BES ion-scale density fluctuation data from MAST L-mode, H-mode and ITB discharges reveals a grand critical balance where times associated with fluctuation decorrelation, parallel streaming, diamagnetic drift, and magnetic drift are all comparable: $\tau_c \sim \tau_{st} \sim \tau_* \sim \tau_M$.[186,185] This demonstrates the turbulence is 3D and anisotropic with $l_\parallel > l_y > l_x$. The nonlinear time estimated from drift waves is too long to explain the much shorter turbulence correlation time. Postulating that zonal flows (not measured directly by BES) decorrelate the turbulence instead, requires a ratio of zonal to drift waves $|\delta\Phi_{ZF}|/|\delta\Phi_{DW}| \propto \nu_{*,i}^{-0.8}$, which is consistent with previous literature.[187]

## B. Microtearing Modes at Ion (and sub-ion) scales

MTMs generate magnetic islands on rational surfaces that tear confining flux surfaces and generate predominantly electron heat transport. They are driven by $R/L_{Te}$ and propagate in the e-direction with frequency $\omega \sim \omega_{*,e}$. MTMs dominate over ITG at $k_y\rho_i < 1$ at mid-radius in MAST, NSTX and GLOBUS-M H-mode plasmas where local $\beta_e$ ~5 to 10%.[154,155,188] Their eigenfunctions have a complex multiscale character: $\delta\Phi$ is highly extended in ballooning angle $\theta$ and has high radial wavenumbers, while $\delta A_\parallel$ is localized in $\theta$ and radially extended. Other linear properties include[152,189,190]: critical thresholds in $\beta$ and $R/L_{Te}$; instability over a wide

$\nu_e/\omega$ range that peaks at $\nu_e/\omega = O(1)$[189,190]; high $|R/L_n|$ is stabilizing; $\gamma_{MTM}$ is sensitive to $R/L_{Te}$, $\nu_{ei}$, $R/L_n$, $\beta$, $R/L_p$, and $\hat{s}$; weak sensitivity to poloidal shaping[190]; width of the perturbed current layer, $d = O(\rho_i)$[189,191]; and insensitive to $\delta B_{\parallel}$ and kinetic ions.[152] MTMs are unstable in simplified circular $s-\alpha$ model fits to MAST, where scans[189,192] find: magnetic drifts are destabilizing; trapped particles destabilize at low $\nu_{e,*}$ but stabilize at high $\nu_{*,e}$; instability arises over a finite window in $\beta$ (e.g. $0.05 < \beta < 0.35$); and MTMs are stable if both $\delta\Phi$ and drifts are excluded. Artificially removing energy dependence from GS2's collision operator has weak impact on $\gamma_{MTM}$ (when drifts are included),[152,189,192] which is essential for instability in most analytic theories.[193–197] MTMs are also unstable in the shallow gradient plateau inboard of the pedestal top in MAST[198,199] and NSTX.[200] Edge MTMs exhibit most properties of core MTMs,[189,190] with two key differences: $\delta\Phi$ is less extended along the field line because of higher magnetic shear; and $\gamma_{edge,MTM}$ can be maximal at $\nu_{ei}$=0 indicating a collisionless drive,[199,200] and not at finite $\nu_{ei}$ as in the ST core.[189,190] NB core nonlinear simulations for NSTX find $q_{e,MTM} \sim \nu_{ei}$[191] and is consistent with the confinement scaling $B\tau_E \sim \nu_*^{-1}$.[93,111] This simulation result depends on $\gamma_{MTM}$ decreasing with decreasing $\nu_{ei}$. Collisionless MTMs are reported by several authors,[201,202] while others find collisions essential for instability.[203] $\gamma_{edge,MTM}$ increases strongly with trapped particle fraction, and Figure 34, taken from Dickinson et al.[199] illustrates $\gamma_{edge,MTM}$ dependence on $\nu_{ei}$ and inverse aspect ratio $\epsilon$. Electron drift, precession, and bounce frequencies are comparable to the mode frequency, challenging usual analytic theory approaches. The linear drive mechanism for MTMs is complex,[189,190,199] and yet to be fully understood analytically. While MTMs were first found frequently to be dominant in STs, it is increasingly realized that MTMs also impact on conventional aspect ratio tokamaks including in internal transport barriers and in the H-mode pedestal.[204–207]

MTMs dominate at $r/a$=0.6 in a collisional high $\beta$ ($\beta_e \sim 0.1$) NSTX H-mode.[93] $\gamma_{MTM}$ peaks for $\nu_{ei}$ in the range $1 < Z_{\mathrm{eff}}\nu_{ei}/\omega < 4$, with the experimental $Z_{\mathrm{eff}}\nu_{ei}$ typically below the peak where increasing $Z_{\mathrm{eff}}$ is destabilizing.[190] $\gamma_{MTM}$ dependences on $\hat{s}$, $q$ and $\hat{s}/q$ are non-monotonic, but around the experimental value on this surface increasing $\hat{s}/q$ is destabilizing (for $0.6 < \hat{s}/q < 1.3$) though this becomes stabilizing for $\hat{s}/q > 2$ due to increased field-line-bending. Locally this results in $\gamma_{MTM}$ and $\gamma_{ETG}$ having opposite trends with $Z_{\mathrm{eff}}$ and $\hat{s}/q$, which may help distinguish modes experimentally. At $r/a > 0.8$, KBMs (or hybrid ITG/KBMs) at lower $k\rho_i \sim 0.15 - 0.35$ become dominant over MTMs, especially at high $|R/L_n|$, $\beta_e$, and low $Z_{\mathrm{eff}}\nu_{ei}$.

MTMs play a role in the $\tau_e \propto \nu_*{}^{-1}$ scaling, which was verified over an extended $\nu_*$ range in NSTX using lithium wall conditioning, and is attributed to reduced $Q_e$ at lower $\nu_*$ for $\rho > 0.5$.[101] Local $\nu_{e,*}$ variation is large at $\rho$=0.6: at high $\nu_{e,*}$ MTMs are virulent with

$\gamma_{MTM} \gg \gamma_E$: at lower $\nu_{e,*}$ , $\gamma_{MTM}$ is reduced by $\gamma_E$. Farther out at $\rho$=0.7, the hybrid TEM/KBM is unstable over a wider radial range at lower $\nu_{e,*}$ due to an increase in $T_e/T_i$, though its influence on $Q_i$ is unclear, as $\gamma_{KBM-TEM} \sim \gamma_E$. NSTX and MAST collisionality scans were performed with $\nu_{ei}$ below the peak in $\gamma_{MTM}(\nu_{ei})$, where growth rates align with $\tau_e \propto \nu_*{}^{-1}$ scaling.[190,111] The weaker scaling $\tau_e \propto \nu_*{}^{-0.4}$ at GLOBUS-M may be explained by $\nu_{ei}$ in the scan ranging beyond the peak in $\gamma_{MTM}(\nu_{ei})$.

Higher wavenumber MTMs are robustly unstable at $3 < k_y\rho_i < 15$ in the core of HHFW heated NSTX L-modes, where $q_0 \sim 3$ is higher than in typical H-modes, $\hat{s}$ is low, and core values of $\beta_e \sim 5\%$[204] Similar MTMs also dominate sub-$\rho_i$-scales at mid-radius in a conceptual burning ST.[7] While $\delta\Phi$ eigenfunctions are less extended in ballooning angle than for core MTMs,[155,190] radial wavenumbers are similar as $k_y\rho_i$ is higher.[204] At outer radii, MTMs are stable at lower $\beta_e$ and ETG is the dominant instability. $\gamma_{MTM}$ increases with $R/L_{Te}$ and $\nu_{ei}$, and is higher in D than in He plasmas.[204]

First estimates of MTM transport were for a beam heated NSTX H-mode with $P_{nb} = 6\ MW$,[205] where MTMs at $0.1 < k_y\rho_i < 1$ dominate in the steep $dT_e/dr$ region at $0.4 < r/a < 0.75$.[205] Nonlinear MTM theory predicts magnetic fluctuations scale as $\delta B/B \sim \rho_e/L_{Te}$,[206] suggesting large $\delta B/B$ in low $B$ machines (as for typical STs). MTMs saturate nonlinearly to form overlapping islands centred on different rational surfaces, and electron heat transport can be estimated using a simple test-particle transport model from stochastic magnetic fields.[207] In the collisional limit (valid for the plasma), this gives a model heat diffusivity, $\chi_{e,MTM} = (\rho_e/L_T)^2 v_{th,e}^2/(\nu_{ei} q)$ that predicts substantial transport at mid-radius with $\chi_{e,MTM} \sim 0.5\chi_{e,exp}$.[205] If this model dominated heat loss, the associated energy confinement time scaling would be consistent with $\tau_E \sim a^2\chi_e \propto B$ reported for STs.[112,111] Another electron heat transport mechanism is required for $r/a < 0.3$, where $T_e$ is too flat to drive MTMs. In NSTX discharges with core $\hat{s} < 0$, however, core confinement improves with the suppression of MTMs and $\chi_e$.[205]

Nonlinear local GYRO calculations[208,191] were performed at $r/a = 0.6$ in the MTM dominated collisional high $\beta$ NSTX H-mode mentioned previously (where ETG is stable),[191] including kinetic electrons and ions and electron pitch angle scattering, but neglecting $\gamma_E$. Nonlinear MTM simulations are challenging and attempts for MAST with GS2, failed to saturate due to unexplained nonlinear instability of the highest $k_x$ modes on the grid.[164,192] These are demanding because of the need to capture both the rational surface spacing and fine radial scales in $\delta\Phi$. Grids used $\leq 16$ binormal wavenumbers $0 < k_\theta\rho_s < 0.75$, and $\leq 540$ points in a radial domain extending $80\rho_s$. In the saturated state, shown in Figure 35, taken from Guttenfelder et al,,[191] $\delta n_e$ fluctuations peak off the outboard mid-plane and have correlation lengths $L_x \sim 0.7\rho_s \ll L_y \sim 4\rho_s$, while $\delta A_\parallel$ approaches the box scale in radius and peaks at the lowest resolved finite $k_\theta \rho_s$. Magnetic flutter carries 98% of the heat flux and $Q_e \gg Q_i$. $\chi_{e,sim} \sim 1.2\chi_{GB}$ is consistent with $\chi_{e,exp}$, and with a collisionless Rechester-Rosenbluth estimate[207] following[205] giving $\chi_{e,mod} \sim 0.92\chi_{e,GB}$. Simulations are broadly consistent with nonlinear MTM theory expectation $\delta B_r/B \sim \rho_e/L_{Te}$.[206] Scans (see Figure 36 from Guttenfelder et al.[191]) in this parameter range find that $\chi_e/\chi_{GB}$ increases sharply with $R/L_{Te}$ and with $\beta_e$ above critical values that exceed linear thresholds, and scales almost linearly with $\nu_*$*. Restarting a saturated simulation with the experimental $\gamma_E$, however, largely suppressed the MTM turbulence, though artificially increasing $R/L_{Te}$ by 20% partly restored $q_{e,MTM}$ to a level 3x smaller than $q_{e,exp}$.[191]

Transport predictions for an NSTX discharge were obtained using reduced models of MTM heat transport: RLW[209]; and a model by Wong et al.[210] RLW, which is independent of $\nu_*$ and $\beta$, was better and gave reasonable matches to $T_{e,exp}$ at radii and times where GK finds unstable MTMs.[211] The multi-mode transport model was recently upgraded to included MTMs, which improves $T_e$ predictions for a high $\nu_*$ NSTX plasma.[212]

## C. Electron Scales: ETG Modes

ETG modes, the electron-scale analogue of ITG, can produce substantial electron heat transport with $\chi_e \gg \chi_{e,GB}$,[213,214] and are unstable for $R/L_{Te} > R/L_{Te,crit,ETG}$. An empirical formula for the ETG threshold for typical core condition[168]

$$\frac{R}{L_{Te,crit,ETG}} = Max[(1+\frac{Z_{\text{eff}}T_e}{T_i})(1.33+1.91\frac{\hat{s}}{q})(1-1.5\epsilon)(1+0.3\epsilon\frac{d\kappa}{d\epsilon}), 0.8R/L_n] \tag{19}$$

captures the stabilizing impacts of impurities (demonstrated for MAST[215]), $\hat{s}/q$, and density gradients, but is not expected to be accurate at high $\beta$ or $dP/dr$, $\hat{s} \leq 0$, or with strong shaping. ETG is sensitive to finite $\beta$ effects particularly from $\delta B_\parallel$,[114,216,217] and both $\delta B_\parallel$ and full $v_{\nabla B}$ must be retained[217]: the low $k_\perp \rho_i$ approximation canceling the $\delta B_\parallel$ drive with the $dP/dr$ contribution to $v_{\nabla B}$,[218] is inaccurate for ETG even at $\beta \ll 1$.[217] In strongly rotating beam heated STs, virulent ETG modes (well above threshold with $R/L_{Te} \gg R/L_{Te,crit,ETG}$) are less susceptible to flow shear suppression than ITG, because $\gamma_{ETG} \gg \gamma_E$ while $\gamma_{ITG} \sim \gamma_E$. GK simulations and experimental data reveal regimes where ETG carries significant $Q_e$ in mid/outer radius regions of MAST and NSTX.

In MAST H-mode, at mid-radius where density is flat and $\beta \sim 0.1$, GS2 finds $\gamma_{ETG} \gg \gamma_E$ with peak growth around $k_y \rho_e \sim 0.2 - 0.3$,[155] in conditions where including $\delta B_\parallel$ reduces $\gamma_{ETG}$.[152] Collisions have little influence on $\gamma_{ETG}$ at high wavenumber where $\nu_{ei}/(\epsilon\omega) \ll 1$,[219,220] but at $\nu_{ei}/(\epsilon\omega) > 1$ reduced trapped electron drive is stabilizing at lower $k_y$.[173,220]

In NSTX H-modes, perturbative Li pellet experiments find stiff $T_e$ profiles in monotonic $q$ plasmas consistent with a critical $R/L_{Te}$,[93] $\chi_e$ profile shapes agree with an analytic electrostatic model of ETG transport,[93,221] and $\chi_e$ at $r/a = 0.65$ is in the range 5-20$\chi_{e,gB}$ expected from ETG turbulence. ETG may also play a role in discharges from an NSTX $\nu_*$ scan outside mid-radius, where $R/L_{Te} > R/L_{Te,crit,ETG}$[101] and GYRO finds $\gamma_{ETG}$ and $R/L_{Te}$ decreasing with decreasing $\nu_*$.[101] high-$k$ microwave scattering observations provide direct support for $R/L_{Te}$ driven fluctuations consistent with ETG turbulence in NSTX He plasmas heated by HHFW, where the fluctuations strikingly appear when $R/L_{Te} > R/L_{Te,crit,ETG}$ and it is found that Eq. 19 only slightly underestimates the critical gradient computed using GS2.[222,223] Flow shear suppression of ETG turbulence is possible near marginal stability and has been observed under such conditions in high-$k$ scattering observations from NSTX.[115]

Density gradient stabilization of ETG was first observed on NSTX after an ELM increased $R/L_n$ locally by a factor of 5, while $\chi_e$ halved and high-$k$ scattering found suppression of ETG density fluctuations at $k_\perp \rho_s < 10$ (consistent with linear GS2).[219,224] Later in a slowly evolving NBI heated NSTX H-mode with $R/L_n$ increasing at the high-$k$ scattering location, the fluctuations moved to lower amplitudes and frequencies in the plasma frame, supporting the stabilizing influence of $R/L_n$ on ETG.[225]

Single scale nonlinear ETG simulations are physically justified if there is a mechanism to provide a low-$k_y$ cut-off by suppressing ion-scales. First nonlinear electromagnetic simulations of ETG turbulence for a MAST H-mode used GS2 at $r/a = 0.4$, where $\beta_e \sim 0.049$ and $R/L_n \sim 0$.[226] Calculations with/without collisions, with/without kinetic ions, with various grid resolutions and neglecting flow shear found electrostatic transport dominating negligible magnetic flutter in the saturated state, with $\chi_{e,ETG} \sim \chi_{e,exp} \gg \chi_{e,GB}$. The excess over $\chi_{e,GB}$ is due to strong streamers (with $k_y \gg k_x$) and weak zonal modes, and $Q_e$ depends weakly on $\beta_e$ in spite of $\delta B_\parallel$ reducing $\gamma_{ETG}$.[227,173,217] Farther out at $r/a = 0.8$, $\hat{s}/q$ and $R/L_n$ are larger and $\chi_{e,ETG} \ll \chi_{e,exp}$. Later electrostatic GS2 simulations for the same local equilibrium, included flow shear and collisions that each individually suppress low $k_y$.[173] These calculations confirm that anisotropic ETG turbulence with $k_y \gg k_x$ gives $Q_{e,ETG} \sim Q_{e,exp}$ and is robust to the experimental level of $\gamma_e$ (see Figure 37, taken from Roach et al.[173]). ETG turbulence could, however, be suppressed by artificially increasing $\gamma_E$ to $10 \times \gamma_{E,exp} = O(\gamma_{ETG})$.[173] These findings were verified using GYRO (with non-periodic boundary conditions),[173,228] where it also noted that the anisotropic nature of ETG turbulence must be carefully accounted for on interpreting fluctuation measurements, e.g. from the NSTX high-$k$ scattering system that is sensitive to modes with $k_r = 9k_\theta$.[228]

Low-$\beta$ NSTX H-mode plasmas in a scan with $\nu_{e,*}$ spanning a factor 2.5, exhibited the energy confinement scaling, $B\tau_E \propto \nu_{e,*}{}^{(-0.82)}$[219] consistent with a scan at higher $\beta$.[93] ETG is unstable (with MTMs stable) at the high-$k$ scattering location near mid-radius where $\beta_e \sim 0.02$. high-$k$ fluctuations, however, increase at lower $\nu_*$ counter to expectation from the $\tau_E$ scaling, which is not fully understood and could be a local effect.[219]

Global electrostatic simulations of ETG turbulence in NSTX, using GTS with adiabatic ions find ETG turbulence dominated by anisotropic streamers making significant contributions to electron heat transport.[169] Turbulence saturation involves: an initial transient dominated by ETG streamers at $k_\theta \rho_s \sim 13$; subsequent transfer of energy to a high frequency e-GAM at $m = 1$; downshift of the streamer spectrum to $k_\theta \rho_s \sim 6$ with concurrent slow growth of a low frequency zonal flow. It was speculated that collisional damping of zonal flows and e-GAMs, could indirectly lead to a favorable scaling $q_{e,ETG} \propto \nu_*$ following a similar mechanism reported for ITG.[187] GTS also computed ETG turbulence in an L-mode heated only by RF before and after switching-off of the heating, which resulted in a rapid reduction of electron-scale fluctuations and $Q_{e,exp}$ dropping by a factor 2.[229] Equilibrium gradients and the simulated electron heat flux, $Q_{e,GTS}$, were, however, similar before and after cessation, and only close to $Q_{e,exp}$ in the latter state without RF: the discrepancy is not understood.

Collisionality dependence of ETG turbulence was explored at mid-radius in MAST using GS2. Artificially scanning $\nu_{ei}$ at fixed $R/L_{Te}$ reveals that the long-time saturated $Q_e$ falls with decreasing $\nu_*$, due to an evolving balance between zonal and non-zonal fluctuations.[220] At low $\nu_{ei}$, long times, $tv_{th,e}/a = O(10,000)$, were needed to reach the transport relevant saturated state. At low $\nu_{ei}$ , resistive collisional damping is weak, and zonal modes grow sufficiently large to break up the transport enhancing radial streamers that form early in the simulation. ETG turbulence is marginal in these simulations, and the saturation process differs from the standard picture developed in the strongly driven limit where zonal secondaries are weak.[213] The simulations find $Q_{e,ETG} \sim \nu_{ei}$ (see Figure 38, taken from Colyer et al.[220]), consistent with a theoretical model of interactions between resistively damped zonal modes, drift waves and linear drive.[220] This $Q_{e,ETG}$ scaling aligns with the energy confinement scaling obtained from H-modes in NSTX and MAST,$B\tau_E \propto \nu_*^{(-1)}$.[93,111]

Electron internal transport barriers (e-ITBs) were produced on NSTX at locations with $\hat{s} < -0.4$ with $\chi_e < 0.1\chi_{e,gB}$ and $R/L_{Te} \sim 20 \gg R/L_{Te,crit,ETG}$ (see Figure 39, taken from Yuh et al.[143] and Peterson et al.[230]). high-$k$ fluctuation measurements suggest local suppression of ETG turbulence in the e-ITB,[143,142] while paradoxically linear gyrokinetics finds this region is super-critically unstable to ETG (robust to the uncertainty in $Z_{\text{eff}}$). Strong negative $\hat{s}$ is the key ingredient for triggering e-ITB formation and the transition from stiff to weak ETG transport. Flow shear is thought not to be responsible, as barriers can be generated in HHFW heated plasmas where $\gamma_E \sim 0$. During the lifetime of the e-ITB, intermittent bursts of high k fluctuations grow on timescales consistent with ETG and may regulate $R/L_{Te}$ inside the barrier. Nonlinear electrostatic local GYRO simulations[143] for an RF heated NSTX e-ITB (with negligible $\gamma_E$), found significant ETG turbulence only for $R/L_{Te} \gg R/L_{Te,crit,ETG}$, and that the nonlinear upshift in $R/L_{Te}$ gets larger as $\hat{s}$ becomes more negative (see Figure 39c).[230] Above the nonlinear threshold the turbulence character changes, with off-mid-plane streamers at the top and bottom of the e-ITB flux surfaces (see Figure 39(d)). Global GYRO calculations find that ETG driven flux is comparable with experiment in the outer region of the barrier where $\hat{s}$ is less negative, and that the turbulence cannot penetrate to the inner barrier (where $\hat{s}$ is more negative and $Z_{\text{eff}}T_e/T_i$ is larger).

Electron-scale $\delta n_e$ fluctuations were measured in the core of a MAST L-mode using DBS, sensitive to modes with $k_y \gg k_r$ (c.f. $k_y \ll k_r$ from NSTX high-$k$ scattering). First results reveal that for $7 < k_\perp \rho_i < 11$, $|\delta n|^2 \sim k_\perp^{-\alpha}$, $\alpha = 4.7 \pm 0.2$,[231] where the exponent is close to 13/3 expected from a theory-based power law.[232]

Compelling evidence for transport relevant ETG turbulence comes from an extensive validation study using the NSTX high-$k$ scattering system during an $I_p$ ramp-down in a moderate $\beta$ NBI-heated discharge.[233] $R/L_n$ increases by a factor four between two times at the high-$k$ scattering location, $r/a = 0.7$, where fluctuations reduce in amplitude (see Figure 40, taken from Ruiz Ruiz et al.[233]). Improving on earlier work,[225] fluctuation measurements were compared with synthetic diagnostics based on local nonlinear GYRO simulations at both times. These demonstrate impressive simultaneous agreement for[233]: $Q_e$, fluctuation frequency spectra (which poorly discriminate between models), fluctuation wavenumber spectral shape; and the ratio of fluctuation levels in strongly and weakly driven conditions (see Figure 40). This strongly supports electron thermal transport being caused by electron-scale ETG turbulence at the outer-core of this moderate $\beta$ H-mode plasma, in conditions of both strong and weak ETG drive.[233]

## VIII. Holistic Microstability Analysis for Select Regimes

### A. Edge Pedestal

The transition between the shallow gradient core and the steep H-mode pedestal, triggers a sharp change in microstability in a relatively collisional MAST H-mode pedestal, with modest bootstrap current and $dn_e/dr$ dominating $dp/dr$.[198,234] In the steep pedestal KBMs dominate at $k_\perp \rho_i < 1$ (close to marginal), but MTMs (and ETG at higher $k_y$[231] dominate the shallower plateau inboard of the pedestal top. This stark mode transition is triggered by an increasing pedestal density gradient post-ELM (see Figure 41c) and contributes to the pedestal recovery.[198] Similar results are found in non-Li H-mode pedestals in NSTX[200,235] (see Figure 41b), with ETG also unstable from mid-pedestal outwards. The MTM-KBM mode transition is also seen at the pedestal top of a lower $\nu_*$ MAST H-mode pedestal, but enhanced bootstrap current gives KBMs access to second stability.[236] DBS and cross-polarization DBS in MAST have measured $\delta n$ and $\delta B$ fluctuations at the pedestal top during the ELM recovery in type-I ELMs. ETG dominate with MTM also unstable at the location and wavenumbers $3 < k_\perp \rho_i < 4$ measured by DBS/CP-DBS. The measured $(\delta B/B)/(\delta n/n) \sim 0.05$ is closer to the value 0.02 expected linearly from ETG than 0.4 for MTMs.

## B. Impact of Lithium

Li coatings applied to PFCs in NSTX reduce edge recycling, improve confinement[200] and substantially change profiles (see Figure 41a). The density pedestal is broader but shallower with Li, and inside $\Psi_{95}$, $dT_e/dr$ is steeper and $\chi_{e,eff}$ is lower. Radial profiles of the dominant microinstabilities at $k_\theta \rho_s < 1$ (illustrated in Figure 41b) are quite different. Without Li MTMs dominate at a conventional pedestal top, but with Li MTMs are stabilized by higher $dn_e/dr$ and are replaced by hybrid TEM-KBM modes with lower growth rates comparable to $\gamma_E$. MTM growth rates at the pedestal top are insensitive to large reductions in $\nu_e$, as seen in MAST.[199] Outside $\Psi_{95}$ both cases are unstable to ETG modes, but lower $R/L_n$ with Li results in more virulent ETG that may limit $dT_e$/dr. In both plasmas the pedestal is close to the KBM stability boundary but in second-stability where growth rates decrease with increasing pressure gradient.

## C. Pellet Fueling

Local microstability was analysed in edge pellet fuelled MAST H-modes, on three surfaces close to the pellet ablation peak during 10 $ms$ following pellet launch.[163] Microstability was strongly impacted by large local equilibrium excursions induced by the pellet. The most striking feature is an asymmetry between the stabilizing and destabilizing impacts of the pellet on TEMs, inside and outside the ablation peak, which arises because of favorable and unfavorable drifts at these locations, and could result in more pellet particles being transported outwards than into the core. While drifts favor stability for TEM at $\theta$=0 (outboard side) on the $dn/dr > 0$ surface, drifts are unfavorable at $\theta = \pi$: without collisions CTEM would be unstable at $\theta = \pi$, but are stabilized by the level of collisions in this MAST plasma.

## D. Enhanced Electron Heat Transport/Anomalous Fast Ion Redistribution at High Power

At high $P_{nbi}$ NSTX H-modes have flat core $T_e$, which is correlated large amplitude GAEs and CAEs, see Figure 42a. If the $P_{nbi}$ source is classically transferred to the plasma, the core electron heat transport is very hard to explain because gradients of the thermal species are too low to drive microturbulence.[105] One possibility is that core $Q_e$ is enhanced by stochastic electron orbits generated by multiple overlapping GAEs.[105,237] Alternatively CAEs and GAEs couple to kinetic Alfven waves (KAWs) and convey the NBI energy and momentum sources to a resonance at larger radius where they are transferred to the thermal plasma, in a process called "energy channelling"[238] (see Figure 42b,c) . Nonlinear hybrid MHD-particle simulations find that "energy channelling" involving CAEs coupling to KAWs, appears the more plausible explanation.[239] Novel reflectometry of GAEs and CAEs in similar discharges, however, find amplitudes that are too low to support either mechanism, and also rule out significant stochastic ion heating from CAEs.[240] Higher $B$ and more flexible NBI configurations on NSTX-U impact on fast particle modes and should help address this question. GAEs on NSTX-U arise at higher frequency and toroidal mode number than on NSTX, and are suppressed by higher pitch beam ions injected by off-axis NBI,[241] consistent with theory and hybrid MHD-particle simulations.[242]

## E. Long Steady Discharges

Long steady discharges that will be delivered by NSTX-U and MAST-U are ideal for confinement studies. Initial transport studies on NSTX-U for a long pulse L-mode with $P_{nb} = 2.6\ MW$, $\langle n_e \rangle = 4.3 \times 10^{19}\ m^{-3}$ and $\beta_t$=4.1% shows that $\chi_e \gg \chi_i$ and $\chi_i \sim \chi_{i,NC}$ at $0.2 < r/a < 0.8$,[160] which is consistent with local GYRO calculations in $0.45 < r/a < 0.7$, where ITG turbulence is either stable or weakly growing with $\gamma_{ITG} \ll \gamma_E$. At $r/a = 0.47$, $\beta$ and $Z_{\rm eff}$ may be sufficiently large for significant electron heat transport contribution from $Q_{e,MTM}$, where $\gamma_{MTM} > \gamma_E$. Electron-scale nonlinear ETG calculations predict large contributions from $Q_{e,ETG}$ at $r/a = 0.47, 0.56, 0.66$. Further out at $r/a$=0.76, however, ETG is diminished and ITG rises to dominate transport because $\gamma_E$ is lower and falling with radius. This is consistent with BES finding broadband ion-scale fluctuations growing with radius. Interestingly BES finds bi-modal poloidal phase velocities at $r/a \sim 0.68$ that could indicate the presence of two types of mode at ion scales, but these were not found in nonlinear gyrokinetic simulations at this radius. These NSTX-U plasmas have complicated microturbulence at both electron and ion scales that exhibit strong radial dependence. More sophisticated calculations including non-local profile variation $\delta B$, and multi-scale interactions may be needed.[160]

## IX. Conclusions

In this review we have presented results, which show that many fundamental energy transport and confinement properties of Spherical Tokamaks are different from those at higher aspect ratio. These differences are based on geometric considerations, with ST plasmas having more extreme toroidicity than plasmas at higher aspect ratio and the relatively larger $E \times B$ shearing rates, both of which serve to suppress electrostatic drift wave instabilities at both ion and electron gyroradius scales, and also through the importance of much stronger electromagnetic effects due to the ST operating at high $\beta_T$. These latter effects bring into light the importance of both microtearing modes and Kinetic Ballooning modes (modified by the fast electron pressure), both becoming important in the core of ST plasmas, while being important only in the pedestal region at higher aspect ratio. These differences have led to inferring a very strong improvement in normalized confinement with decreasing collisionality, $\Omega\tau_E \propto \nu_{e,*}{}^{-1}$, much stronger than at higher aspect ratio, which bodes well for an ST-based fusion pilot plant should this trend continue.

For the present generation of STs, electrons are highly anomalous and they are the dominant channel through which energy is lost. Ion transport outside the very core of the plasma, and especially in H-modes, is near neoclassical values (reflecting the suppression of the low-$k$ electrostatic drift wave instabilities), although neoclassical ion thermal diffusivities can be in the $\geq 1$ $m^2/s$ range. There is some inferred evidence that ion transport becomes more anomalous a the lowest ST collisionalities attained to date. Studies of particle and momentum transport have been more limited, but the latter may indeed capture the effect of any subdominant low-$k$ drift wave turbulence. Internal Transport Barriers have been observed in both MAST and NSTX, and, as at higher aspect ratio, their existence is tied to local values of $q$ and magnetic shear.

Gyrokinetic studies, coupled with low- and high-$k$ turbulence measuements, have shed light on the underlying physics controlling transport. At lower $\beta$, both ion- and electron-scale electrostatic drift turbulence may be responsible for transport, while at higher $\beta$, MTMs, KBMs, and hybrid TEM-KBMs play a role. All of these modes are sensitive to $\hat{s}$, $q$ and $R/L_n$. Flow shear will, of course affect the balance between ion- and electron-scale modes. Considerable work has been devoted to understanding electron heat transport from MTMs, which are complex modes with instability thresholds in $R/L_{Te}$ and $\beta$, and growth rate sensitivity (some non-monotonic) to collisions, magnetic shear, $R/L_n$, $R/L_{Te}$, and $\beta$.

Non-linear gyrokinetic simulations have shown that the electron heat flux decreases with decreasing collisionality, consistent with the global normalized confinement scaling, although flow shear was neglected in these calculations. High-$\beta$ plasmas with with large $\alpha_{MHD}$ found significant transport in all channels from hybrid TEM-KBM turbulence, which dwarfs that from subdominant MTMs in this specific regime. Non-linear ETG simulations predict significant heat fluxes in some high- and low-$\beta$ H-modes. Initial multi-scale non-linear simulations[243] found that ETG turbulence could suppress MTMs.

A wealth of fluctuation data from BES, DBS, and high-$k$ scattering on NSTX and MAST has facilitated detailed comparisons with gyrokinetic simulations and the study of fluctuations at ion and electron scales in MAST and NSTX. These data have provided compelling evidence for the presence of ITG and ETG turbulence in some plasmas, and direct experimental support for the impact of experimental actuators like $\gamma_E$, $R/L_n$ and magnetic shear on turbulence and transport.

The next generation of ST experiments will test the favorable confinement trends at even lower collisionality, along with other aspects of ST performance that can inform the basis for an ST power plant. For instance, NSTX-U with up to 18 MW of auxiliary heating power (see Table 1), $B_T$ up to 1 $T$ and $I_p$ up to 2 $MA$ will be able to explore a collisionality regime up to five times lower than that in NSTX, thus testing the confinement and transport processes of both the thermal plasma and energetic particles in this regime. NSTX-Upgrade, with its ability to achieve very high $\beta_N/l_i$ will also explore the high-$\beta$ route to non-inductive, long-pulse operation. Further, while NSTX-U will explore heat flux mitigation in conventional divertor configurations, future upgrades to NSTX-U could involve the implementation of liquid lithium divertors. MAST-Upgrade operation in a similar parameter range will also explore the confinement and transport at lower collisionalities than at which MAST operated, its main focus will reflect its flexibility to test a wide range of divertor configurations, the most notable of which will be on long-legged (i.e., Super-X) divertor operation as a heat flux mitigation method. The ST40 ST will be operating at higher toroidal field (3 $T$) than either NSTX-Upgrade or MAST-Upgrade to develop the physics basis for STF1, which will use high temperature superconducting magnets to produce fusion powers with $Q \geq 2$.

These new experiments will open up avenues for continued and extended physics studies of ST confinement and transport. The expanded operating ranges of these STs will provide the basis for further validation of theoretical predictions, including gyrokinetic simulations with synthetic diagnostics, against experimental measurements of turbulence and kinetic profiles to complement the empirical experimental approach. Advances in computer science will aid in enhancing the gyrokinetic codes in areas critical to understanding ST transport, such as the interaction of electron and ion scale turbulence, self-consistent treatments of flow shear, the importance of thermal plasma transport caused by energetic particle-driven modes, and the ability to provide global descriptions including phenomena like avalanching and turbulence spreading. These studies will provide the basis for developing reduced predictive models of ST plasma transport and the potential to integrate these reduced models with those at higher aspect ratio to provide predictions beyond narrow aspect ratio ranges.

In particular, the impact of fast particles on thermal confinement in the plasma core remains an open question. This question has direct relation to how the thermal plasma is influenced by $\alpha$-particles in a burning plasma at both low and high aspect raito. Data from NSTX-U and MAST-U will help to resolve the dilemma as to whether (and if so, how) electron heat confinement is degraded in strongly heated high $\beta$ ST plasmas with fast particle driven GAE and CAEs.

The new experiments will also provide the opportunity to study other transport channels, particularly impurity transport as related to the dilution by helium ash and radiation losses, but also the effect of energetic particle-driven modes on the energetic particle distribution, which can affect both non-inductive current drive and fusion power production. Further, the new experiments can drive progress on optimizing core-pedestal coupled high performance scenarios through understanding further the nature of the H-mode pedestal and ITB formation. These can be accomplished through both the flexibility of the devices as well as diagnostics and theory specifically targeting these phenomena.

These results, along with those from other STs to explore non-inductive startup methods, as discussed in the Introduction, will be critical for assessing the feasibility of an ST-based fusion pilot plant.

## X. Acknowledgements

The authors gratefully acknowledge discussions with and input from Anthony Field, Gleb Kurskiev and Martin Valovic. S. Kaye's work has been supported by U.S. Dept of Energy contracts DE-AC02-09CH11466. C M Roach contributions to this paper were funded by EPSRC Grant EP/T012250/1.

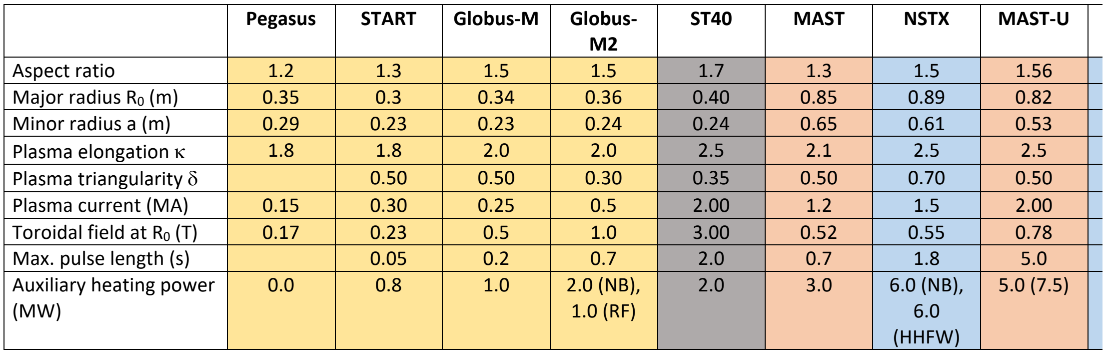

| | Pegasus | START | Globus-M | Globus-M2 | ST40 | MAST | NSTX | MAST-U |
|---|---|---|---|---|---|---|---|---|
| Aspect ratio | 1.2 | 1.3 | 1.5 | 1.5 | 1.7 | 1.3 | 1.5 | 1.56 |
| Major radius $R_0$ (m) | 0.35 | 0.3 | 0.34 | 0.36 | 0.40 | 0.85 | 0.89 | 0.82 |
| Minor radius a (m) | 0.29 | 0.23 | 0.23 | 0.24 | 0.24 | 0.65 | 0.61 | 0.53 |
| Plasma elongation $\kappa$ | 1.8 | 1.8 | 2.0 | 2.0 | 2.5 | 2.1 | 2.5 | 2.5 |
| Plasma triangularity $\delta$ | | 0.50 | 0.50 | 0.30 | 0.35 | 0.50 | 0.70 | 0.50 |
| Plasma current (MA) | 0.15 | 0.30 | 0.25 | 0.5 | 2.00 | 1.2 | 1.5 | 2.00 |
| Toroidal field at $R_0$ (T) | 0.17 | 0.23 | 0.5 | 1.0 | 3.00 | 0.52 | 0.55 | 0.78 |
| Max. pulse length (s) | | 0.05 | 0.2 | 0.7 | 2.0 | 0.7 | 1.8 | 5.0 |
| Auxiliary heating power (MW) | 0.0 | 0.8 | 1.0 | 2.0 (NB),<br>1.0 (RF) | 2.0 | 3.0 | 6.0 (NB),<br>6.0 (HHFW) | 5.0 (7.5) |

Table 1: Comparison of key operating parameters for STs that have performed, or will be performing, confinement studies. Heating power is through neutral beams, unless otherwise indicated. Values in parenthesis represent potential upgrades. HHFW stands for High Harmonic Fast Wave (RF) heating for NSTX and NSTX-U.

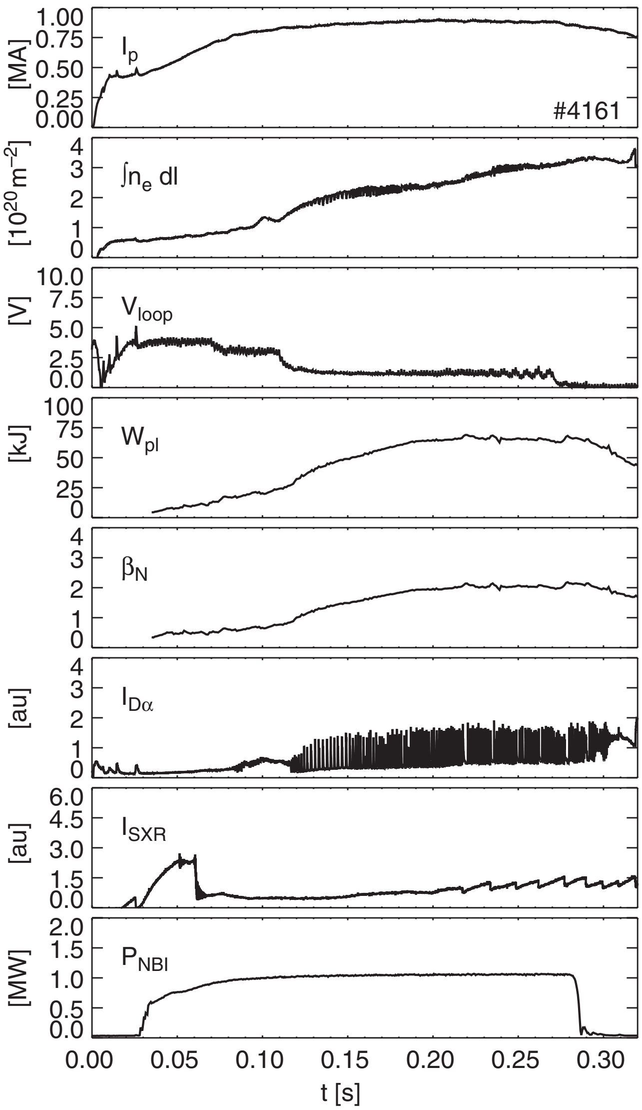

Figure 1: Temporal evolution of (from top panel down) plasma current, line-integral density, loop voltage, plasma energy, normalized $\beta_N$, $D_\alpha$, central SXR emission and NBI beam power for a ELMY H-mode discharge from MAST. Taken from Field et al.[56]

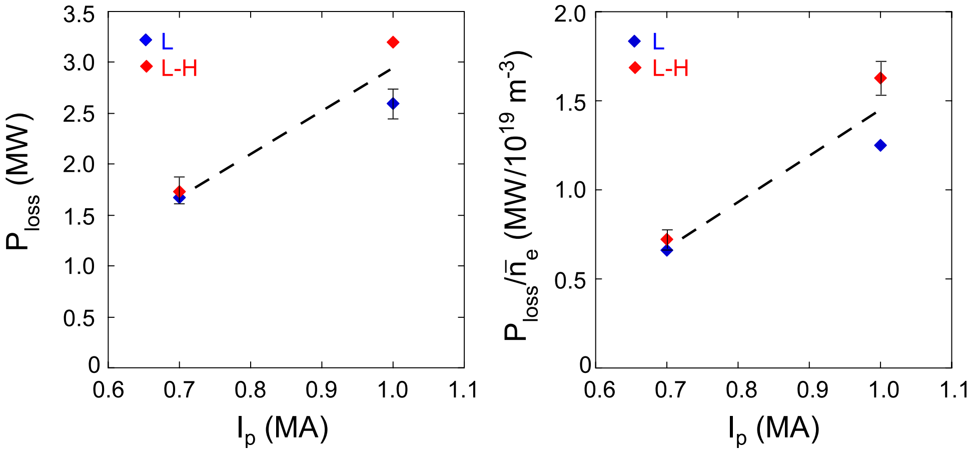

Figure 2: Loss power (left panel) and loss power normalized by line-averaged density (right panel) as a function of plasma current. Red symbols denote discharges that transition into the H-mode at that loss power, while blue symbols indicate discharges that remained in the L-mode for that loss power. Taken from Kaye et al.[67]

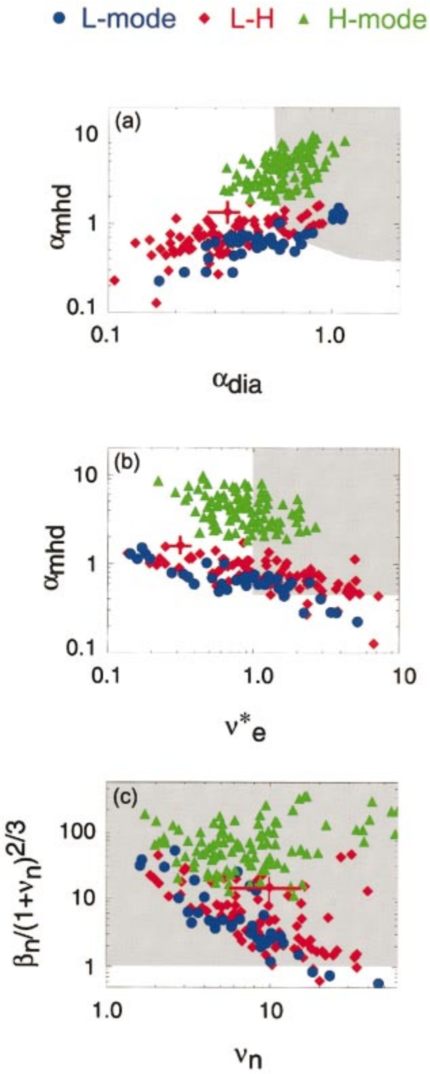

Figure 3: Comparison between experimental data and theory for (a) drift-resistive ballooning modes, (b) peeling modes, and (c) drift Alfvén modes. The shaded region in each plot indicates the theoretical prediction of H-mode access. Reproduced from Kaye et al., Phys. Plasmas, 10, 3953, 2003 with the permission of AIP Publishing.

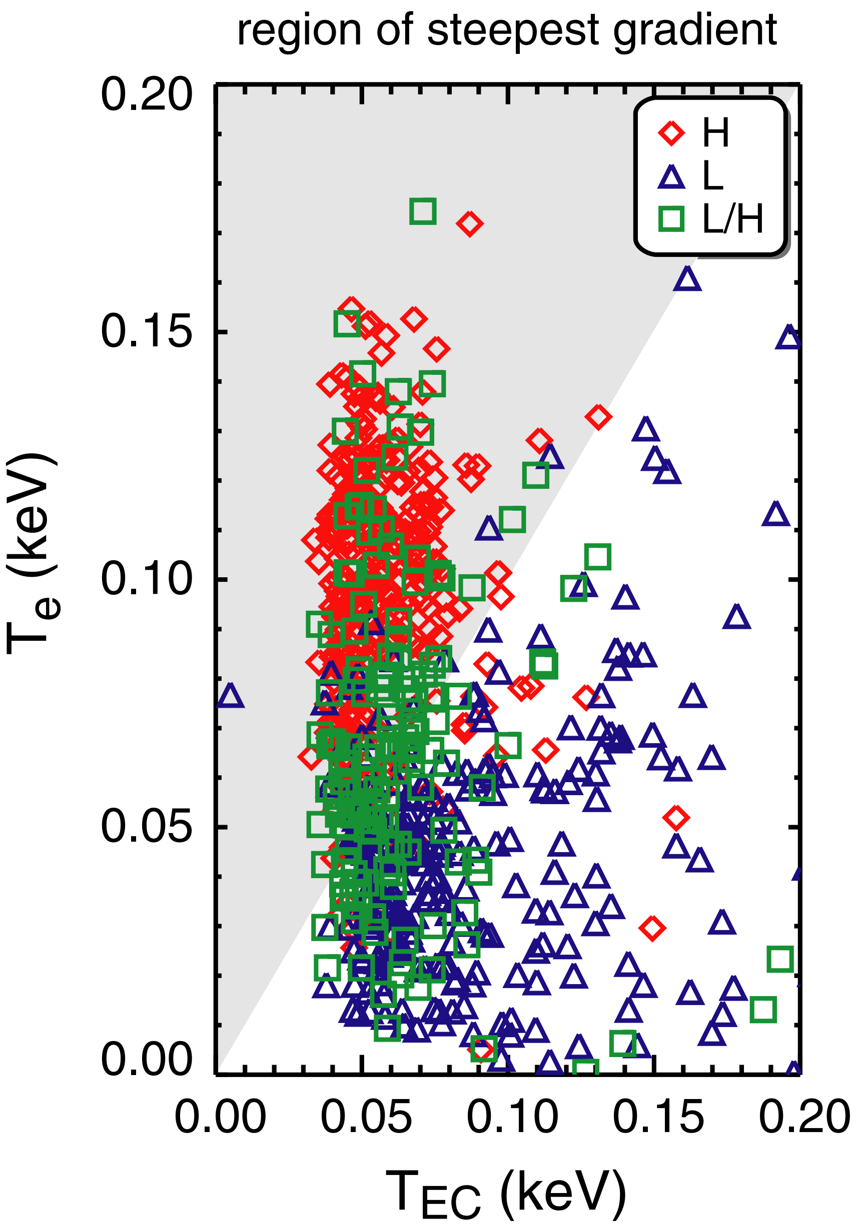

Figure 4: Comparison between experimental data from MAST and the finite-$\beta$ drive wave theory. The shaded regions indicate where the theory predicts an H-mode. Taken from Counsell et al.[72]

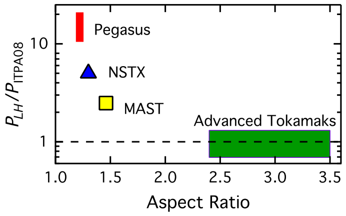

Figure 5: Measured $P_{LH}$ compared to the ITPA scaling for several STs at different aspect ratios. Reprinted Fig. 4 with permission from: Thome et al., Phys. Rev. Lett., 116, 175004, 2016. Copyright 2016 by the American Physical Society.

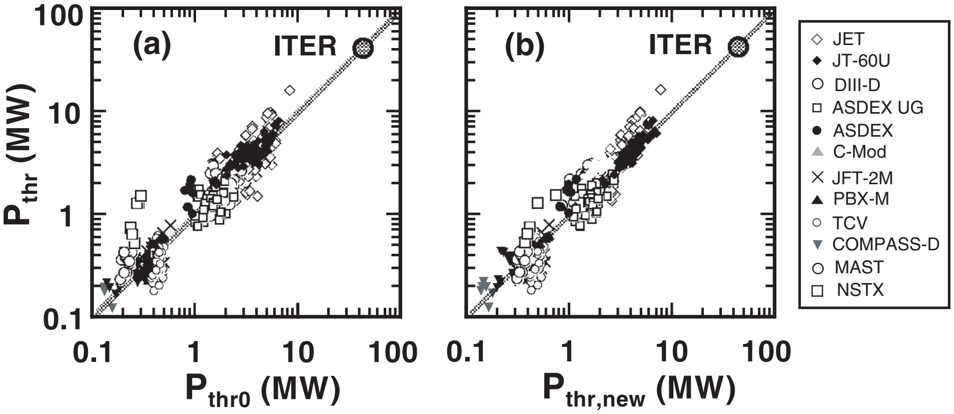

Figure 6: Comparisons of experimental power thresholds ($P_{thr}$) with scaling expressions from (a) Ryter et al.[81] and (b) Takizuka et al.[69] expressions. Taken from Takizuka et al.[69]

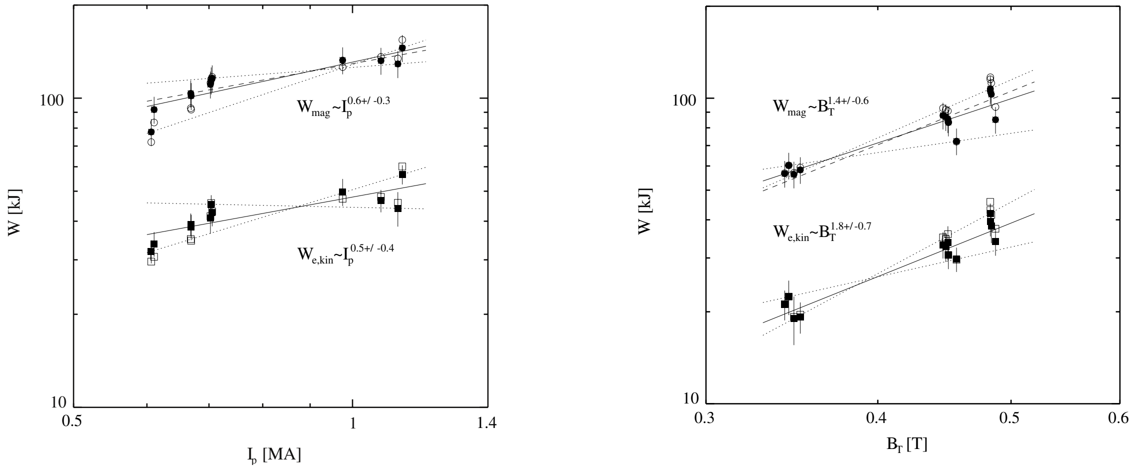

Figure 7: (left) Total and electron stored energy vs $I_p$ and (right) vs $B_T$ for MAST ELMy and ELM-free H-mode MAST plasmas. The various lines show the confidence limits of the linear fits through the data. Taken from Valovic et al.[95]

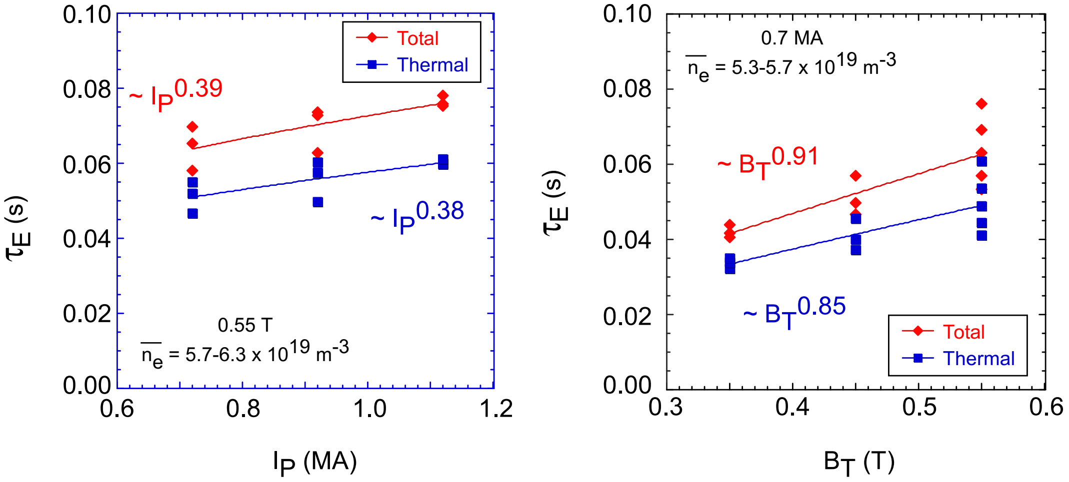

Figure 8: (left) Confinement time vs $I_p$ and (right) vs $B_T$ for NSTX H-mode plasmas with boronized walls. Taken from Kaye et al.[93]

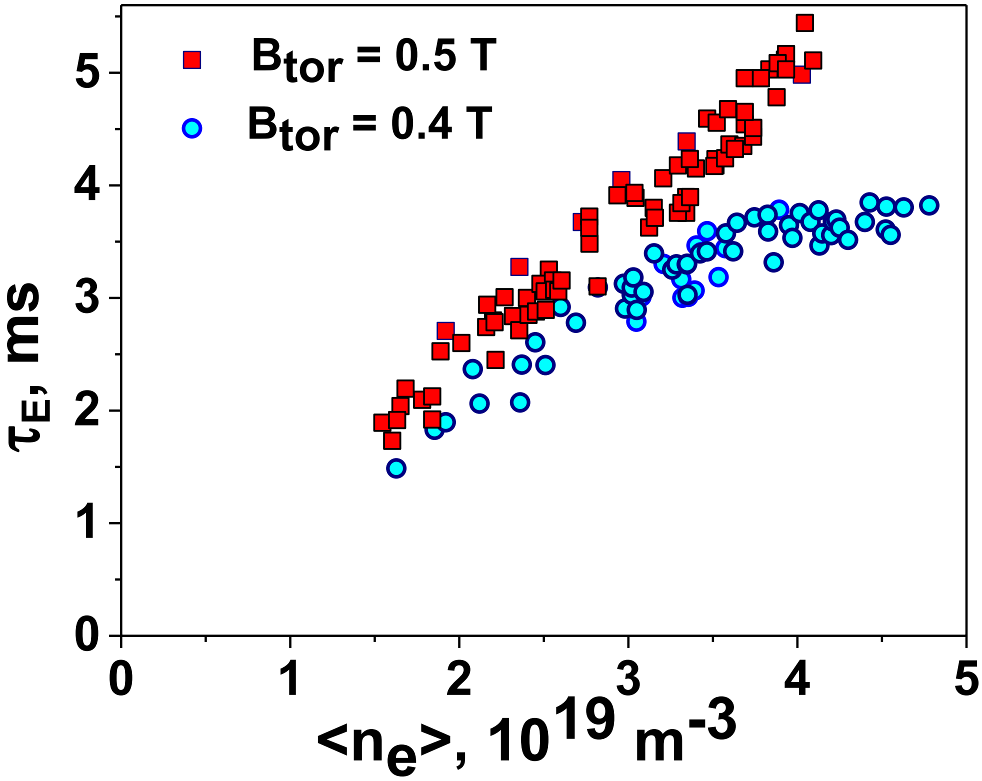

Figure 9: Comparison of the experimental confinement time values versus predicted values using the scaling given in Eq. 11 Taken from Bakharev et al.[98]

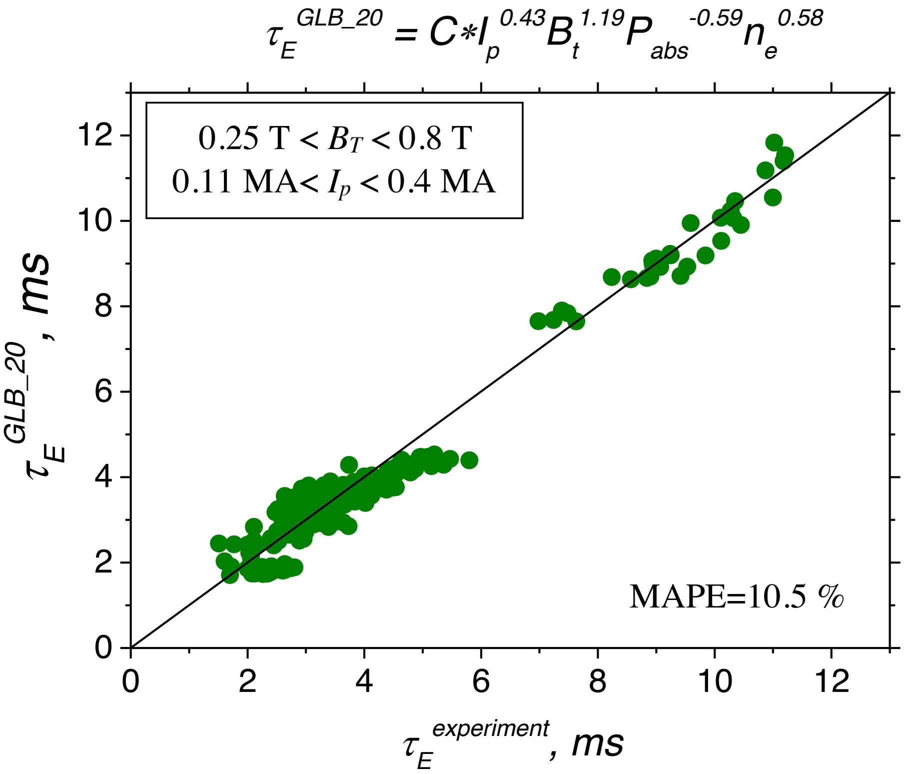

Figure 10: Experimentally deduced confinement time vs $I_p$ and $B_T$ parametric dependence for Globus-M (blue) and Globus-M2 (red) H-mode plasmas. Taken from Kurskiev et al.[99]

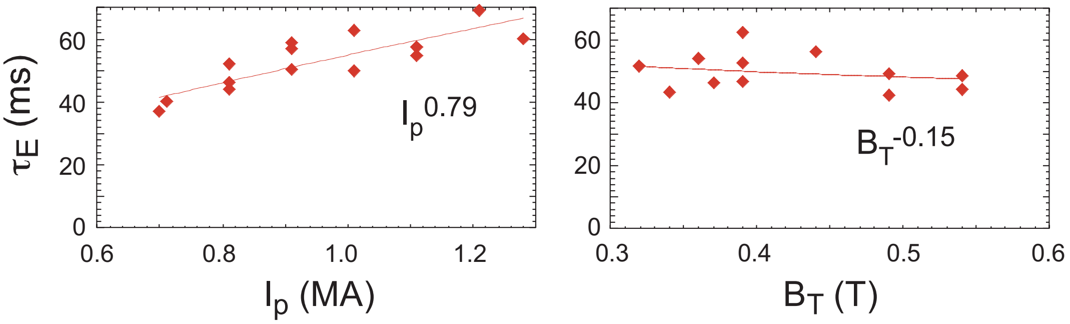

Figure 11: Thermal confinement times vs $I_p$ (left) and $B_T$ (right) for NSTX H-mode plasmas with lithium wall conditioning. Taken from Kaye et al.[101]

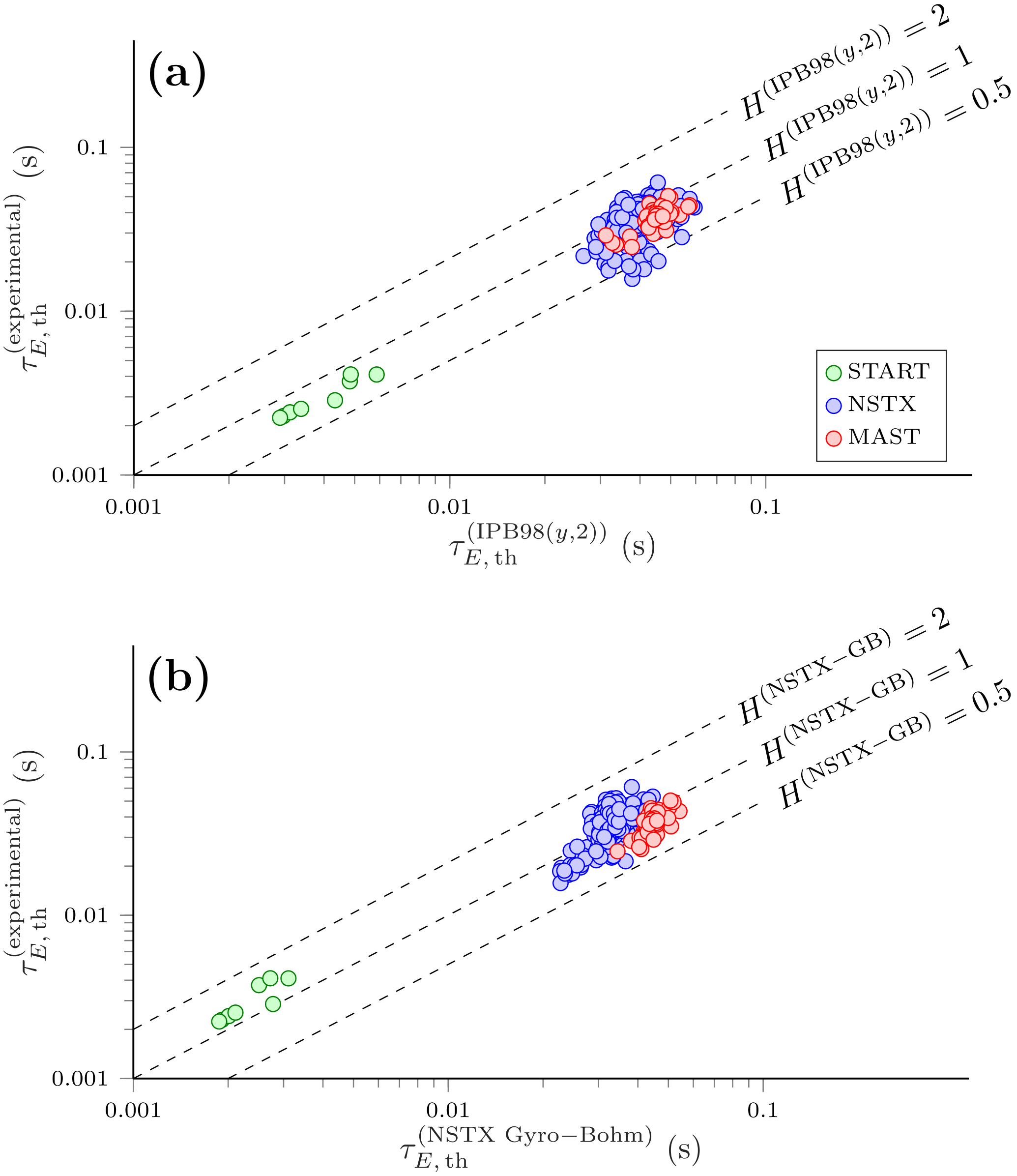

Figure 12: Comparison between a) the IPB98y,2 scaling and b) the NSTX gyroBohm scaling (Eq. 6) and experimental data from START, MAST and NSTX. Taken from Buxton et al.[102]

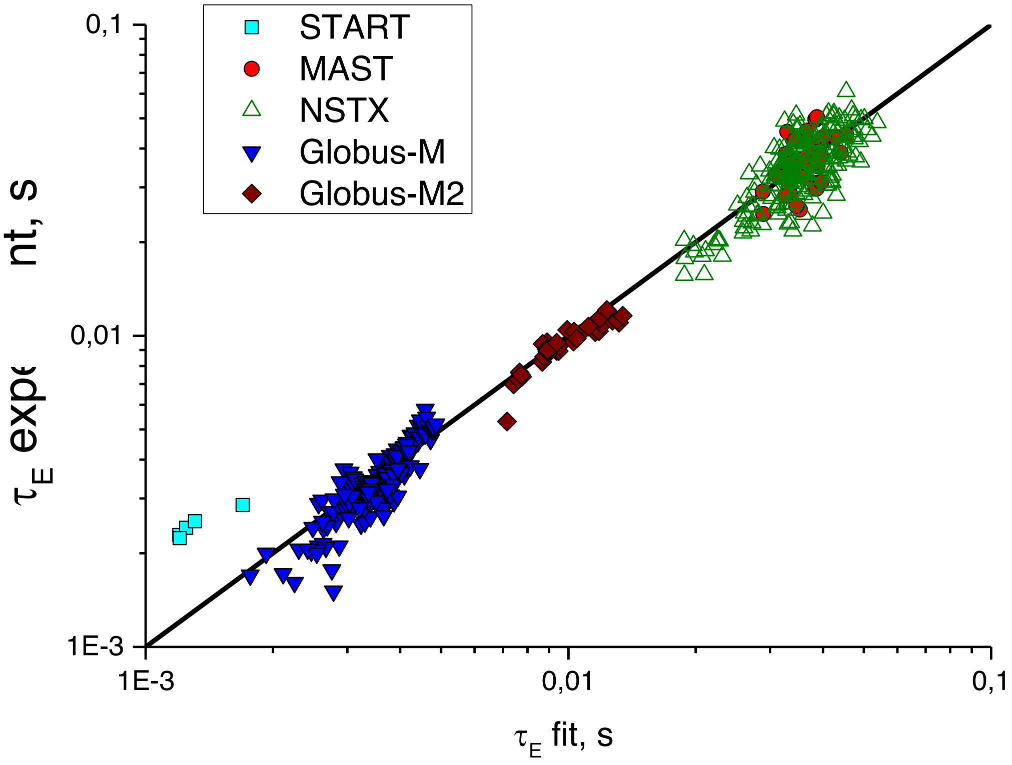

Figure 13: The results of the regression fit for the STs database. Taken from Kurskiev et al.[103]

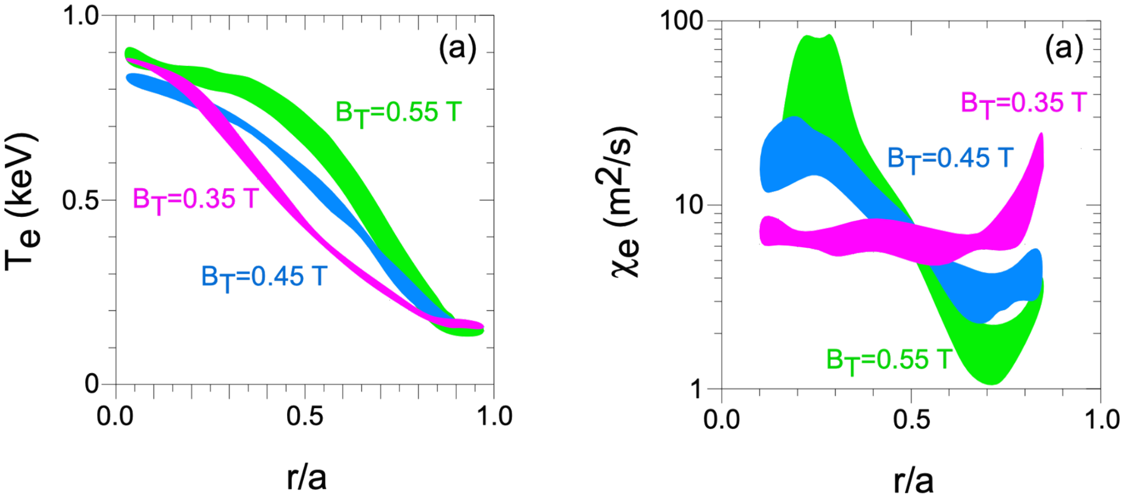

Figure 14: (left) Electron temperature and (right) electron thermal diffusivity as a function of $r/a$ at various $B_T$ in NSTX boronized wall H-mode plasmas. Taken from Kaye et al.[93]

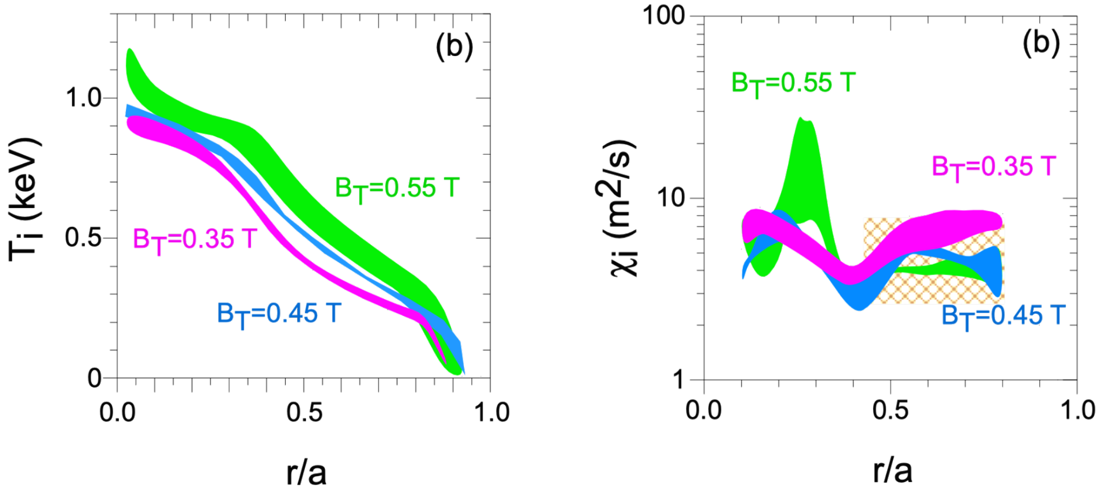

Figure 15: (left) Ion temperature and (right) ion thermal diffusivity as a function of $r/a$ at various $B_T$ in NSTX boronized wall H-mode plasmas. The yellow cross hatched region in the right-hand panel reflects the range of ion neoclassical thermal diffusivity over the range of $B_T$. Taken from Kaye et al.[93]

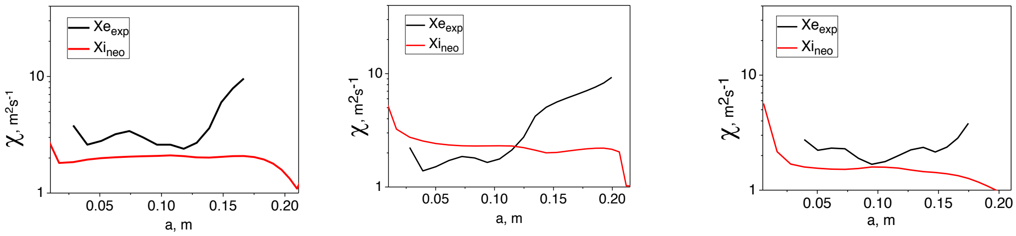

(a) $B_T = 0.4$ T $I_p = 200$ kA
#36954

(b) $B_T = 0.5$ T, $I_p = 200$ kA
#36610

(c) $B_T = 0.5$ T, $I_p = 250$ kA
#36618

Figure 16: Electron and ion neoclassical thermal diffusivity at different $B_T$ and $I_p$ in Globus-M. Taken from Telnova et al.[96]

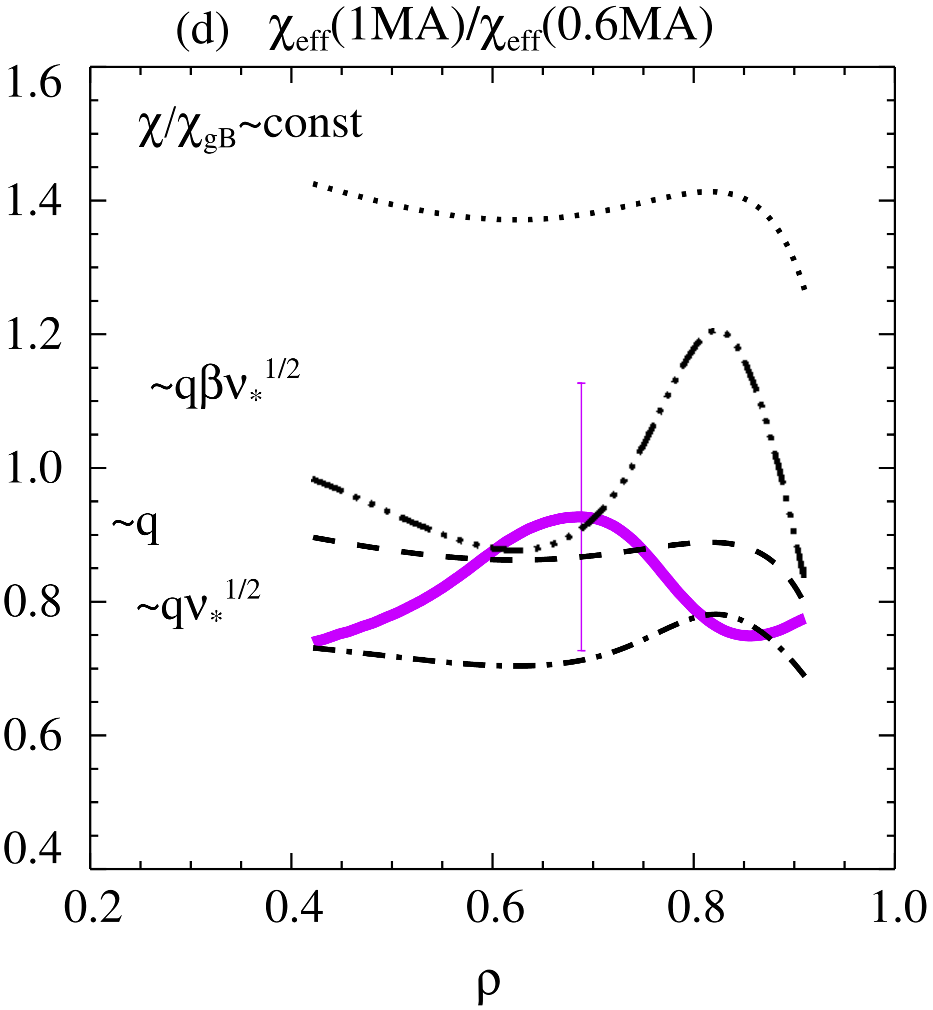

Figure 17: Pink line is the ratio of MAST experimental diffusivities, black lines are the ratios expected from different models calculated from $n_e$ and $T_e$ profiles and with $q \sim B_T/I_p$. Taken from Valovic et al.[95]

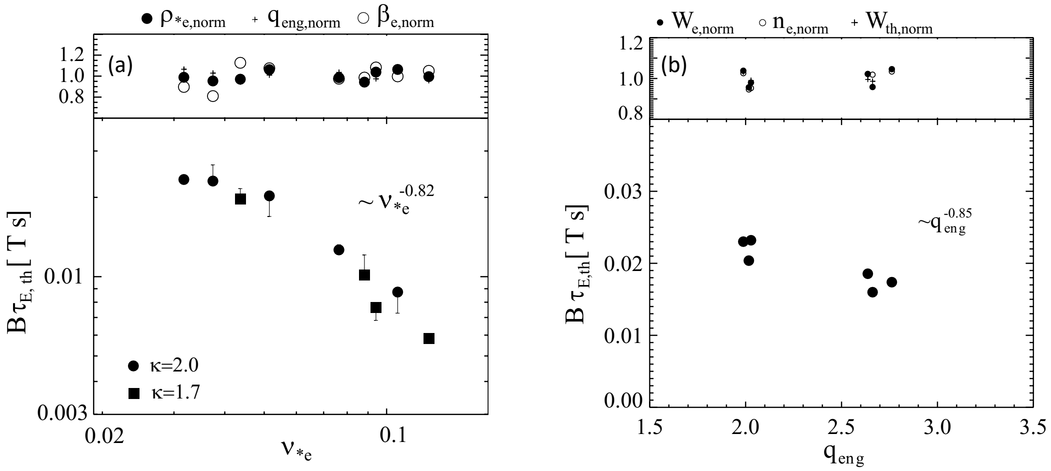

Figure 18: (a) Collisionality scan of thermal energy confinement time in MAST. Vertical bars show the size of the correction due to the variations in $\rho_{e,*}$, assuming gyroBohm scaling. Top panel shows variations of electron Larmor radius, $\beta$ and $q_{eng}$, all normalized to average values along the scan. The scaling is based on $\kappa$=2 data only. (b) Safety factor scan of thermal energy confinement time. Top panel show variations of electron energy content $W_e$, line-averaged density $n_e$, and thermal energy $W_{th}$, all normalized to average values along the scan. Taken from Valovic et al.[111]

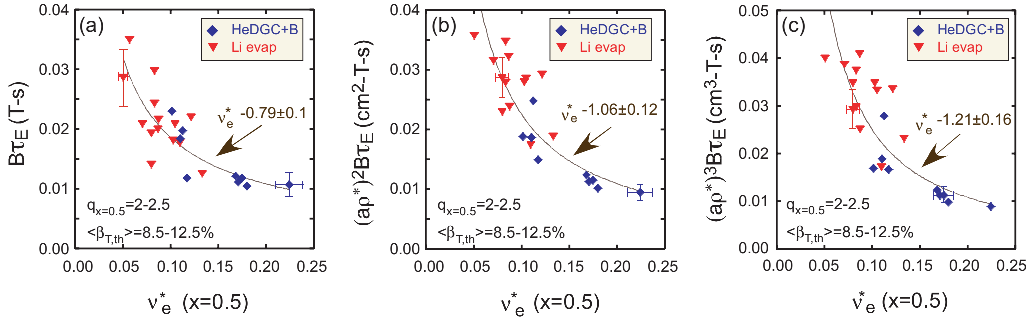

Figure 19: Normalized confinement time as a function of collisionality at $r/a = 0.5$ for NSTX H-mode discharges with boronized walls (blue points) and with walls conditioned through lithium evaporation (red points). Panels a through c assume no, Bohm and gyroBohm $\rho_*$ dependences respectively. Taken from Kaye et al.[101]

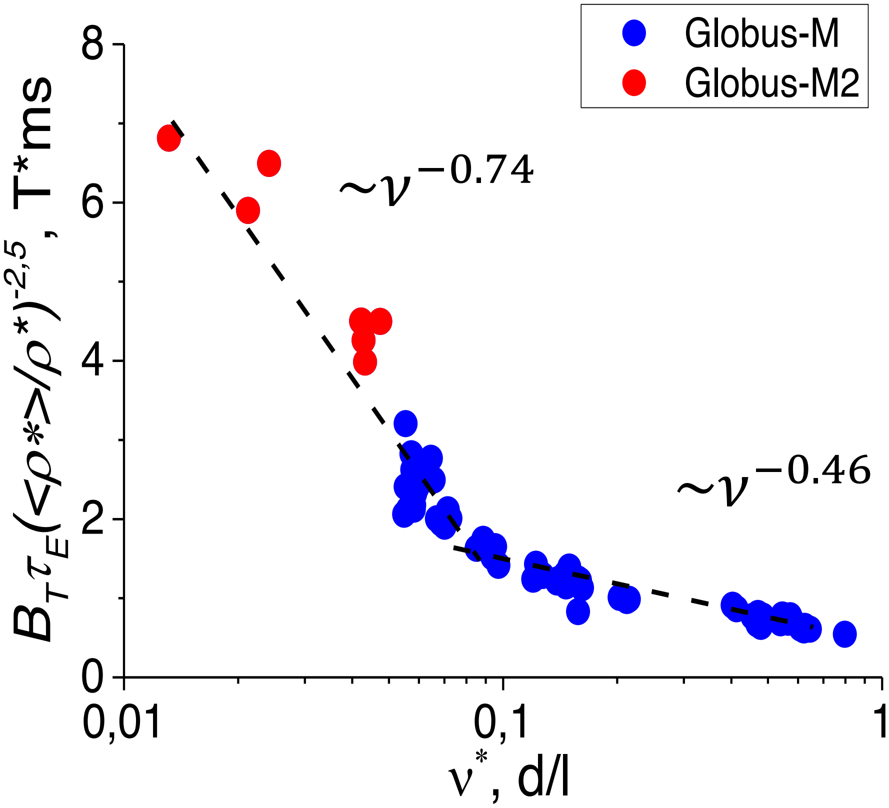

Figure 20: Normalized energy confinement corrected for $\rho_*$ variation versus collisionality. The was little variation of the dimensionless parameters $q_{eng}$, $\rho_*$ and $\beta$ across the range of collisionalities. Taken from Kurskiev et al.[103]

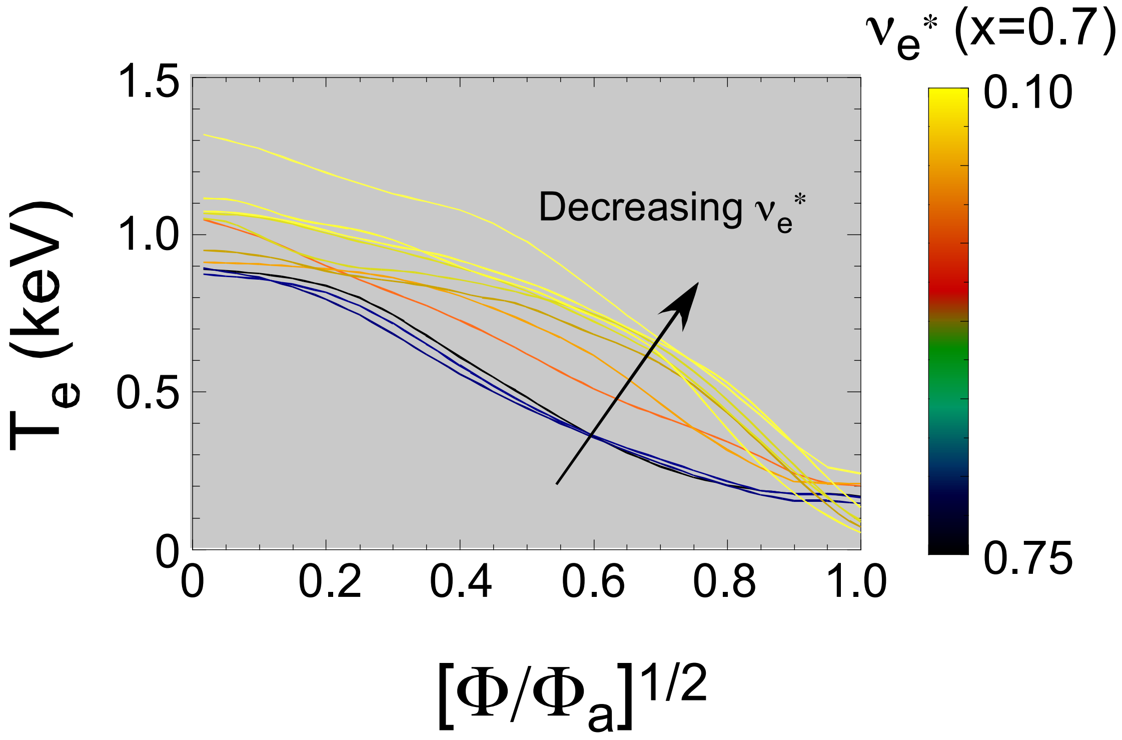

Figure 21: $T_e$ profiles from NSTX for lithium wall conditioned plasmas color-coded by normalized electron collisionality at $r/a \sim 0.7$. $\Phi$ is toroidal flux. Taken from Kaye et al.[101]

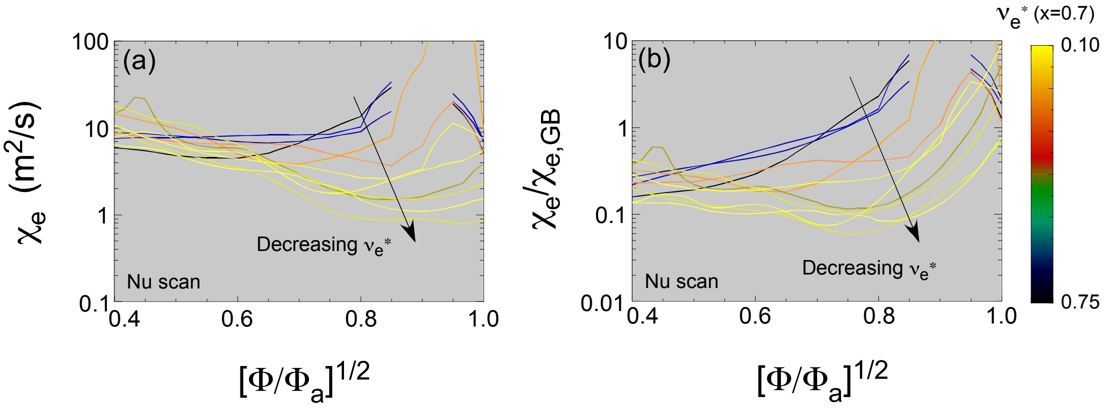

Figure 22: $\chi_e$ profiles color-coded by electron collisionality at $r/a$ ~0.7 for both boronized and lithium wall conditioned NSTX plasmas with minimal variation in $\beta$ and q ("Nu scan"). This is from the same dataset as that shown in Figure 21. $T_e$ profiles from NSTX for lithium wall conditioned plasmas color-coded by normalized electron collisionality at $r/a \sim 0.7$. (b) $\chi_e$ profiles normalized to $\chi_{gyroBohm}$ ($\propto \rho_s^2 c_s/a$). The profiles in both panels are color-coded by normalized electron collisionality at $r/a \sim 0.7$. Taken from Kaye et al.[101]

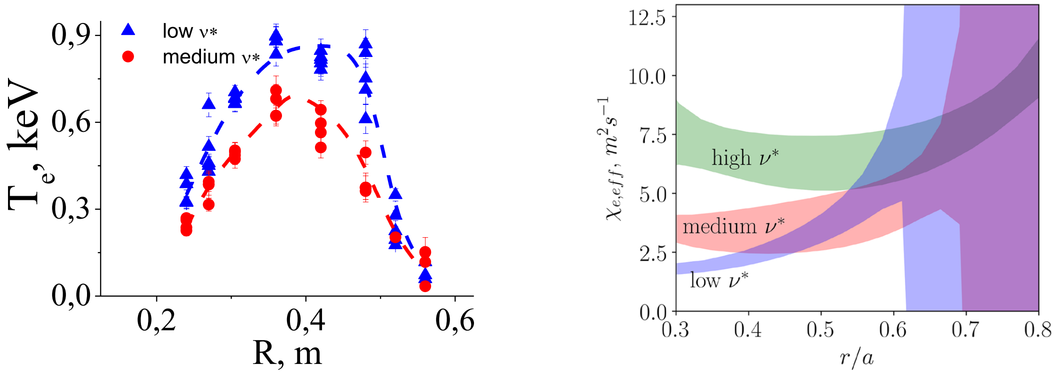

Figure 23: (a) Electron temperature profiles measured by Thomson Scattering for Globus-M plasmas at low ($\nu_* \sim 0.05$) and medium ($\nu_* \sim 0.1$) collisionalities. (b) Effective thermal diffusivity versus collisionality at fixed $\rho_*$, $\beta_T$, and $q$; high collisionality $\nu_* \simeq 0.4$, medium $\nu_* \simeq 0.1$, and low $\nu_* \simeq 0.05$. Taken from Kurskiev et al.[97]

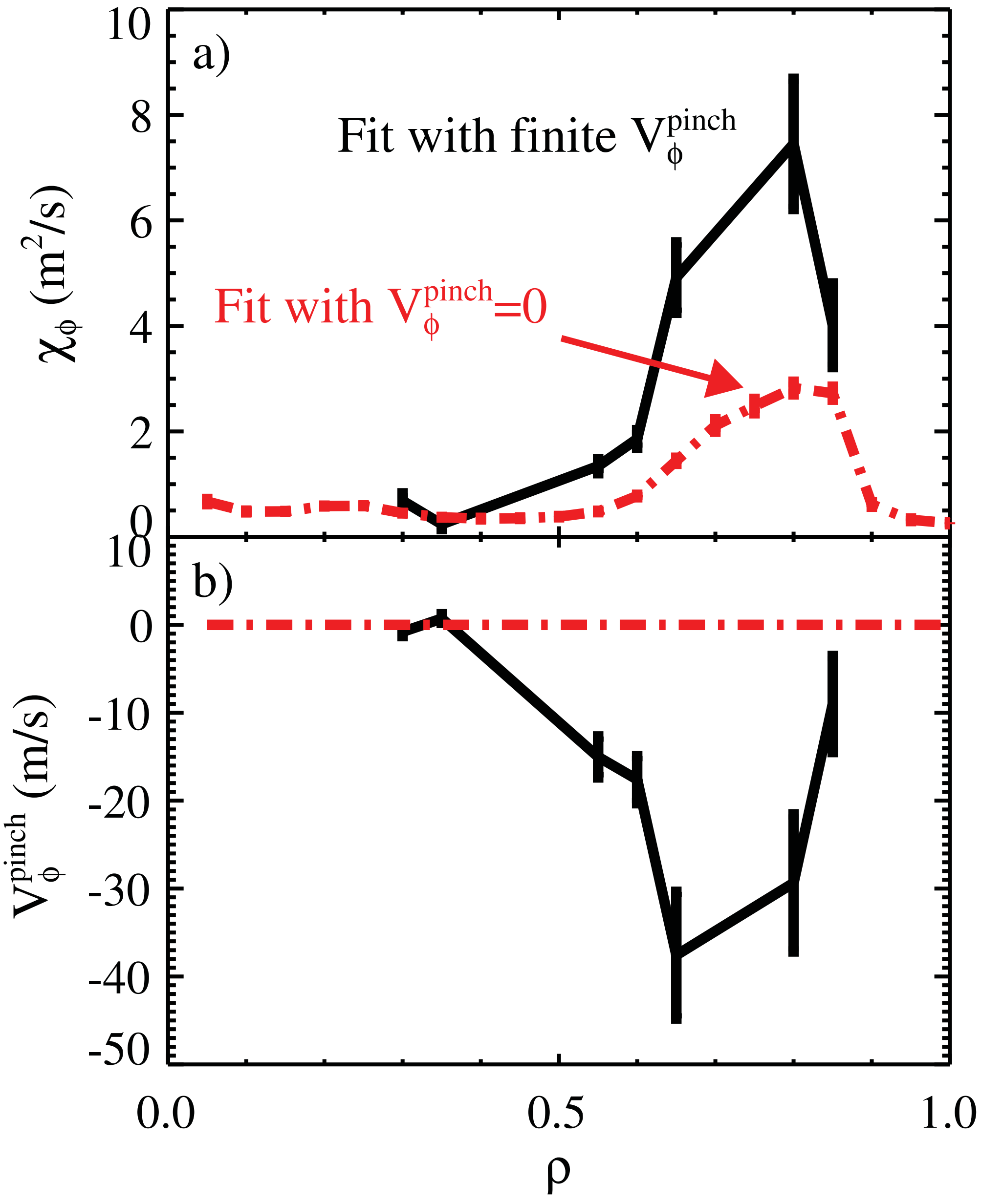

Figure 24: a) Momentum diffusivity and b) momentum pinch velocity inferred using $n = 3$ nonresonant magnetic perturbations to an NSTX H-mode plasma. For comparison, the inferred diffusivity neglecting any momentum pinch is also shown (dashed). Reprinted Fig. 2 with permission from: Solomon et al., Phys. Rev. Lett., 101, 065009, 2008. Copyright 2008 by the American Physical Society.

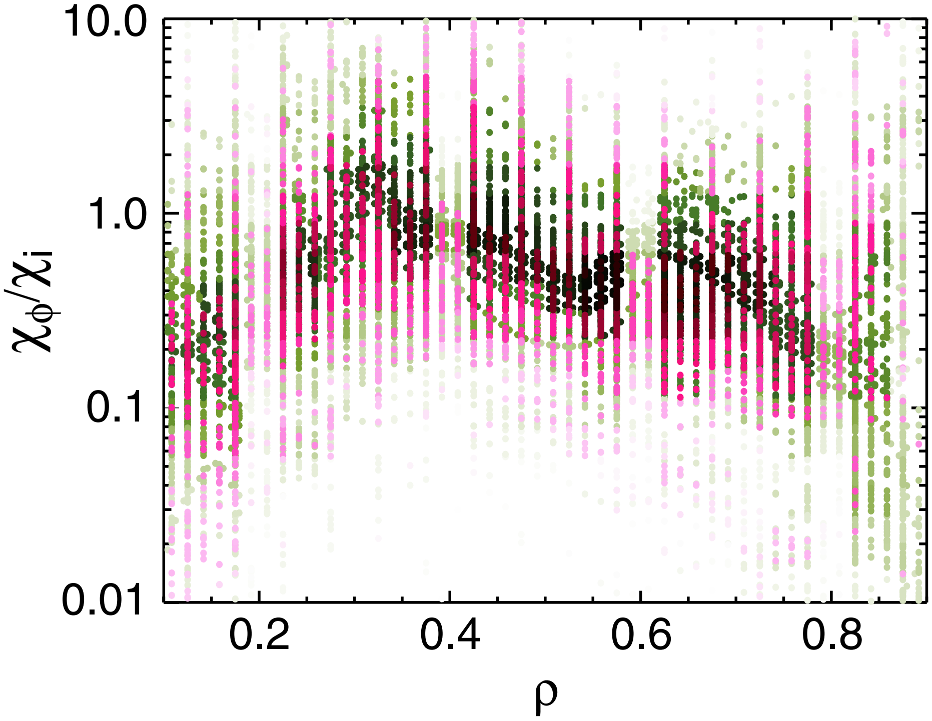

Figure 25: Profile of the Prandtl number calculated from TRANSP analysis of MAST L-mode (green) and H-mode (magenta) discharges. Taken from Meyer et al.[121]

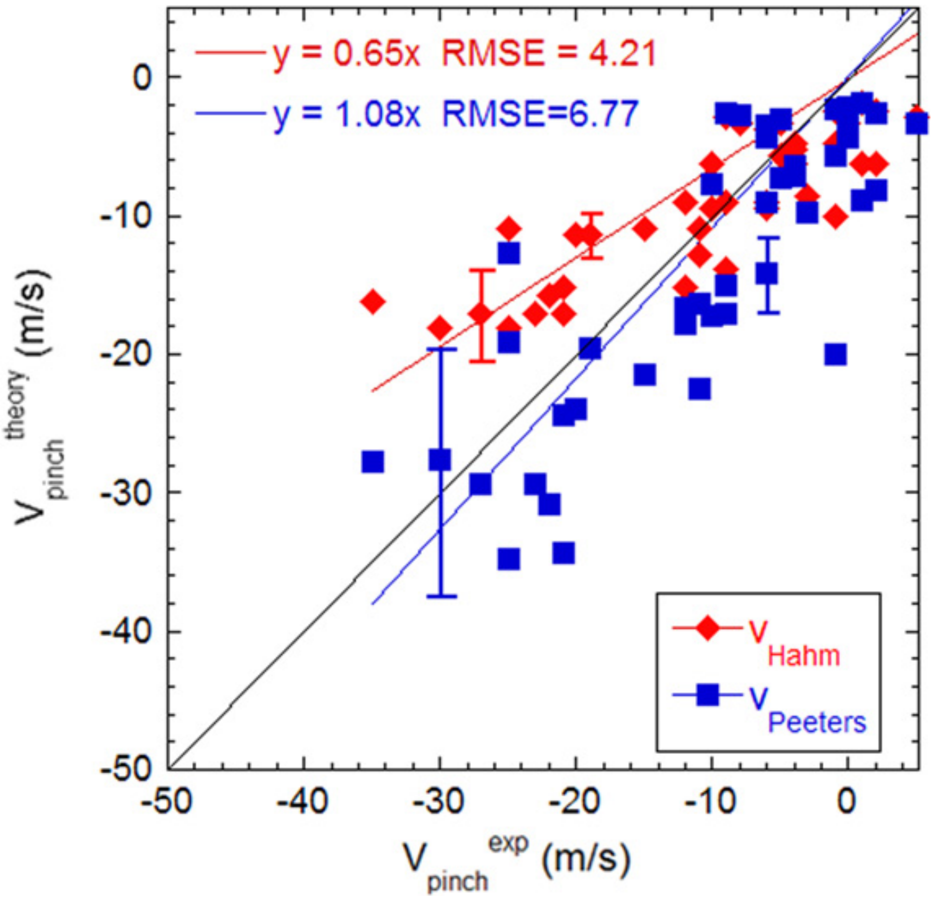

Figure 26: $v_{pinch}$ as computed by the Hahm (red) and Peeters (blue) theories versus experimentally inferred values for the outer region of NSTX H-mode plasmas. Taken from Kaye et al.[120]

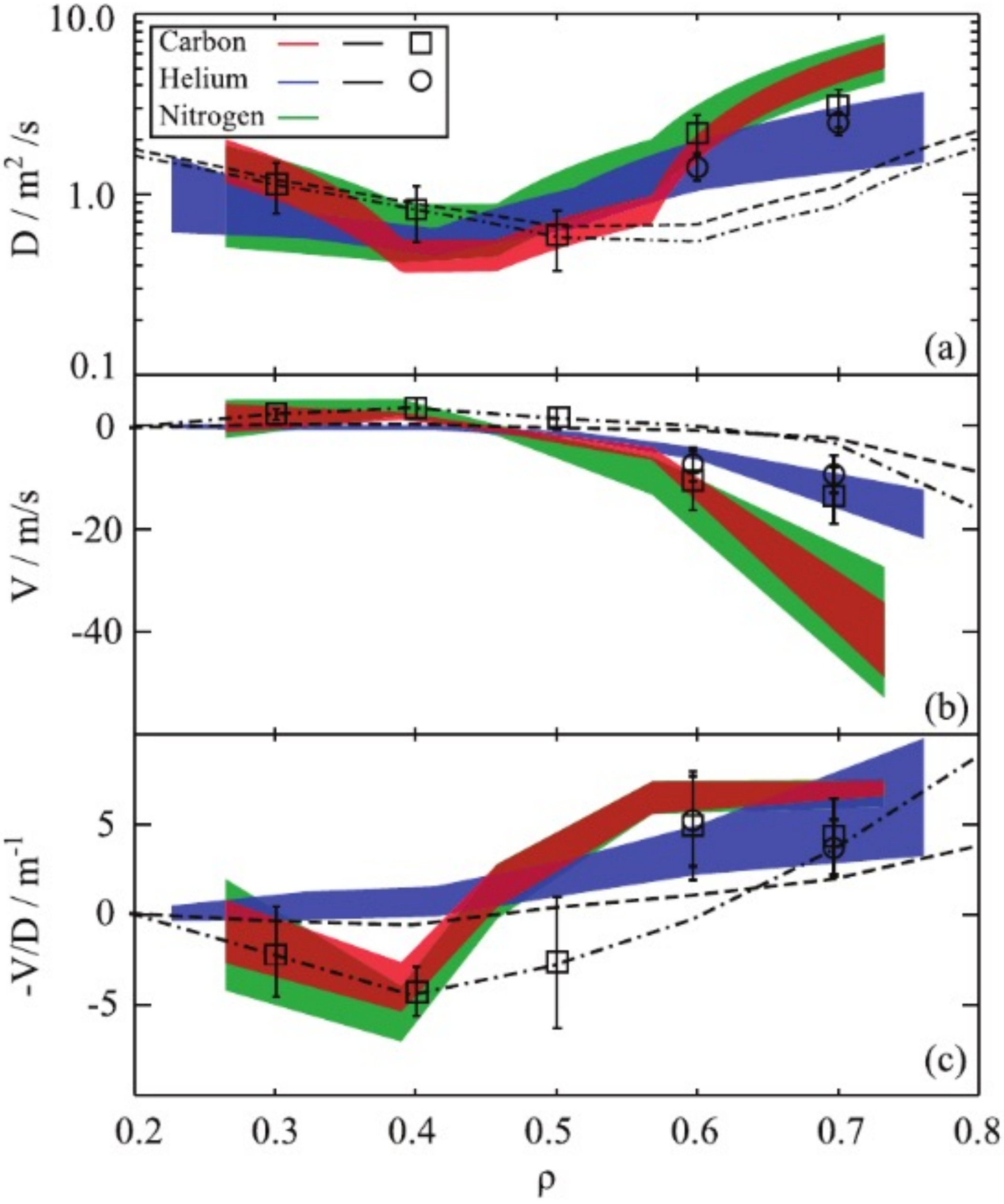

Figure 27: Radial profiles of transport coefficients for light impurities He, C, N measured in MAST, showing: (a) diffusivity, D; (b) convective velocity, V; and (c) the corresponding steady state impurity peaking factor, -V/D. NEO simulations of the neoclassical impurity transport coefficients for He and C are shown as dashed and dash-dotted lines. The quasi-linear and neoclassical transport coefficients for He and C have been summed at $r/a$=0.6 and $r/a$=0.7, and they are indicated by symbols. Taken from Henderson et al.[131]

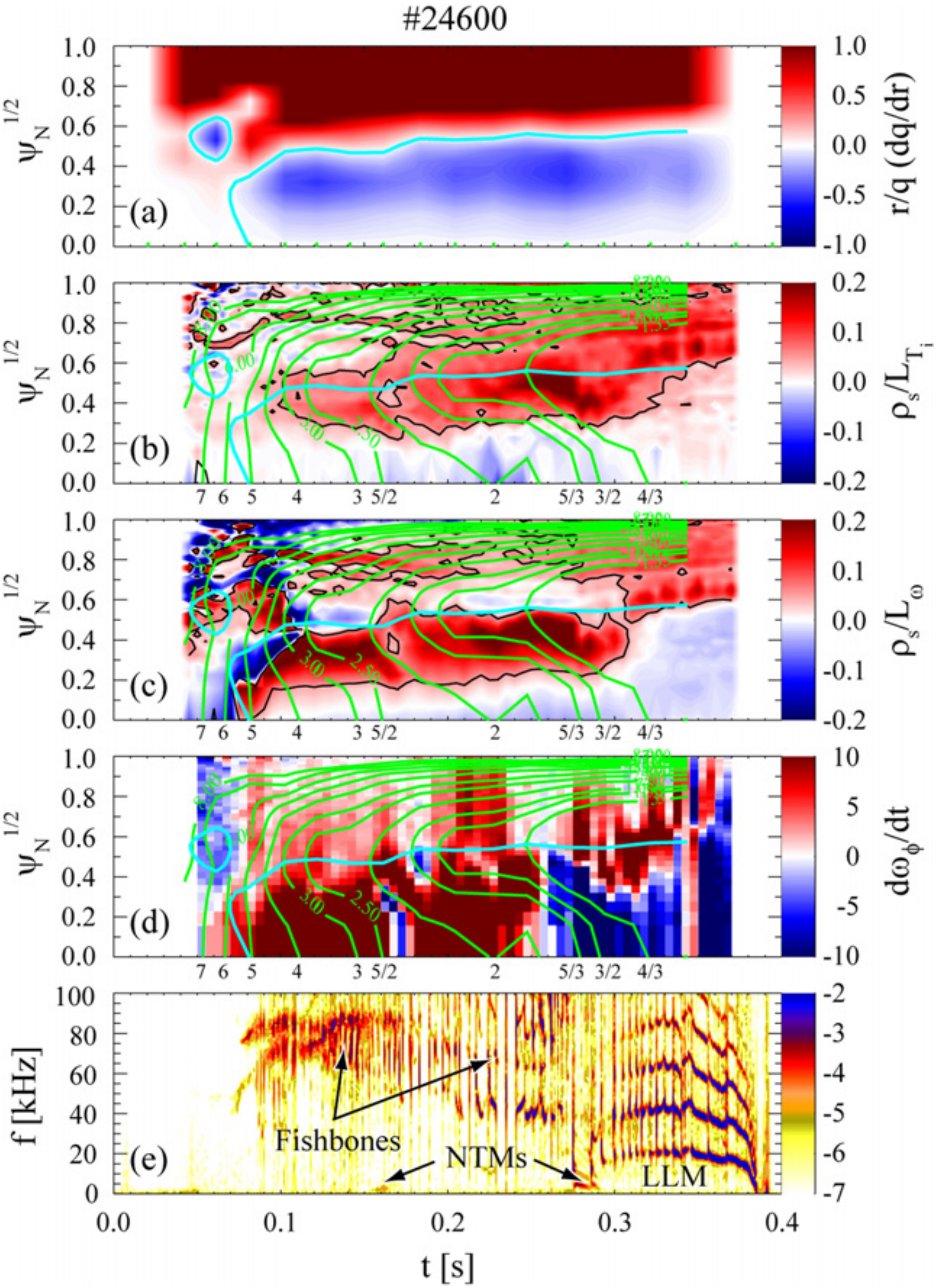

Figure 28: Evolution of (a) magnetic shear, (b) normalized ITG $\rho_s/L_{Ti}$ and (c) toroidal rotation $\rho_s/L_\omega$ gradient, (d) rate of change in toroidal rotation $\omega_\phi$ and (e) MHD in co-NBI MAST ITB discharge. Locations of rational surfaces (green, labeled below plots) and $q_{min}$ (cyan) are also shown. Taken from Field et al.[140]

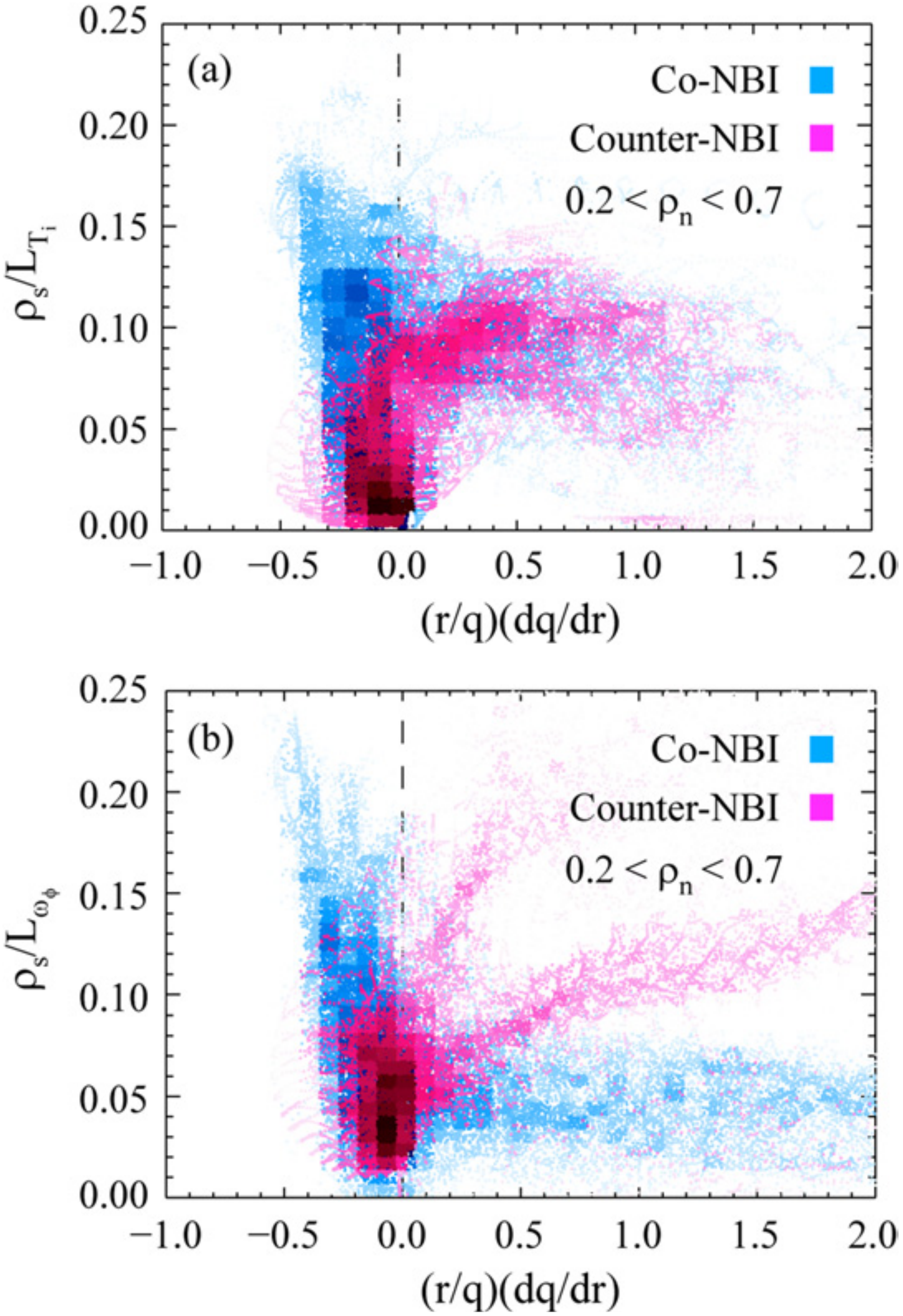

Figure 29: Dependence of normalized gradients of ion temperature $\rho_s/L_{Ti}$ (a) and rotation rate $\rho_s/L_{\omega,\phi}$ (b) on magnetic shear $\hat{s}$ for several MAST ITB discharges with co- or counter-NBI heating. Taken from Field et al.[140]

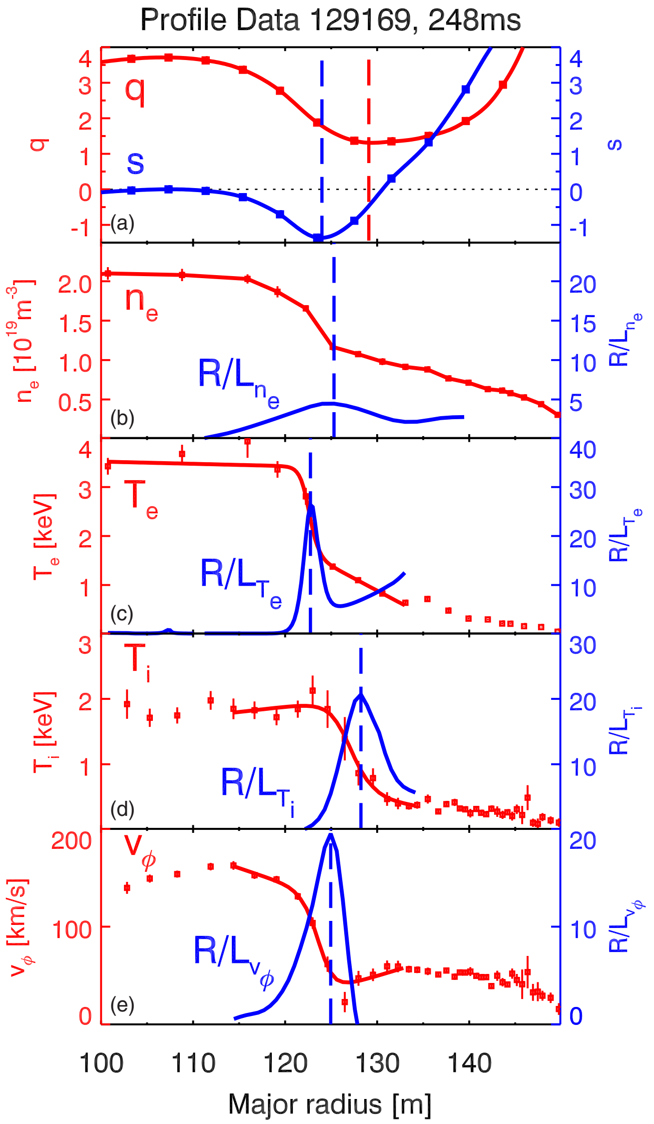

Figure 30: Kinetic profiles of an NSTX ITB. Using the left-hand axes are (a) $q$ (b) electron density $n_e$ (c) electron temperature $T_e$ (d) ion temperature $T_i$ and (e) toroidal velocity $v_\phi$. Using the right hand axes are (a) magnetic shear, $\hat{s}$ and (b)-(e) the normalized inverse gradient scale lengths. Vertical dashed lines indicate radial positions of interest for $q_{min}$, maximum negative $\hat{s}$, and peak normalized inverse gradient scale lengths. Taken from Yuh et al.[142]

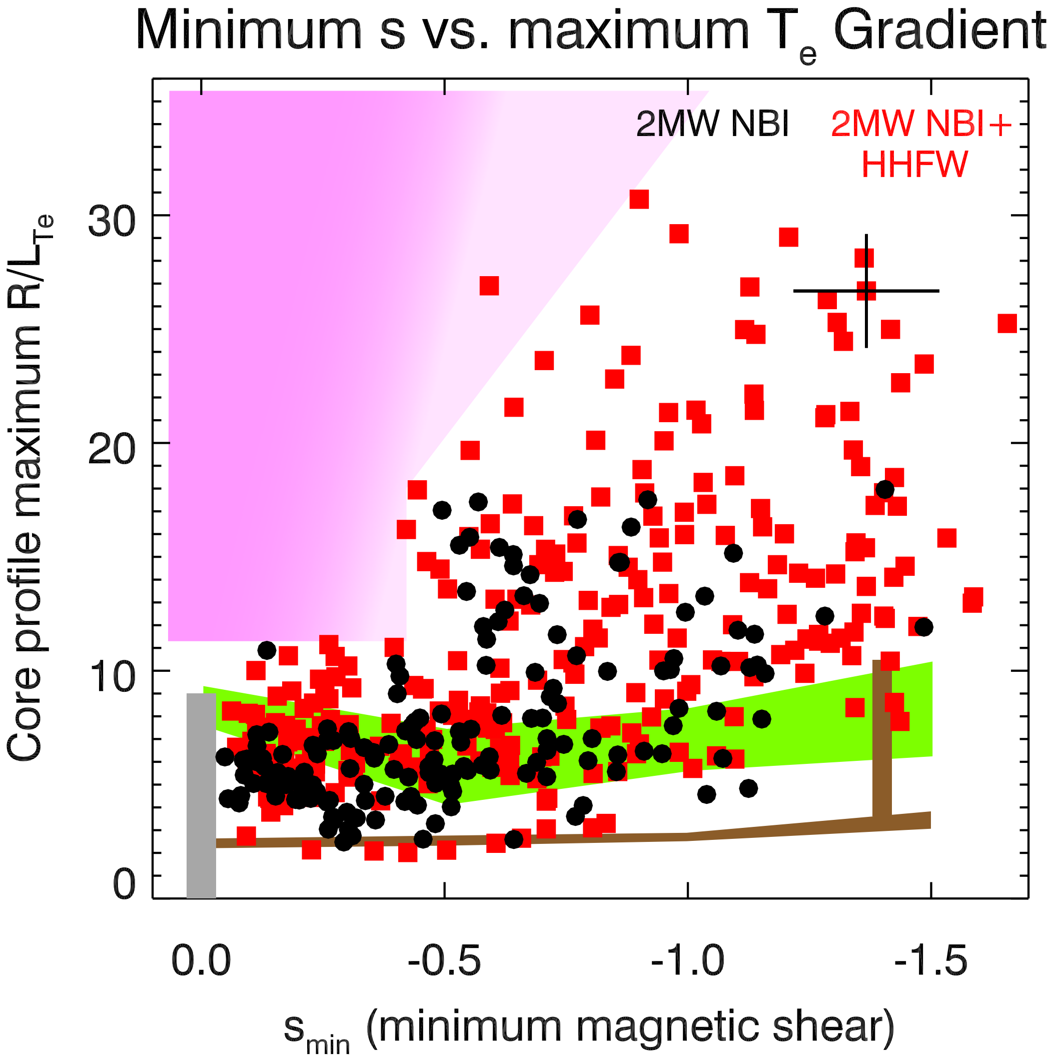

Figure 31: Value of minimum magnetic shear vs peak electron temperature gradient. Shaded region in the upper left shows an inaccessible region due to stiff profiles. Horizontal bands show critical ETG gradients calculated using linear GS2 and GYRO simulations. The gray vertical band at $s_{min}$=0 serves as a reference from high-$\beta$ H-mode discharges. Reprinted Figs. 2, 4 with permission from: Yuh et al., Phys. Rev. Lett., 106, 055003, 2011. Copyright 2011 by the American Physical Society.

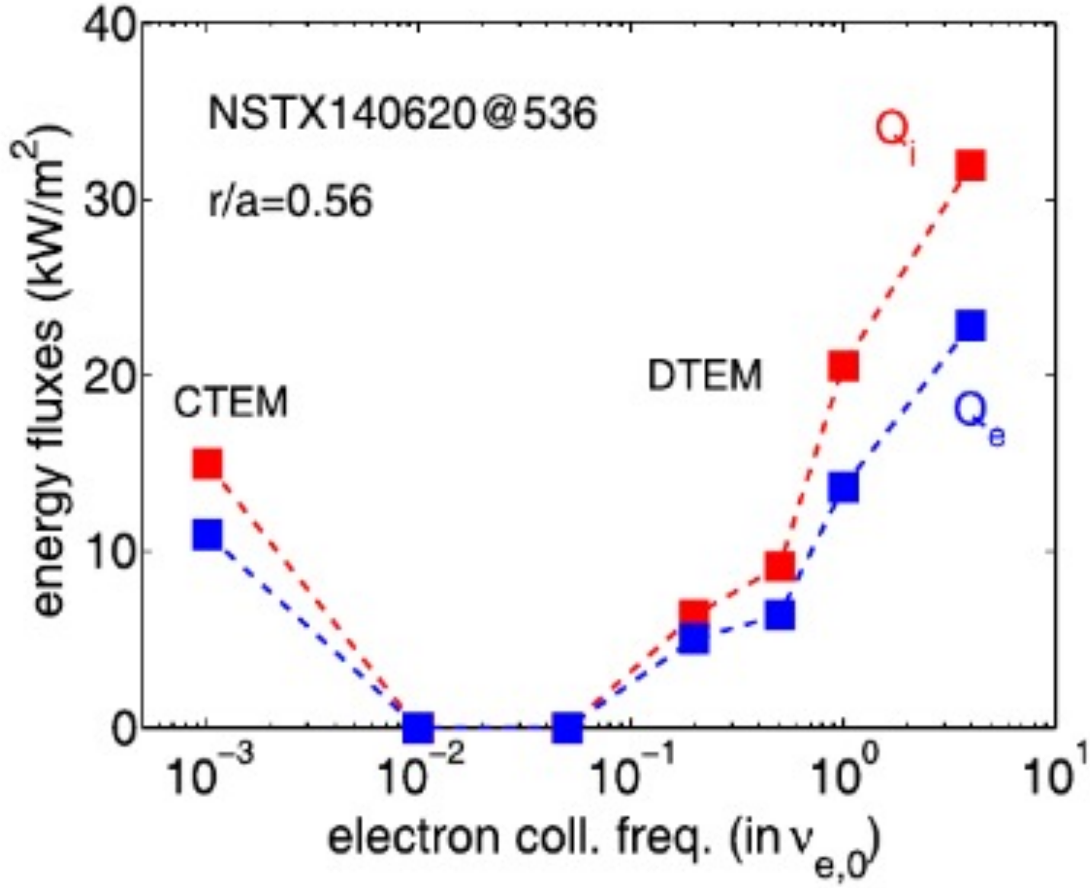

Figure 32: Simulated TEM-driven ion and electron heat fluxes for an NSTX equilibrium as functions of normalized electron collision frequency. The CTEM data points correspond to the use of zero electron collision frequency. Taken from Wang, et al.[169]

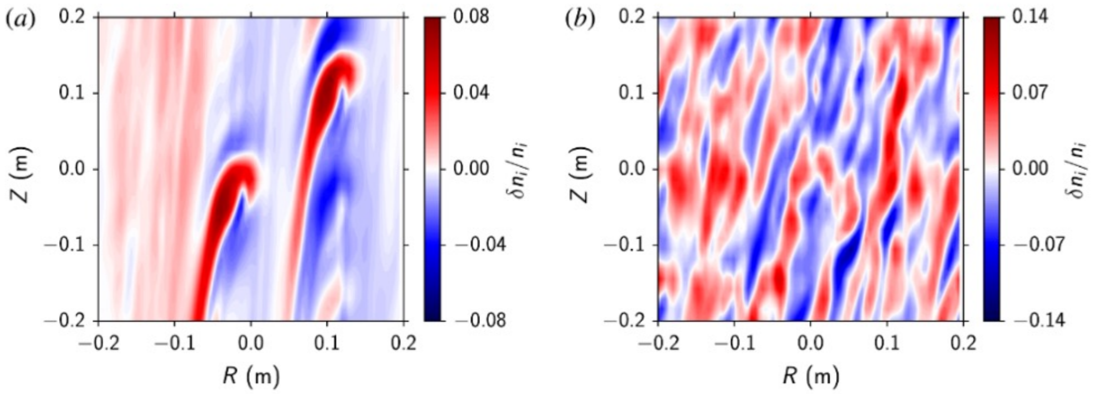

Figure 33: Normalized $\delta n_e$ fluctuations in the poloidal plane (i) close to (left), and (ii) well above the ITG threshold. Taken from van Wyk, et al..[183] Reproduced with permission of The Licensor through PLSclear.

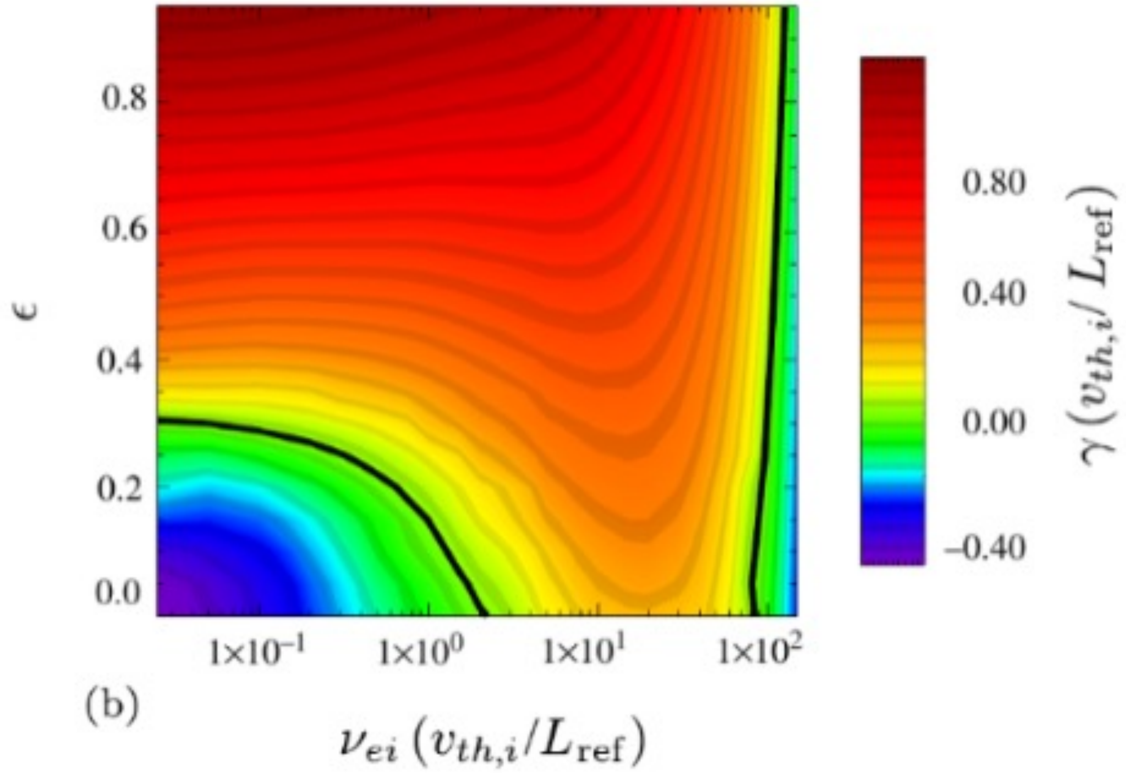

Figure 34: Growth rate of edge MTM versus $\nu_{ei}$ and inverse aspect ratio $\epsilon$, for a circular $s-\alpha$ fit to the local equilibrium at the MAST pedestal top ($\epsilon^{1/2}$ sets the trapped particle fraction). The black line indicates marginal stability. Reprinted Figure 5 with permission from: Dickinson et al., Phys. Rev. Lett., 108, 135002, 2012. Copyright 2012 by the American Physical Society.

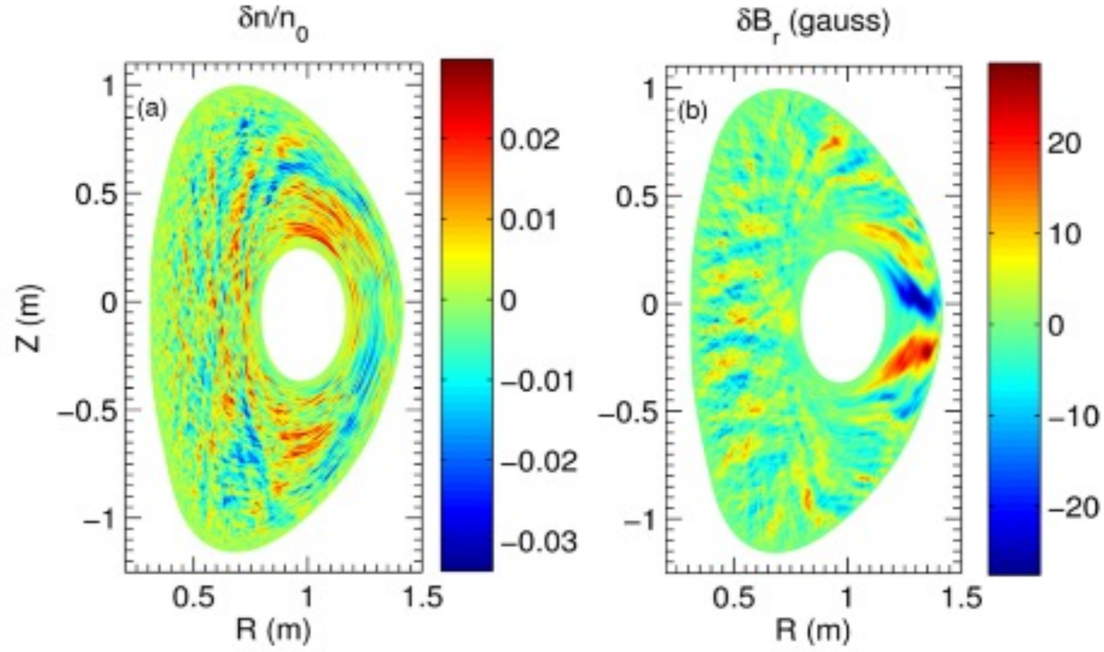

Figure 35: Contour plot of (a) $\delta n_e$ and (b) $\delta B_r$ in the poloidal plane from the saturated state of local nonlinear MTM simulations for NSTX (right plots). Taken from Guttenfelder et al.[191]

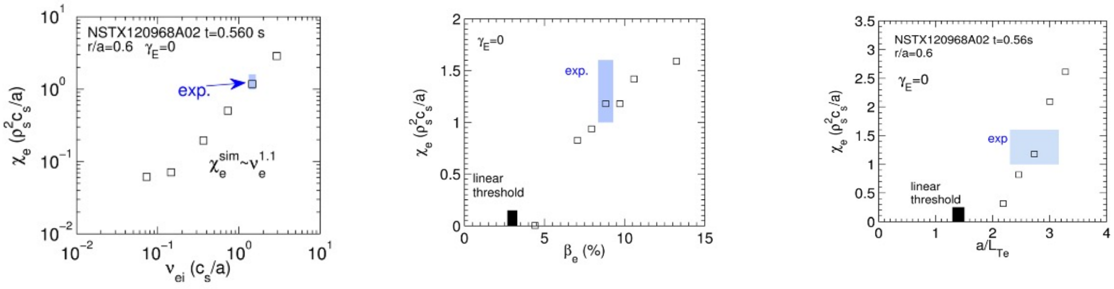

Figure 36: $\chi_{e,exp}$ and $\chi_e$ from nonlinear GYRO simulations of MTM turbulence in NSTX, showing dependences on: (a) $\nu_{ei}$, (b) $\beta_e$, and (c) $a/L_{Te}$. $\chi_e \propto \nu_{ei}^{1.1}$, and linearly increases with $\beta_e$ in this region of parameter space, but over a more extended region the dependence is non-monotonic and $\chi_e$ rolls over to decrease at higher $\nu_{ei}$ or $\beta_e$. Taken from Guttenfelder et al.[191]

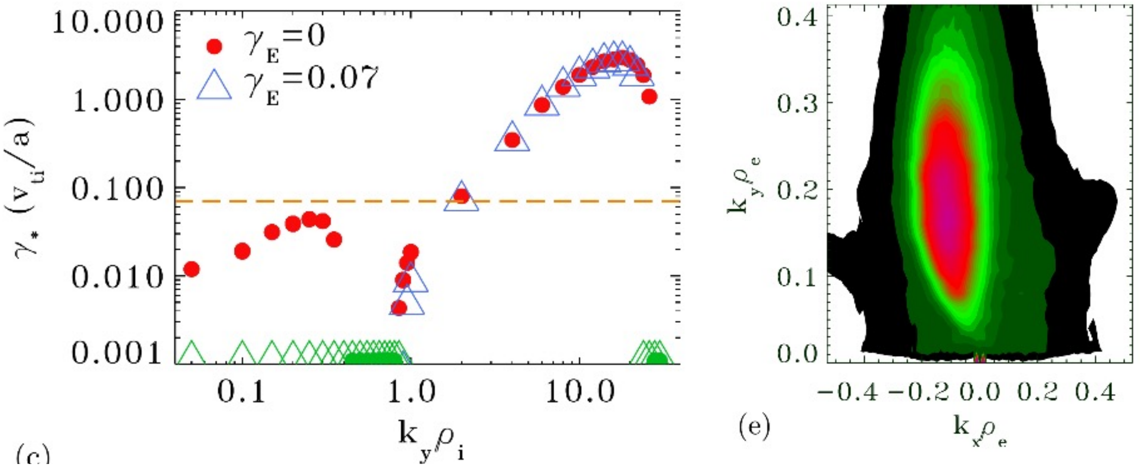

Figure 37: (a) Effective growth rates $\gamma_E$ as functions of $k_y\rho_i$ with (triangles) and without (circles) $\gamma_{E,exp}$ (indicated by horizontal dashed line) at mid-radius in a MAST H-mode, demonstrating the suppression of ion scale modes. Symbols at the $\gamma_*$-axis minimum denote stable modes. (b) Fieldline averaged saturated spectrum of $\delta\Phi^2(k_x,\ k_y)$ for an ETG simulation with $\gamma_E = 4\gamma_{E,exp}$, demonstrating anisotropy and $\gamma_E$ induced eddy tilting. Taken from Roach et al.[173]

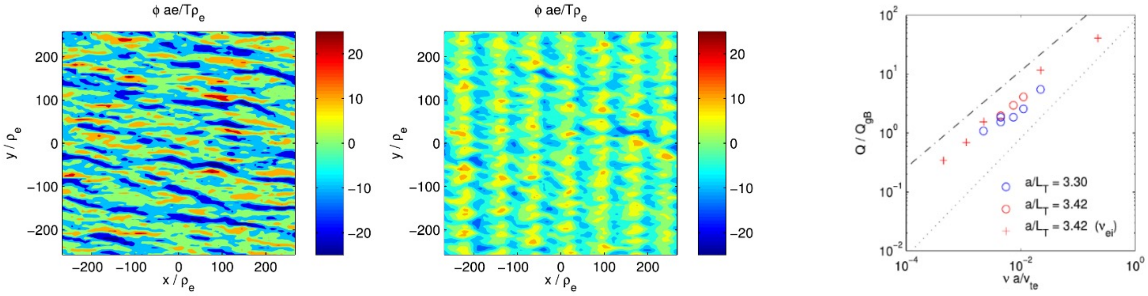

Figure 38: Normalized electrostatic potential at outboard midplane from GS2 simulation of ETG turbulence in MAST-like parameters at $\nu = 0.2\nu_{exp}$ (a) pseudo-saturated state dominated by streamers at $t = 1200a/v_{th,e}$ and (b) long-time saturated state at $t = 7835a/v_{th,e}$ with lower transport because zonal flows have broken up the streamers.(c) normalized electron heat flux from ETG turbulence has linear dependence on collisionality for several values of $R/L_{Te}$. Taken from Colyer et al.[220]

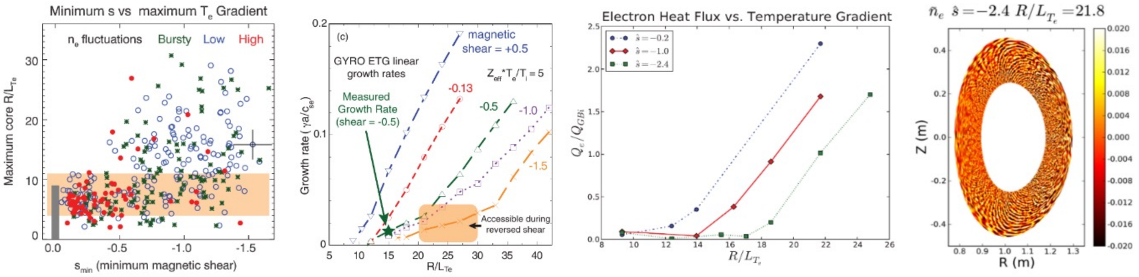

Figure 39: Plots from study of e-ITB plasmas in NSTX. (a) Maximum core $R/L_{Te}$ versus minimim magnetic shear, showing improved access to extremely high $R/L_{Te}$ and suppression of high-$k$ fluctuations at increasingly negative $\hat{s}$. (b) Linear GYRO results showing ETG growth rates reducing with increasingly negative $\hat{s}$, but without any significant change to $R/L_{Te,crit,ETG}$. (Taken from Yuh et al.[143]) (c) ETG electron heat flux versus$R/L_{Te}$ for different values of $\hat{s}$ inside an NSTX e-ITB. The nonlinear threshold gradient is increasingly upshifted beyond the linear threshold as $\hat{s}$ gets more negative. (d) Density fluctuations in poloidal cross section from a local GYRO calculation of ETG turbulence at $R/L_{Te}$ above the nonlinear threshold, showing high amplitude fluctuations giving significant electron heat transport at the top and bottom of the flux surface. (Taken from Peterson et al.[230])

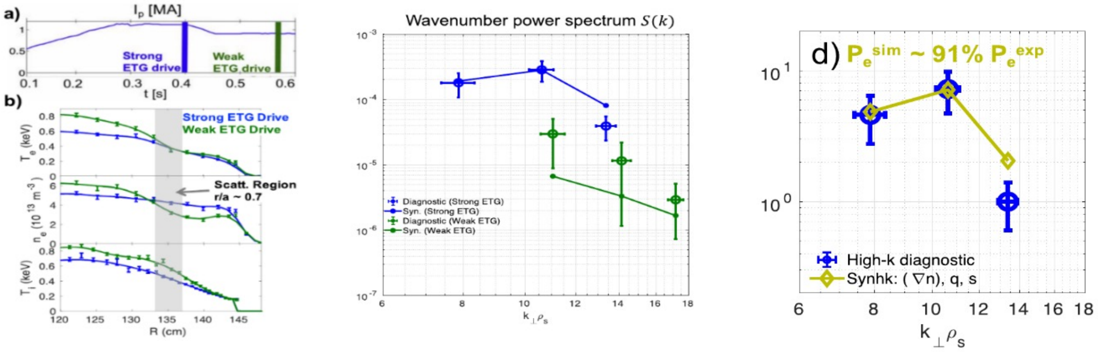

Figure 40: (a) $I_p$ time trace from NBI heated NSTX H-mode at modest $\beta$, indicating two times when ETG drive is strong and weak. (b) Radial profiles of $T_e,\ n_e$ and $T_i$ at these times. (c) Comparisons of fluctuation spectra from the high-$k$ scattering diagnostic at $r/a = 0.7$ in (open circles with error bars), with synthetic diagnostic spectra from nonlinear GYRO simulations of ETG turbulence (solid points connected by line). Blue and green correspond to times with high and low ETG drive, respectively. (d) Experimental and synthetic wavenumber spectral shape match well for the strong ETG condition where the ETG GYRO simulation used $R/L_n$ optimized to within $R/L_{n,exp} \pm 1\sigma,\ q = 0.9q_{exp}$, and $\hat{s} = 1.2\hat{s_{exp}}$. In (c), (d) the diagnostic spectra were scaled by a constant which was chosen to minimize "distance" from the synthetic spectrum for the strongly driven case. Taken from Ruiz Ruiz et al.[233]

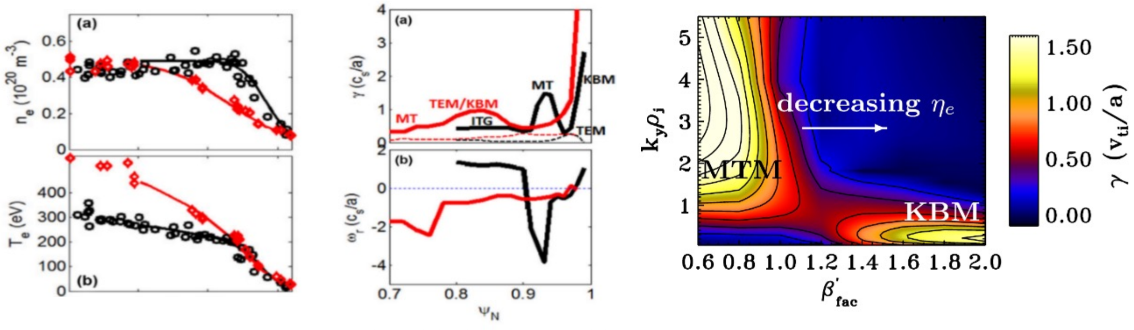

Figure 41: (a) $n_e$ (top) and $T_e$ (bottom) profiles from NSTX discharges with (red) and without (black) 5355 $mg$ Li coating applied to PFCs prior to the discharge. (Taken from Canik et al.[200]) (b) Growth rates and frequencies of the dominant microinstability at $k_\theta \rho_s \leq 1$ as a function of normalized poloidal flux for NSTX equilibria shown (left) with (red) and without (black) Li conditioning shown in (a). (c) Contour plot showing growth rate of dominant modes as a function of $k_y \rho_i$ from a scan around the local MAST equilibrium from a surface that joins by the expanding pedestal during ELM recovery. In the scan $dn_e/dr$ and $R/L_n$ are multiplied by $\beta'_{fac}$, which closely represents the measured pedestal profile evolution, and dominant MTMs are supplanted by KBMs on joining the pedestal. Taken from Dickinson et al.[198]

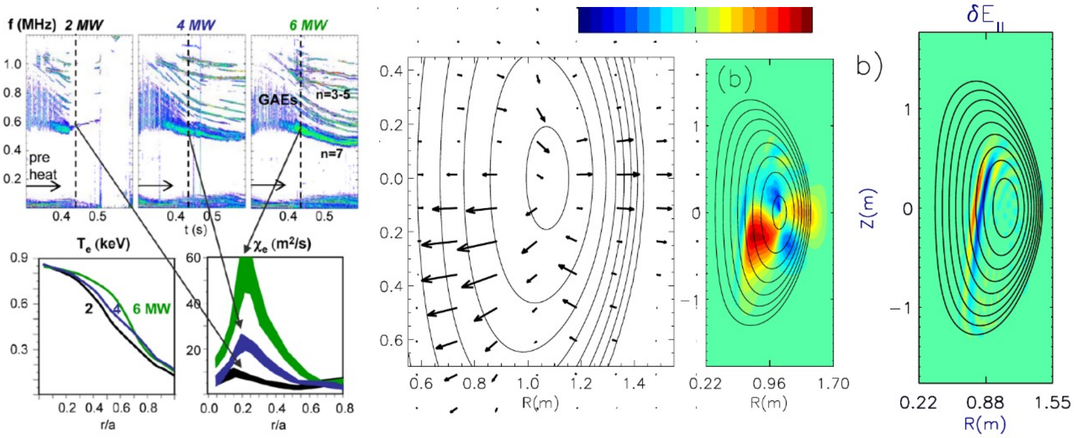

Figure 42: (a) Correlation between GAE activity (top), $T_e$ flattening (bottom left), and increasing core $\chi_e$ (bottom right) with increasing beam power (Reprinted Fig. 3 with permission from: Stutman et al., Phys. Rev. Lett., 102, 115002, 2009. Copyright 2009 by the American Physical Society.). Alternatively results from nonlinear hybrid MHD-particle simulations illustrated in (b), (c) suggest redistribution of the fast ion heating profile off-axis by "energy channelling" due to interactions between GAE and KAW. (b) Simulations for $n = 4$ modes show an outward flux of fast ion energy arising from the coupling of core driven GAEs to KAWs driven at an off-axis resonance. (c) Contour plot of $\delta E_\parallel$ (from the same simulation) shows the off-axis resonance location where plasma electrons are heated by the KAW. ((b),(c), taken from Belova et al.[239]

# References

[1]PENG, Y.-K.M. and D.J. Strickler, Nucl. Fusion **26**, 769 (1986).

[2]PENG, Y.-K.M., Phys. Plasmas **7**, 1681 (2000).

[3]VOSS, G.M., et al., Fusion Engineering. and Design **83**, 1648 (2008).

[4]ABDOU, M.A, et al., Fusion Technology **29**, 1 (1996).

[5]PENG, Y.-K.M., et al., Plasma Phys. Controlled Fusion **47**, B263 (2003).

[6]PENG, Y.-K.M., et al., Fusion Science and Technology **56**, 957 (2009).

[7]WILSON, H.R., et al., Nucl. Fusion **44**, 917 (2004).

[8]MENARD, J.E., et al., Nucl. Fusion **51**, 103014 (2011).

[9]MENARD, J.E., et al., Nucl. Fusion **56**, 106023 (2016).

[10]MENARD, J.E., et al., Phil. Trans. R. Soc. A **377**, 20170440 (2019).

[11]COSTLEY, A.E., et al., Phil. Trans. R. Soc. A **377**, 20170439 (2019).

[12]KAYE, S.M., et al., Fusion Technology **36**, 16 (1999).

[13]ONO, M., et al., Nucl. Fusion **41**, 1435 (2001).

[14]DARKE, A.C., et al., Fusion Technology **1**, 799 (1995).

[15]SYKES, A., et al., Plasma Phys. Controlled Fusion **36**, 1393 (1994).

[16]MENARD, J.E., et al., Nucl. Fusion **37**, 595 (1997).

[17]ROBERTO, M., et al., Nucl. Fusion **32**, 1666 (1992).

[18]BICKERTON, R.J., J.W. Connor and J.B. Taylor, Nature Phys. Sci. **229**, 110 (1971).

[19]GALEEV, A.A., Sov. Phys. JETP **32**, 752 (1971).

[20]GERHARDT, S.P., D.A. Gates, S.M. Kaye, et al., Nucl. Fusion **51**, 073031 (2011).

[21]SABBAGH, S.A., et al., Nucl. Fusion **53**, 104007 (2013).

[22]ITER PHYSICS BASIS, Nucl. Fusion **39**, 2137 (1999).

[23]SYKES, A., M.F. Turner and S. Patel, $\beta$-limits in tokamaks due to high-n ballooning modes, in *Proc. 11th Eur. Conf. Controlled Fusion and Plasma Physics (Aachen) vol 2, p. 363 (Petit-Lancy, Switzerland: European Physical Society)*, 1983.

[24]TROYON, F., R. Gruber, H. Saurenmann, et al., Plasma Phys. Controlled Fusion **26**, 209 (1984).

[25]REWOLDT, G., et al., Phys. Plasmas **3**, 1667 (1996).

[26]KOTSCHENREUTHER, M., et al., Nucl. Fusion **40**, 677 (2000).

[27]GORELENKOV, N.N., et al., Phys. Plasmas **11**, 2586 (2004).

[28]TAKASE, H., et al., J. Phys. Soc. Japan **70**, 609 (2001).

[29]KOTSCHENREUTHER, M., et al., Phys. Plasmas **14**, 072502 (2007).

[30]RYUTOV, D., et al., Phys. Plasmas **14**, 064502 (2007).

[31]JARBOE, T.R., et al., Fusion Technology **15**, 7 (1989).

[32]JARBOE, T.R., et al., Phys. Plasmas **5**, 1807 (1998).

[33]HANADA, K., et al., IAEA FusionEnergy Conference Proceedings, FT/P3-25, 2008.

[34]ONO, Y., et al., Nucl. Fusion **43**, 789 (2003).

[35]ONO, Y., et al., IAEA FusionEnergy Conference Proceedings, EX/P9-4, 2008.

[36]NAGATA, M., et al., Phys. Plasmas **10**, 2932 (2003).

[37]CHUNG, K.J., et al., Plasma Science and Technology **15**, 244 (2013).

[38]WANG, W.H., et al., Plasma Phys. Controlled Fusion **47**, 1 (2005).

[39]TAKASE, H., et al., Nucl. Fusion **41**, 1543 (2001).

[40]MAEKAWA, T., et al., Nucl. Fusion **45**, 1439 (2005).

[41]MAJESKI, R.J., et al., Phys. Rev. Lett. **97**, 075002 (2006).

[42]MAJESKI, R.J., et al., Nucl. Fusion **49**, 055014 (2009).

[43]ONO, M. and R. Kaita, Phys. Plasmas **22**, 040501 (2015).

[44]GRYZANEVICH, M., et al., Phys. Rev. Lett. **80**, 3972 (1998).

[45]GARTSKA, G.D., et al., Phys. Plasmas **10**, 1805 (2003).

[46]GUSEV, V.K., et al., Nucl. Fusion **49**, 104021 (2009).

[47]MINAEV, V.B., et al., IOP Conf. Series: Journal of Physics **1094**, 012001 (2018).

[48]CAROLAN, P.G., et al., Plasma Phys. Controlled Fusion **40**, 615 (1998).

[49]SYKES, A., et al., Phys. Rev. Lett. **84**, 495 (2000).

[50]SNIPES, J.A., et al., Proc. of the 24th EPS Conf., Berchtesgaden, Part III, P. 96, 1997.

[51]MAINGI, R., M.G. Bell, R.E. Bell, et al., Phys. Rev. Lett. **88**, 035003 (2002).

[52]MAINGI, R., M.G. Bell, R.E. Bell, et al., Nucl. Fusion **43**, 969 (2003).

[53]KAYE, S.M., C.E. Bush, E. Fredrickson, et al., Phys. Plasmas **10**, 3953 (2003).

[54]SYKES, A., et al., Nucl. Fusion **41**, 1423 (2001).

[55]COUNSELL, G.F., et al., Plasma Phys. Controlled Fusion **44**, B23 (2002).

[56]FIELD, A.R., P.G. Carolan, R.J. Akers, et al., Plasma Phys. Controlled Fusion **44**, A113 (2002).

[57]THOME, K., M.W. Bongard, J.L. Barr, et al., Phys. Rev. Lett. **116**, 175001 (2016).

[58]THOME, K., M.W. Bongard, J.L. Barr, et al., Nucl. Fusion **57**, 022018 (2017).

[59]MENARD, J.E., et al., Nucl. Fusion **57**, 102006 (2017).

[60]MAINGI, R., C.S. Chang, S.H. Ku, et al., Plasma Phys. Controlled Fusion **46**, A305 (2004).

[61]AKERS, R.J., et al., Phys. Plasmas **9**, 3919 (2002).

[62]LLOYD, B., et al., Nucl. Fusion **47**, S658 (2007).

[63]LLOYD, B., et al., Nucl. Fusion **43**, 1665 (2003).

[64]MAINGI, R., et al., Nucl. Fusion **50**, 064010 (2010).

[65]FUNDAMENSKI, W., F. Mitello, D. Moulton, et al., Nucl. Fusion **52**, 062003 (2012).

[66]MEYER, H., et al., Nucl. Fusion **53**, 104008 (2013).

[67]KAYE, S.M., R. Maingi, D. Battaglia, et al., Nucl. Fusion **51**, 113019 (2011).

[68]BUSH, C.E., M.G. Bell, R.E. Bell, et al., Phys. Plasmas **10**, 1755 (2003).

[69]TAKIZUKA, T., et al., Plasma Phys. Controlled Fusion **46**, A227 (2004).

[70]CHANG, C.S., et al., Phys. Plasmas **11**, 2649 (2004).

[71]BATTAGLIA, D.J., C.S. Chang, S.M. Kaye, et al., Nucl. Fusion **53**, 113032 (2013).

[72]COUNSELL, G.F., et al., Nucl. Fusion **45**, S157 (2005).

[73]ROGERS, B.N., J.F. Drake, Z. Zeiler, et al., Phys. Rev. Lett. **81**, 4396 (1998).

[74]GUZDAR, P.N., R.G. Kleva, A. Das, et al., Phys. Rev. Lett. **87**, 015001 (2001).

[75]WILSON, H.R., J.W. Connor, A.R. Field, et al., Phys. Plasmas **6**, 1925 (1999).

[76]POGUTSE, O., Y. Igitkhanov, W. Kerner, et al., Cont. Fusion Plasma Physics **21A**, 1545 (1997).

[77]GUZDAR, P.N., R.G. Kleva, R. Groebner, et al., Phys. Rev. Lett. **89**, 265004 (2002).

[78]ZWEBEN, S., et al., Phys. Plasmas **17**, 102502 (2010).

[79]WHITE, R.B., et al., Phys. Plasmas **13**, 072301 (2006).

[80]MARTIN, Y.R., T. Takizuka, et al., J. Phys. Conf. Series **123**, 012033 (2008).

[81]RYTER, F., et al., Plasma Phys. Controlled Fusion **44**, A415 (2002).

[82]DRAPER, N.R. and H. Smith, Applied Regression Analysis, 2nd Edition, John Wiley and Sons, NY, 1981.

[83]ANDERSON, T.W., Ann. Stat. **12**, 1 (1984).

[84]GELMAN, A., Bayesian Data Analysis, 2nd Edition, Chapman and Hall, Boca Raton, FL, 2009.

[85]ALLEN, L., and C. Bishop, Plasma Phys. Controlled Fusion **34**, 1291 (1992).

[86]MURARI, A., et al., Nucl. Fusion **57**, 126017 (2017).

[87]SPEARS, B.K., et al., Phys. Plasmas **25**, 080901 (2018).

[88]KAYE, S.M., et al., Phys. Plasmas **8**, 1977 (2001).

[89]KURSKIEV, G.S., et al., Plasma Phys. Controlled Fusion **59**, 045010 (2017).

[90]SYKES, A., et al., Nucl. Fusion **39**, 1271 (1999).

[91]KAYE, S.M., M.G. Bell, R.E. Bell, et al., Nucl. Fusion **46**, 848 (2006).

[92]SYKES, A., et al., Plasma Phys. Controlled Fusion **39**, B247 (1997).

[93]KAYE, S.M., F.M. Levinton, D. Stutman, et al., Nucl. Fusion **47**, 499 (2007).

[94]VALOVIC, M., et al., Nucl. Fusion **45**, 942 (2005).

[95]VALOVIC, M., R. Akers, G. Cunningham, et al., Nucl. Fusion **49**, 075016 (2009).

[96]TELNOVA, A. Yu., et al., J. Phys. Conf. Ser. **907**, 012014 (2017).

[97]KURSKIEV, G.S., et al., Nucl. Fusion **59**, 066032 (2019).

[98]BAKHAROV, N.N., et al., Nucl. Fusion **58**, 126029 (2018).

[99]KURSKIEV, G.S., et al., Accepted for publication in Nuclear Fusion, 2021.

[100]MAINGI, R., et al., Nucl. Fusion **52**, 083001 (2012).

[101]KAYE, S.M., R. Maingi, D. Battaglia, et al., Nucl. Fusion **53**, 063005 (2013).

[102]BUXTON, P., et al., Plasma Phys. Controlled Fusion **61**, 035006 (2019).

[103]KURSKIEV, G.S., N.N. Bakharev, F.V. Chernyshev, et al., Energy confinement in the spherical tokamak globus-m2 with a toroidal magnetic field approaching 0.8 t, Submitted to Nuclear Fusion for publication, 2021.

[104]KAYE, S.M., et al., Plasma Phys. Controlled Fusion **48**, A429 (2006).

[105]STUTMAN, D., et al., Phys. Rev. Lett. **102**, 115002 (2009).

[106]CONNOR, J.W., Nucl. Fusion **17**, 1047 (1977).

[107]CONNOR, J.W., Plasma Phys. Controlled Fusion **30**, 619 (1988).

[108]KADOMTSEV, B.B., Sov. Phys. - J. Plasmas Phys. **1**, 295 (1975).

[109]PETTY, C.C., Phys. Plasmas **15**, 080501 (2008).

[110]LUCE, T., Plasma Phys. Controlled Fusion **50**, 043001 (2008).

[111]VALOVIC, M., R. Akers, M. deBock, et al., Nucl. Fusion **51**, 073045 (2011).

[112]KAYE, S.M., R.E.. Bell, D. Gates, et al., Phys. Rev. Lett. **98**, 175002 (2007).

[113]BELL, R.E., et al., Rev. Sci. Inst. **77**, 10E902 (2006).

[114]BOURDELLE, C., et al., Phys. Plasmas **10**, 2881 (2003).

[115]SMITH, D.R., et al., Phys. Rev. Lett. **102**, 225005 (2009).

[116]MENARD, J.E., et al., Nucl. Fusion **43**, 330 (2003).

[117]CHAPMAN, I.T., et al., Plasma Phys. Controlled Fusion **49**, B385 (2007).

[118]BERKERY, J.W., et al., Phys. Plasmas **24**, 056103 (2017).

[119]SOLOMON, W., et al., Phys. Rev. Lett. **101**, 065004 (2008).

[120]KAYE, S.M., et al., Nucl. Fusion **49**, 045010 (2009).

[121]MEYER, H., et al., Nucl. Fusion **49**, 104017 (2009).

[122]PEETERS, A.G., et al., Phys. Rev. Lett. **98**, 265003 (2007).

[123]HAHM, T.S., et al., Phys. Plasmas **14**, 072302 (2007).

[124]GUTTENFELDER, W., S.M. Kaye, Y. Ren, et al., Phys. Plasmas **23**, 052508 (2016).

[125]GUTTENFELDER, W., et al., Nucl. Fusion **57**, 056022 (2017).

[126]PARK, J.-K., et al., Nucl. Fusion **53**, 063012 (2013).

[127]HILLESHEIM, W.H., et al., Nucl. Fusion **55**, 032003 (2015).

[128]BARNES, M., et al., Phys. Rev. Lett. **111**, 055005 (2013).

[129]PARRA, F. and M. Barnes, Plasma Phys. Controlled Fusion **57**, 045002 (2015).

[130]HENDERSON, S.S., et al., Nucl. Fusion **54**, 093013 (2014).

[131]HENDERSON, S.S., et al., Plasma Phys. Controlled Fusion **57**, 095001 (2015).

[132]STUTMAN, D., et al., Phys. Plasmas **10**, 4387 (2003).

[133]HENDERSON, S.S., et al., Nucl. Fusion **44**, 513 (2004).

[134]SCOTTI, F., et al., Nucl. Fusion **53**, 083001 (2013).

[135]SCOTTI, F., et al., J. Nucl. Materials **463**, 1165 (2015).

[136]SCOTTI, F., et al., Nuclear Materials and Energy **12**, 768 (2017).

[137]SCOTTI, F., PhD Thesis, Princeton University, 2014.

[138]AKERS, R.J., et al., Plasma Phys. Controlled Fusion **45**, A175 (2003).

[139]MEYER, H., et al., Plasma Phys. Controlled Fusion **46**, A291 (2004).

[140]FIELD, A.R., et al., Nucl. Fusion **51**, 063006 (2011).

[141]LLOYD, B., et al., Nucl. Fusion **51**, 094013 (2011).

[142]YUH, H., et al., Phys. Plasmas **16**, 056120 (2009).

[143]YUH, H., et al., Phys. Rev. Lett. **106**, 055003 (2011).

[144]KOTSCHENREUTHER, M., G. Rewoldt and W.M. Tang, Computer Physics Communications **88**, 128 (1995).

[145]CANDY, J. and R. E. Waltz, Journal of Computational Physics **186**, 545 (2003).

[146]PEETERS, A.G. and D. Strintzi, Phys. Plasmas **11**, 3748 (2004).

[147]WANG, W.X., Z. Lin, W. M. Tang, et al., Phys. Plasmas **13**, 092505 (2006).

[148]JOLLIET, S., A. Bottino, P.Angelino, et al., Computer Physics Communications **177**, 409 (2007).

[149]BOTTINO, A., A.G. Peeters, R. Hatzky, et al. , Phys. Plasmas **14**, 010701 (2007).

[150]ROACH, C.M., J.W. Connor and S. Janjua, Plasma Phys. Controlled Fusion **37**, 679 (1995).

[151]G. M. STAEBLER, G. Colyer, S. Kaye, J. E. Kinsey, and R. E. Waltz, Testing the Trapped Gyro-Landau Fluid Transport Model with Data from Tokamaks and Spherical Tori, in *Proceedings of 22nd IAEA Fusion Energy Conference, Geneva, TH/P8-42*, 2008.

[152]ROACH, C.M., D.J. Applegate, J.W. Connor, et al., Plasma Phys. Controlled Fusion **47**, B323 (2005).

[153]REDI, M.H., W. Dorland, C.L. Fiore, et al., Testing Gyrokinetics on C-Mod and NSTX, in *Proceedings of 32nd EPS Conference on Plasma Physics, Tarragona, Spain*, volume ECA 29C, P-5.041, 2005.

[154]REDI, M.H., W. Dorland, R. Bell, et al. , Gyrokinetic calculations of microturbulence and transportfor nstx and alcator-cmod h-modes, in *Proceedings of 30th EPS Conference on Plasma Physics, St. Petersburg, Russia*, volume ECA 27A, P-4.94, 2003.

[155]APPLEGATE, D.J., C M Roach, S C Cowley, et al., Phys. Plasmas **11**, 5085 (2004).

[156]BELOVA, E.V., N.N. Gorelenkov, E.D. Fredrickson, et al., Phys. Rev. Lett. **115**, 015001 (2015).

[157]ROACH, C.M., R.J. Akers, N.J. Conway, et al., Nucl. Fusion **41**, 11 (2001).

[158]FIELD, A.R., R.J. Akers, C. Brickley, et al., Core heat transport in the mast spherical tokamak, in *Proceedings of 22nd IAEA Fusion Energy Conference, Vilamoura*, pages EX/P2–11, 2004.

[159]TELNOVA, A.Yu., G.S. Kurskiev, I.V. Miroshnikov, et al., Plasma Phys. Controlled Fusion **62**, 045011 (2020).

[160]GUTTENFELDER, W., S.M. Kaye, D.M. Kriete, et al., Nucl. Fusion **59**, 056027 (2019).

[161]REN, Y., E. Belova, N. Gorelenkov, et al., Nucl. Fusion **57**, 072002 (2017).

[162]GUTTENFELDER, W., J.L. Peterson, J. Candy, et al., Nucl. Fusion **53**, 093022 (2013).

[163]GARZOTTI, L., J. Figueiredo, C.M. Roach, et al., Plasma Phys. Controlled Fusion **56**, 035004 (2014).

[164]CONNOR, J.W., C.M. Roach, R.J. Hastie, et al., Turbulent transport in spherical tokamaks with transport barriers (poster), in *Proceedings of 21st IAEA Fusion Energy Conference, Chengdu, China, TH/P2-2*, 2006.

[165]B. COPPI and F. Pegoraro, Nucl. Fusion **17**, 969 (1977).

[166]BELLI, E.A. and J. Candy, Phys. Plasmas **17**, 112314 (2010).

[167]PEETERS, A.G., C. Angioni, M. Apostoliceanu, et al., Physics of Plasmas **12**, 022505 (2005).

[168]JENKO, F., W. Dorland and G. W. Hammett, Phys. Plasmas **8**, 4096 (2001).

[169]WANG, W.X., et al., Phys. Plasmas **22**, 102509 (2015).

[170]REN, Y., W.X. Wang, W. Guttenfelder, et al., Nucl. Fusion **60**, 026005 (2019).

[171]WANG, W.X., S. Ethier, Y. Ren, et al., Nucl. Fusion **55**, 122001 (2015).

[172]MENARD, J.E., S. Gerhardt, M. Bell, et al., Nucl. Fusion **52**, 083015 (2012).

[173]ROACH, C.M., I.G. Abel, R.J. Akers, et al, Plasma Phys. Controlled Fusion **51**, 124020 (2009).

[174]CATTO,P. J., M.N. Rosenbluth, and C.S. Liu, Phys. Fluids **16**, 1719 (1973).

[175]GHIM, Y.-C., A.R. Field, A A. Schekochihin, et al, Nucl. Fusion **54**, 042003 (2014).

[176]SCHEKOCHIHIN, A.A., E G Highcock and S.C. Cowley, Plasma Phys. Controlled Fusion **54**, 055011 (2012).

[177]HIGHCOCK, E.G., M. Barnes, A.A. Schekochihin, et al., Phys. Rev. Lett. **105**, 215003 (2010).

[178]HIGHCOCK, E.G., A.A. Schekochihin, S. Cowley, et al., Phys. Rev. Lett. **109**, 265001 (2012).

[179]SAARELMA, S., P. Hill, A. Bottino, et al., Plasma Phys. Controlled Fusion **54**, 085012 (2012).

[180]FIELD, A.R., D. Dunai, Y.-C. Ghim, et al. , Plasma Phys. Controlled Fusion **56**, 025012 (2014).

[181]FOX, M.F., F. van Wyk, A.R. Field, et al., Plasma Phys. Controlled Fusion **59**, 034002 (2017).

[182]van WYK, F., E G Highcock, A.R. Field, et al., Plasma Phys. Controlled Fusion **59**, 114003 (2017).

[183]van WYK, F., E G Highcock, A.A. Schekochihin, et al., Journal of Plasma Physics **82**, 905820609 (2016).

[184]FOX, M.F., A.R. Field, F. van Wyk, et al., Plasma Phys. Controlled Fusion **59**, 044008 (2017).

[185]FIELD, A.R., N.A. Crocker, D. Dunai, et al., Influence of flow shear on the structure of ion-scale turbulence in mast, in *Proceedings of 25th IAEA Fusion Energy Conference, St Petersburg, Russia, EX/P4-38*, 2014.

[186]GHIM, Y.-C., A A. Schekochihin, A.R. Field, et al, Phys. Rev. Lett. **110**, 145002 (2013).

[187]LIN, Z., T.S. Hahm, W.W. Lee, et al., Phys. Rev. Lett. **83**, 3645 (1999).

[188]KISELEV, E.O., N.N. Bakharev, V.V. Bulanin, et al., Journal of Physics: Conference Series **1383**, 012003 (2019).

[189]APPLEGATE, D.J., C.M. Roach, J.W. Connor, et al., Plasma Phys. Controlled Fusion **49**, 1113 (2007).

[190]GUTENFELDER, W., J. Candy, S. M. Kaye, et al., Phys. Plasmas , 022506 (2012).

[191]GUTENFELDER, W., J. Candy, S. M. Kaye, et al., Phys. Plasmas **19**, 056119 (2012).

[192]D. APPLEGATE, *Gyrokinetic Studies of a Spherical Tokamak H-mode Plasma*, PhD thesis, Imperial College London, PhD Thesis, Imperial College London, 2007.

[193]DRAKE, J.F. and Y.C. Lee, Phys Fluids **20**, 1341 (1977).

[194]N. T. GLADD, J. F. Drake, C. L. Chang, and C. S. Liu, Phys. Fluids **23**, 1182 (1980).

[195]D'IPPOLITO, D.A., Y.C. Lee, and ,J.F. Drake, Phys. Fluids **23**, 771 (1980).

[196]CATTO, P.J. and M.N. Rosenbluth, Phys. Fluids **24**, 243 (1981).

[197]HAZELTINE, R.D., D. Dobrott and T.S. Wang, Phys. Fluids **18**, 1778 (1975).

[198]DICKINSON, D., C.M. Roach, S. Saarelma, et al., Phys. Rev. Lett. **108**, 135002 (2012).

[199]DICKINSON, D., C.M. Roach, S. Saarelma, et al., Plasma Phys. Controlled Fusion **55**, 074006 (2013).

[200]CANIK, J.M., W. Guttenfelder, R. Maingi, et al., Nucl. Fusion **53**, 113016 (2013).

[201]PREDEBON, I. and F. Sattin, Phys. Plasmas **20**, 040701 (2013).

[202]SWAMY, A.K., R. Ganesh, J. Chowdhury, et al., Phys Plasmas **21**, 082513 (2014).

[203]HAMED, M., M. Muraglia, Y. Camenen, et al., Phys. Plasmas **26**, 092506 (2019).

[204]SMITH, D.R., W. Guttenfelder, B.P. LeBlanc, et al., Plasma Phys. Controlled Fusion **53**, 035013 (2011).

[205]WONG, K.L., S. Kaye, D.R. Mikkelsen, et al., Phys. Rev. Lett. **99**, 135003 (2007).

[206]DRAKE, J.F., N.T. Gladd, C.S. Liu, et al., Phys. Rev. Lett. **44**, 994 (1980).

[207]RECHESTER, A.B. and M.N. Rosenbluth, Phys. Rev. Lett. **40**, 38 (1978).

[208]GUTTENFELDER, W., J. Candy, S.M. Kaye, et al., Phys. Rev. Lett. **106**, 155004 (2011).

[209]REBUT, P.H., P.P. Lallia and M.L. Watkins, The critical temperature gradient model of plasma transport: Applications to jet and future tokamaks, in *Proceedings of 12th IAEA Fusion Energy Conference, Nice*, pages Volume 2, 191, 1988.

[210]WONG, K.L., S. Kaye, D.R. Mikkelsen,et al., Phys. Plasmas **15**, 056108 (2008).

[211]KAYE, S.M., W. Guttenfelder, R.E. Bell, et al., Phys. Plasmas **21**, 082510 (2014).

[212]RAFIQ, T., S. Kaye, W. Guttenfelder,et al., Phys. Plasmas **28**, 022504 (2021).

[213]DORLAND, W., F. Jenko, M. Kotschenreuther, et al., Phys. Rev. Lett. **85**, 5579 (2000).

[214]JENKO, F. and W. Dorland, Phys. Rev. Lett. **89**, 225001 (2002).

[215]RESHKO, M., C.M. Roach and the MAST Team, Plasma Phys. Controlled Fusion **50**, 115002 (2008).

[216]JOINER,N. and A. Hirose, Phys. Plasmas **14**, 112111 (2007).

[217]JOINER, N., A. Hirose, and W. Dorland, Phys. Plasmas **17**, 072104 (2010).

[218]BERK, H.L. and R.R. Dominguez, Journal of Plasma Physics , 31A148 (1977).

[219]REN, Y., W. Guttenfelder, S.M. Kaye, et al. , Phys. Plasmas **19**, 056125 (2012).

[220]COLYER, G.J., A.A. Schekochihin, F.I. Parra, et al., Plasma Phys. Controlled Fusion **59**, 055002 (2017).

[221]HORTON, W., G.T. Hoang, C. Bourdelle, et al., Phys. Plasmas **11**, 2600 (2004).

[222]MAZZUCATO, E., D.R. Smith, R.E. Bell, et al., Phys. Rev. Lett. **101**, 075001 (2008).

[223]MAZZUCATO, E., R.E. Bell, S. Ethier, et al., Nucl. Fusion **49**, 055001 (2009).

[224]REN, Y., S.M. Kaye, E. Mazzucato et al., Phys. Rev. Lett. **106**, 165005 (2011).

[225]RUIZ RUIZ, J., W Guttenfelder, A E White, et al., Phys. Plasmas **22**, 122501 (2015).

[226]JOINER, N., D Applegate, S.C. Cowley, et al., Plasma Phys. Controlled Fusion **48**, 685 (2006).

[227]JOINER, N.J., *Microinstabilities in Spherical Tokamaks*, PhD thesis, Imperial College London, PhD Thesis, Imperial College London, 2005.

[228]GUTTENFELDER, W. and J. Candy, Phys.Plasmas **18**, 022506 (2011).

[229]REN, Y., W.X. Wang, B. LeBlanc, et al., Phys. Plasmas **22**, 110701 (2015).

[230]PETERSON, J.L., R. Bell, J. Candy, et al., Phys. Plasmas **19**, 056120 (2012).

[231]HILLESHEIM, J.C., N.A. Crocker, W.A. Peebles, et al., Nucl. Fusion **55**, 073024 (2015).

[232]BARNES, M., F.I. Parra, and A.A. Schekochihin, Phys. Rev. Lett. **107**, 115003 (2011).

[233]RUIZ RUIZ, J., W Guttenfelder, A E White, et al., Plasma Phys. Controlled Fusion **61**, 115015 (2019).

[234]DICKINSON, D., S. Saarelma, R. Scannell, et al., Plasma Phys. Controlled Fusion **53**, 115010 (2011).

[235]COURY, M., W. Guttenfelder, D.R. Mikkelsen, et al., Phys. Plasmas **23**, 062520 (2016).

[236]ROACH, C.M., D. Dickinson, S. Saarelma, et al, Gyrokinetic instabilities near an evolving tokamak h-mode pedestal, in *Proceedings of 24th IAEA Fusion Energy Conference, San Diego, USA, TH/5-1*, 2012.

[237]GORELENKOV, N.N., D. Stutman, K. Tritz, et al., Nucl. Fusion **50**, 084012 (2010).

[238]KOLESNICHENKO, Ya I., Yu.V.Yakovenko andV.V. Lutsenko, Phys. Rev. Lett. **104**, 075001 (2010).

[239]BELOVA, E.V., Gorelenkov, N. N., Crocker N. A., et al., Phys. Plasmas **24**, 042505 (2017).

[240]CROCKER, N.A., S. Kubota,W.A. Peebles, et al., Nucl. Fusion **58**, 016051 (2017).

[241]FREDRICKSON, E.D., E.V. Belova, N.N. Gorelenkov, et al., Nucl. Fusion **58**, 082022 (2018).

[242]BELOVA, E.V., E.D. Fredrickson, J.R. Lestz, et al., Phys. of Plasmas **26**, 092507 (2019).

[243]MAEYAMA, S., T.-H.Watanabe, A. Ishizawa, Phys. Rev. Lett. **119**, 195002 (2017).